ISSN 2435-1288

# Nikon Research Report

Vol.6 2024

# Purpose of publication

This publication is being created to widely introduce the achievements of research and development activities conducted by Nikon Corporation. This is a result of R&D based on Nikon's core technologies of "opto-electronics" and "precision" technologies that have been incorporated in new products and/or often valued by external organizations such as academic societies.

# Foreword

Senior Executive Vice President
CTO, Deputy CFO

Yasuhiro Ohmura

Due to ongoing changes in the natural and social environments, our surroundings are evolving every day, presenting us with new challenges. In order to contribute to a sustainable society through business even in such circumstances, we'd like to more deeply understand the essence of what our customers want and collaborate with them to develop solutions that fuel their innovations.

We have passed the halfway mark of our Medium-Term Management Plan that was formulated to realize our Vision 2030 – transforming into "a key technology solutions company in a global society where humans and machines co-create seamlessly". We need to continue to advance technological innovations that underpin our value proposition, so that we can grow further in line with the plan and consistently meet the evolving expectations of society and our customers in the eras to come.

Executive Fellow
General Manager of Advanced Technology
Research & Development

Masaaki Doi

I'm pleased to present this year's report showcasing the Nikon Group's achievements in research and development. From Digital Manufacturing, which is a strategic business domain in the Medium-Term Management Plan, this report highlights that Nikon SLM Solutions AG – a new member of the Group – has developed an industry-leading, large-scale and high-speed metal 3D printer. Also featured from this domain is riblet technology – a type of biomimetic technology that imitates shark skin structure – applied to wind power generation to help realize a sustainable society. From the Healthcare Business, a digital microscopy technology that supports drug discovery and pathological diagnosis is featured. From the Imaging Business, which is one of our main businesses, we report on a super-telephoto prime lens with a built-in teleconverter featuring a slew of state-of-the-art technologies. You will also find exciting articles about light sources for future space optical communications and fundamental materials technology.

While this report represents just a fraction of the extensive technological developments within the Nikon Group, I hope that it provides an insightful glimpse into our R&D activities and opens up opportunities for our technology to contribute to a better society and environment.

# Nikon Research Report Vol.6
# 目次／ CONTENTS

## 技術解説/Technical Reports



## 研究開発論文/Research and Development Reports

# 技術解説

# Technical Reports

# PBF 式 Additive Manufacturing 装置 NXG 600E の開発

Sebastian Feist, Daniel Brück, Christoph Wangenheim

# Development of PBF Additive Manufacturing Machine NXG 600E

Sebastian FEIST, Daniel BRÜCK and Christoph WANGENHEIM

レーザー粉末床溶融（L-PBF）などの積層造形 (AM) 技術は，長い間プロトタイピングや研究用途での使用にのみ適しているという評判を乗り越えてきた．現在，Nikon SLM Solutions は，これまでに製造された中で最も複雑な金属部品の連続生産に注力する世界中の高度な目利きの顧客に AM ソリューションを提供している．NXG 600E マシンの開発により，Nikon SLM Solutions は，最大 600 mm × 600 mm × 1500 mm の寸法の部品を製造できる，最も生産性と信頼性の高い L-PBF プロセスの提供に努めており，多くの技術的課題に直面してきた．本稿では，これらの個々の課題を詳細に説明し，金属 AM の分野で革新的な機能を導入することで，これらの課題をどのように克服したかについて説明する．

Additive Manufacturing (AM) technologies such as Laser Powder Bed Fusion (L-PBF) have long surpassed the reputation of only being suitable for use in the context of prototyping or research applications. Today, Nikon SLM Solutions already provides AM solutions to highly discerning customers around the world, who are focused on serial production of the most complex metal components that have ever been manufactured. With the development of the NXG 600E machine, Nikon SLM Solutions faced many technical challenges while striving to provide the most productive and reliable L-PBF process, capable of producing parts with a dimension of up to 600 mm x 600 mm x 1500 mm. This paper describes these individual challenges in detail and how they were successfully overcome by introducing innovative features which are novel in the realm of metal AM.

**Key words** レーザー粉末床溶融（L-PBF），積層造形 (AM)，SLM Solutions，NXG 600E
laser powder bed fusion (L-PBF), additive manufacturing (AM), SLM Solutions, NXG 600E

## 1 Introduction

Laser Powder Bed Fusion (L-PBF) is a cutting-edge metal additive manufacturing technology revolutionizing industries like aerospace, automotive, and healthcare. Nikon SLM Solutions is a market leading manufacturer of metal L-PBF machines for serial production and prototyping applications, seeking to drive the mass adoption of this manufacturing technique forward and enabling the creation of previously impossible components. Additionally, L-PBF allows for customization and on-demand production, making it ideal for small- to medium-batch manufacturing and customized products.

Since its very inception as “SLM Solutions GmbH” in 2011, Nikon SLM Solutions has been focused on pushing metal additive manufacturing towards commercial and serial production maturity by implementing innovative technology solutions to boost productivity, stability, and part quality. In 2013, the German company launched the SLM®500, which was the first system to feature 4 lasers that could generate a single part simultaneously. The patented multi-laser approach quickly became an industry defining standard for highest productivity, shaping the forefront of metal additive manufacturing capabilities.

In 2020, the company reshaped the market by launching the NXG XII 600, a revolutionary machine which at the time tripled the industry adopted maximum number of lasers from 4 to 12 in a single step, as well as increasing each laser’s maximum output power from 700 W to 1000 W. This machine’s capabilities in a build envelope of 600 mm x 600 mm x 600 mm (XYZ) are still unmatched by the rest of the market in terms of productivity and robustness. Now, with the launch of the NXG 600E (shown as Fig. 1), the NXG system platform has been expanded to allow for

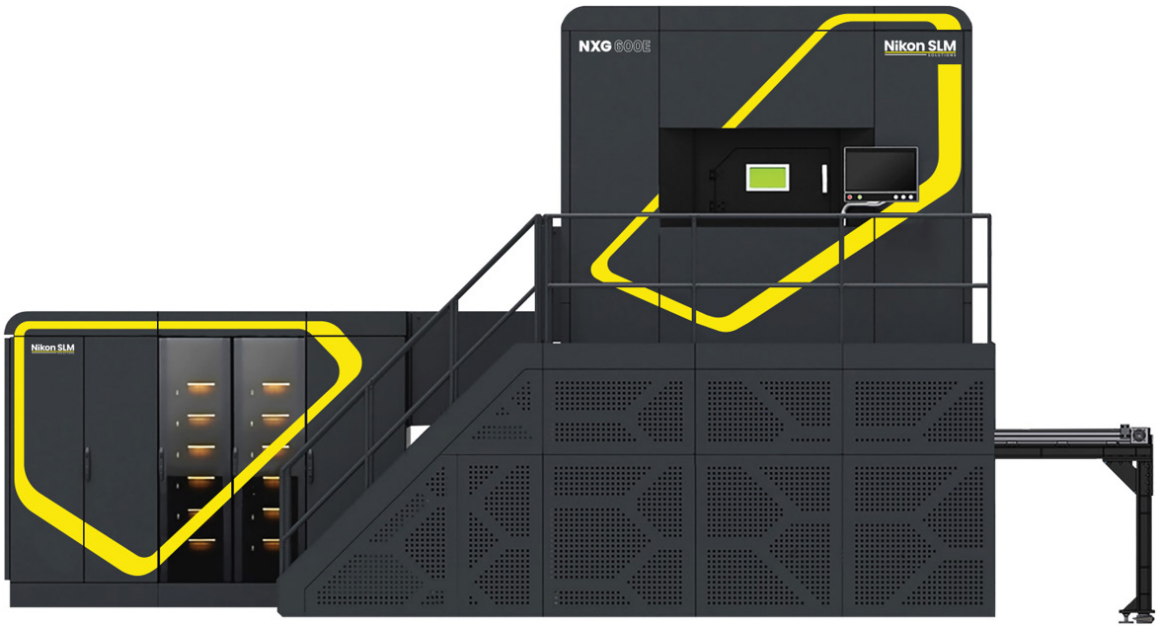


Fig. 1 Picture of the NXG 600E machine

the manufacture of components with a z-height of up to 1500 mm. This endeavor came with several technical obstacles that may seem small to the uninitiated, nevertheless posed significant challenges during the development and qualification phase.

## 2 Technology Background

The process of metal Laser Powder Bed Fusion (L-PBF) begins with a digital 3D model (as Fig. 2) of the desired part, which must be prepared accordingly to make it compatible with the generative process within the L-PBF machine. The 3D model is placed inside of a virtual representation of the machine's build envelope, while proper orientation and support structures are already considered. Next, a software processor slices this model, along with its orientation data and support structures into thousands of individual layers. These thin layers contain the cross-sectional data for a specific section of the part which is to be created. The thickness of each layer typically ranges from between 30 µm and 90 µm, depending on whether the focus lies on part quality or process speed. However, as even more productivity is desired in the future, layer thicknesses of beyond 120 µm are already used.

The finalized data is transferred to the L-PBF machine, where the selective melting procedure occurs in a controlled inert gas environment, preventing oxidation (Fig. 3). This procedure begins with the spreading of a fine metal powder layer onto a build platform (Substrate Plate) by the Recoater. Afterwards, one or multiple high-powered lasers, guided by

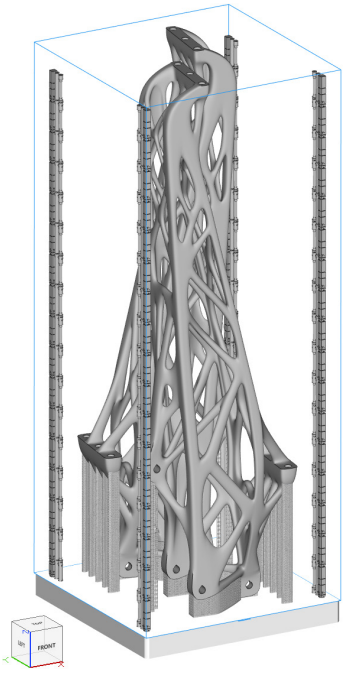

Fig. 2 A 3D model being prepared for layer generation

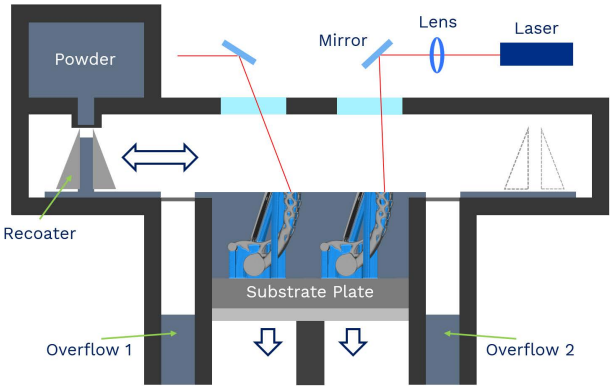


Fig. 3 Layout of a typical L-PBF machine process chamber

Fig. 4 Active laser exposure of metal powder within the NXG 600E machine process chamber

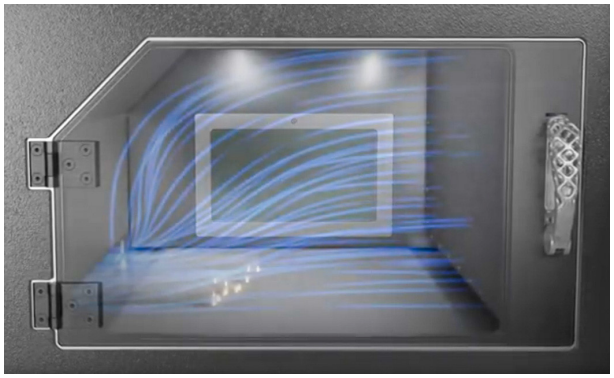

Fig. 5 Laminar shield gas flow within the sealed process chamber

individually controlled mirrors, selectively melt the powder according to the individual cross sections of the digital model. As the lasers move across the powder on the build platform, they fuse melted metal particles together, forming a solid cross-section of the part. Powder which is not melted remains loose and can be reclaimed later for a future process. The build platform then descends by the thickness of one layer and new metal powder is spread on top. Laser exposure of powder material again occurs as in the previous sequence, now guided by the data from the next part cross-section. Each new cross-section is solidified and fused with the solidified sections from previous layers, allowing the metal part to grow vertically as the L-PBF process continues.

Figure 4 shows active laser exposure of metal powder within the NXG 600E machine process chamber. This layer-by-layer procedure is repeated until the entire part is fabricated. Any required support structures are generated simultaneously to prevent the deformation of complex geometries. After completion, the part is removed from the L-PBF machine and undergoes post-processing steps such as unpacking, support removal, and heat treatment. Machining for dimensional accuracy, as well as surface finishing for desired surface qualities can also be completed separately. The result is a high-precision, complex metal part ready for use in various industries like aerospace, automotive, medical, and more. The concept of additive part generation sounds simple but each step along the process chain poses unique technical challenges, all of which had to be approached in a new way for the large-scale printer NXG 600E.

## 3 Challenges to Overcome for Large-scale Metal AM

### 3.1. Multi-laser Segmentation and Alignment

For Data preparation, new algorithms needed to be developed and validated to handle the complex task of assigning segments of the individual part cross sections to one or more of the 12 lasers. The goal here was to find the fastest melting strategy to satisfy the highest demands for part quality properties. Another factor that plays into these quality characteristics is the ability to accurately align each of the 12 lasers to one another so that they melt the powder at precisely the location which they are being instructed to travel to. For this purpose, a novel alignment method was developed which guarantees flawless build quality and reduces risks from optical drifts. The result is that each position of the process chamber's build area can be reached by accurately aligned lasers, enabling a laser utilization of up to 100%.

### 3.2. Process Stability within Each Layer

Another technological feat to achieve was designing a large process chamber that would be able to contain a stable shield gas environment in which 12 lasers could melt the powder material consistently. Figure 5 shows laminar shield gas flow within the sealed process chamber. Build chamber sizes are not infinitely scalable; lower gas flow stability will require a reduction in laser power and thus productivity. During melting, a large amount of soot and sparks are generated which need to be ejected from the process chamber via a steady gas flow. The way the lasers move to melt the powder is calculated very precisely so that none of the soot from one active laser exposure travels into the region of another. For these calculations to be feasible and predictable, the gas flow must be laminar and persistent during the entire run-time of multiple days or even weeks. Generating a laminar flow is very difficult to ensure over such a large build area of 600 mm x 600 mm. Nikon SLM Solutions already began developing new shield gas flow principles for their smaller machines, incorporating a patented sintered wall technology which was enhanced and further optimized for the NXG XII 600 platform.

Fig. 6 Two 1500 mm tall jet engine pylons, made of nickel alloy In718, produced within 169 hours

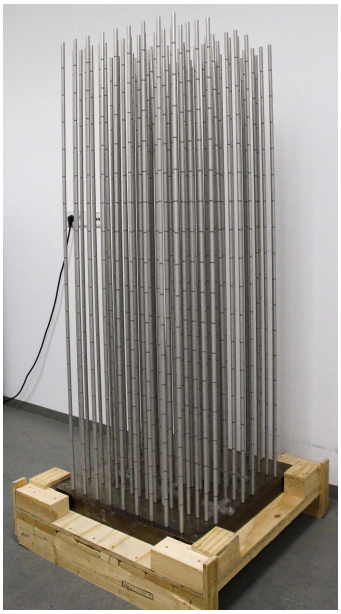

Fig. 7 Seventeen vertically stacked sample part levels from a single NXG 600E L-PBF process

### 3.3. Process Stability across 25.000 Layers

A controlled melting procedure within each individual layer is not enough. An industrial scale metal additive manufacturing machine must also deliver a stable process which can be kept consistent over tens of thousands of layers. For a standard NXG XII 600 with a build envelope of 600 mm x 600 mm x 600 mm this was already very challenging, as the extracted build job after production includes a finished part and loose powder with a combined weight of over 2000 kg. Figure 6 is a photo of built parts. When extending the z-height for the NXG 600E to 1500 mm, the maximum weight could exceed 5000 kg. This has severe implications for both the accuracy level within each layer, as well as the structural integrity requirements for the entire system as a whole unit. Typically, extending the z-height of a metal additive manufacturing system is simple to achieve because the process chamber and optical components do not need to be changed. However, at this scale, the z-drive robustness and overall machine architecture also required additional consideration.

### 3.4. Part Characteristics Consistency

The result of the previously elaborated process and machine characteristics combined is a solidified metal part which needs to perform as desired in a variety of different scenarios. These applications can vary widely in their needs for alloy composition and geometrical complexity, resulting in increased capability needs for the AM system. Depending on how well factors like laser alignment, gas flow stability, process stability are fine-tuned to one another, the solidified part may display varied levels of mechanical strength, elongation at break or surface quality. Such a variability is undesired, as the expectation is that the part will feature a level of homogeneity across its entire z-height. To ensure customer expectations are met, Nikon SLM Solutions carried out rigorous material parameter and process validations during the development of the NXG 600E using stacked sample parts as Fig. 7. This approach will be elaborated in the following chapter.

## 4 Testing and Validation of Process Stability

### 4.1. Laser Allocation Strategies

Wherever any laser melts powder material, large amounts of soot and spatter ejections will form. These pose a risk to the overall process stability, as well as part characteristics and therefore need to be removed by the shield gas flow. Naturally, any soot and spatter travelling downstream towards the gas flow outlet may also interact with exposure areas from other lasers. To prevent this, characteristics of soot and spatter creation need to be predicted, as well as the travel trajectory towards the gas flow outlet. This is a general problem of the metal L-PBF technology that Nikon SLM Solutions overcame with optimized machine design experience, accrued over the last 3 decades.

During the NXG XII 600 early development phase, testing with only 6 lasers was performed to understand the complex interactions between fume and spatter, which increase tremendously with every added laser. The following study was divided into a first setup where all 6 lasers were exposing a

(a)

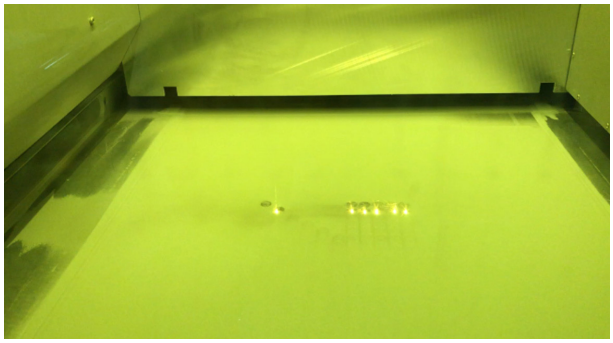

Fig. 8a Six lasers exposing synchronously with maximum soot and spatter interaction

(b)

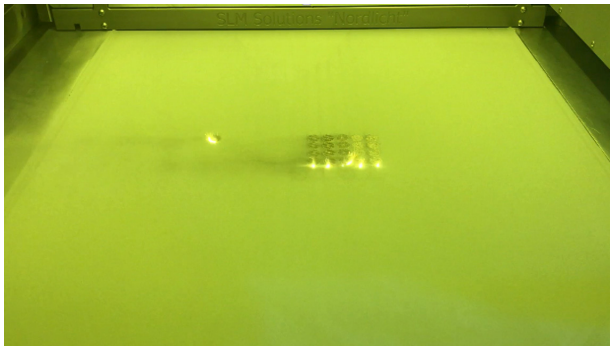

Fig. 8b Asynchronous exposure leading to less soot and spatter interaction for

(a)

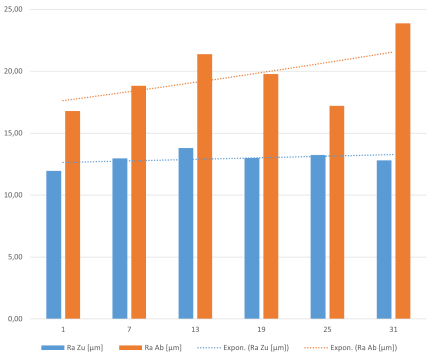


(b)

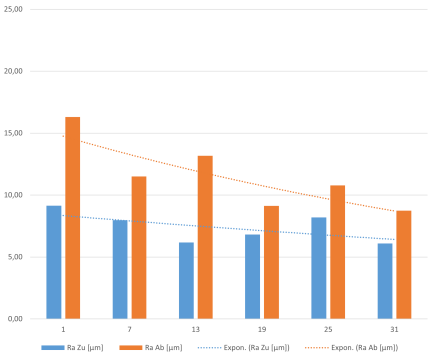


(c)

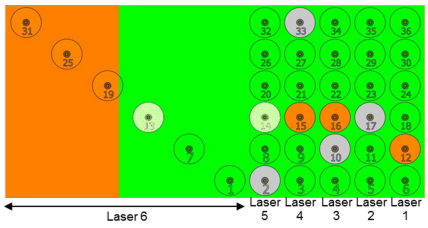


Fig. 9 Roughness (a) increases/(b) decreases with the distance for (a) synchronous/(b) asynchronous exposure and (c) Sample distribution for the test setup

secluded area of powder synchronously (Fig. 8a) and into a second setup which features asynchronous exposure (Fig. 8b). In both cases, the performance characteristics of the laser furthest to the left were observed. During the first setup, the exposure from the laser on the left side is heavily influenced by soot and spatter ejections from the remaining lasers on the right side. As shown in the figure below, the distance of the 5 lasers further to the right side was then increased significantly for the second test setup. The left laser was subsequently only influenced by spatter on the powder bed and no longer by any foreign soot ejections.

The results of a detailed sample analysis show that surface roughness on the part which was exposed by the laser on the left side increases significantly for synchronous exposure (Fig. 9a and Fig. 9b). Figure 9c is a sample distribution. When the distance between laser exposure areas is increased (asynchronous approach), surface roughness decreases to a level which users of the L-PBF technology are familiar with.

However, in a real production scenario, the highest possible level of quality needs to be achieved on all parts and samples. The assessment of multiple individual part cross-sections for each layer and how to allocate the 12 lasers is a complex task which only very advanced software algorithms can solve. For use in serial production scenarios, the goal was not only to achieve best part quality but also to minimize overall exposure time. Lower exposure times result in lower cost per part and make the entire process viable. As emphasized by the test setup above, a maximized utilization rate for all 12 lasers is desired. A high amount of additional test scenarios were conducted to acquire more data which could be used to derive the best laser allocation algorithms.

The result is a variety of strategies that can be chosen during the data preparation phase. Different scanner allocation strategy options need to be made available, due to the high amount of unique cross-section characteristics that differ from one application to the next. The outcome of maximizing either productivity or part quality will vary greatly, even for the same part.

- Maximized productivity and less quality (fastest scanning time)
- Mixture of high productivity and high quality (+35% scanning time)
- Maximized quality and low productivity (+90% scanning time)

Ultimately, the goal was to offer users of the L-PBF

technology a spectrum of scanner allocation approaches, eliminating the need for compromises.

### 4.2. Gas Flow Optimization for Laminar Flow

The task of managing up to 12 individual lasers and their interactions could only be achieved if the underlying process conditions were managed in a consistent and repeatable way. Therefore, it was crucial to supply the process chamber with a highly laminar shield gas flow across the entire powder bed. An active shield gas flow within a metal L-PBF machine's process chamber has been used since the technology was first developed. However, as the number of lasers increased steadily, new approaches had to be found to prevent the need for sacrificing part quality for higher productivity.

Initially, the shield gas was introduced from one side of the process chamber via two separate inlets. One inlet was located at the bottom of the chamber, to produce a stable flow across the powder bed, while the second inlet was located towards the top of the chamber, to prevent soot ejections from reaching the area where the laser enters the chamber. Both gas streams exit the chamber through an outlet located at the bottom of the opposite side, carrying soot and spatter ejections with them. This setup however contains flaws that become more apparent when the number of lasers increases. The two separate streams do not cover the entire z-height of the chamber and a turbulent zone with considerable back flow starts to form in the center of the chamber. A simulation of this inlet setup can be seen in Fig. 10a, where gas enters the chamber on the right and exits at the left.

With multiple active exposure areas, soot will have the opportunity to accumulate in this turbulent zone before it is ejected. The result is a temporary 'soot cloud' formation which lasers will have to pass through before reaching the powder bed. This effectively causes a decreased amount of laser power to arrive where it is needed for melting, leading to an unstable exposure process and inconsistent part properties.

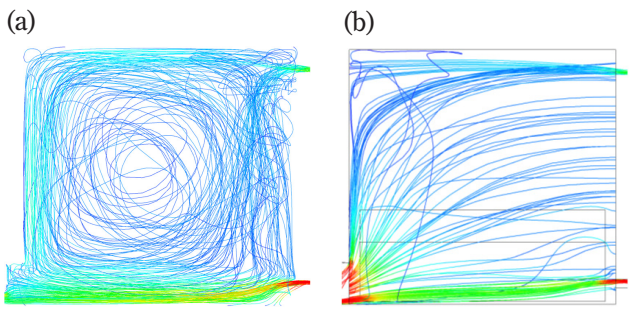


Fig. 10 (a)Turbulent gas flow resulting from two separate inlets, (b) Laminar gas flow resulting from sintered wall inlet approach

Nikon SLM Solutions already tackled the investigation into alternative shield gas flow principles prior to the development of the NXG XII 600. The solution was to ensure a steady gas flow via the entire z-height, as opposed to only at the very top and bottom. This was achieved by incorporating a patented sintered wall technology, where the gas flow inlet itself comprises a major part of one process chamber wall. Figure 10b shows a gas flow simulation which includes only a reduced amount of additional inlet points in the middle of the right wall. The difference in process chamber environment quality is obvious. The turbulent zone in the middle can be eliminated effectively.

Even though this approach was already implemented on smaller L-PBF machines such as the SLM®280 and SLM®500, an identical setup could not be adapted without major modifications. Previously, the distance which the laminar gas stream covered was only around 280 mm. With the increased size of the NXG XII 600 process chamber, a highly laminar flow had to be ensured over a distance of 600 mm.

The chosen approach was to iteratively design, simulate, build, and test various process chamber configurations in virtual and real-life environments. This process contained multiple stages, comprised of complex design adaptations, individual unit and system tests. In summation, the targeted performance characteristics to optimize revolved around three aspects:

- Achieving a highly homogenous flow profile in y-direction (process chamber front to back)
- Minimizing the gas flow speed reduction above the powder in x-direction (as it travels from inlet to outlet)
- Eliminating the risk for laser inlet contamination at the top of the process chamber

Multiple variables for each property needed to be assessed individually and in combination. These variables included but were not limited to gas inlet geometry, gas outlet geometry, process chamber design, gas volume flow rate, background gas flow design, as well as distribution between background flow and lower jet flow. One additional design guideline was the need to remove all unnecessary obstacles to the gas, for the purpose of isolating dead cavities. The result was a highly symmetric chamber where even the streamlined powder Recoater has a hidden parking position in both back and front positions, so as not to disturb the overall flow.

Figure 11a-c demonstrates the iterative process, where

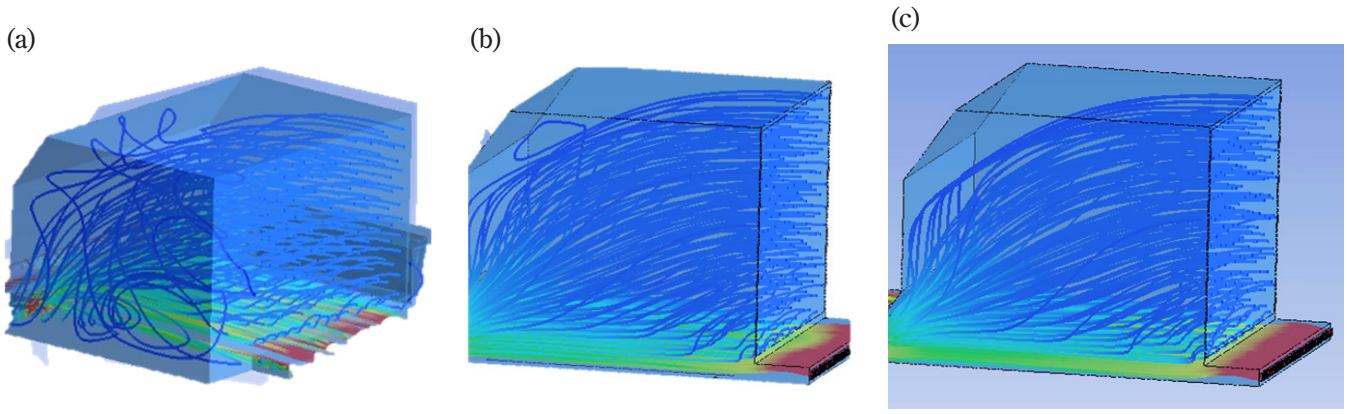


Fig. 11 (a) Simulation results of the unchanged inlet concept applied to a large process chamber, (b) Redesigned gas flow inlet leads to significant improvements in laminar flow (c) Redesigned gas flow outlet further reduces drop in speed and backpressure effects

different development stages can be compared. Initially, the existing sintered wall technology from smaller L-PBF systems was applied to the enlarged process chamber of the NXG XII 600, with less-than-optimal results (Fig. 11a). After continuously improving the inlet geometry, gas flow homogeneity in y-direction was greatly improved and the risk for laser inlet contamination was reduced (Fig. 11b). However, the overall backflow characteristics and decreasing gas flow speed profile were not yet satisfactory. To achieve the desired state, several modifications needed to be made to both the gas flow outlet, as well as the process chamber wall located closest to the outlet. Testing was conducted over a period of several years, with the result being a homogenous gas flow profile in x- and y-direction (Fig. 11c).

### 4.3. Z-Drive Accuracy and Structural Integrity

In addition to overcoming technical challenges influencing stability and productivity within a single cross-section exposure, consistent performance and part quality over thousands of layers had to be achieved. With the development of the even larger NXG 600E, the total z-height of the build envelope was increased from 600 mm to 1500 mm, resulting in an increase from 10.000 to 25.000 individual layers for a slice thickness of 60 µm. To make this feasible, two separate aspects were investigated:

- Z-Drive accuracy during substrate plate movement from one layer to the next
- Structural integrity of the NXG system frame for increased total load

For the investigation of the first aspect, clear requirements had to be established to what level of accuracy repeated substrate plate movements needed to be achieved. Ultimately, the desired precision had to be reflected in the additively manufactured metal part, as opposed to just the L-PBF machine itself. The expectation from users of this technology is that the 3D part model can be replicated to a specific tolerance level that is defined within an ISO standard. Therefore, part accuracy in terms of permissible length deviation was defined according to class F of DIN ISO 2768-1. With regards to straightness, this was specified in accordance with class H of DIN ISO 2768-2. The main influencing factor here was the Z-Drive responsible for moving the substrate plate. To verify that the chosen Z-Drive could achieve high demands for movement accuracy under complex loads, a laser interferometer was used to measure incremental movements in all positions along the z-axis (Fig. 12, 13).

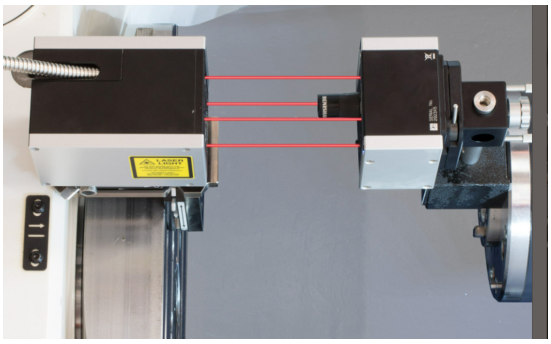

Fig. 12 XM-60 laser interferometer

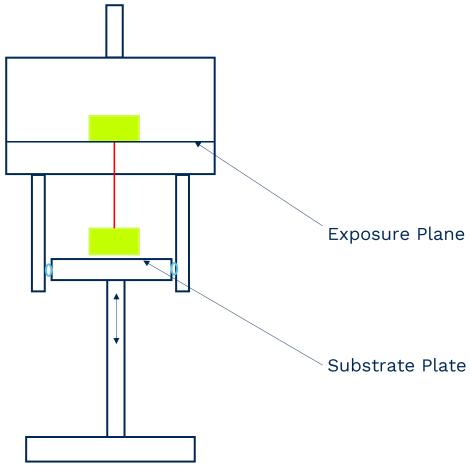


Fig. 13 Schematic representation of the test setup with laser interferometer

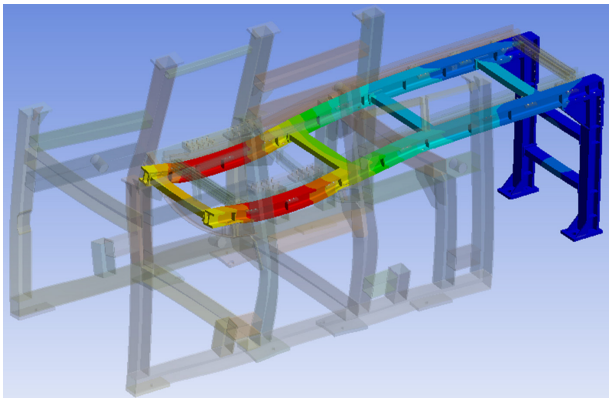

Fig. 14 Structural deformation calculation results from finite element method

Additionally, the accuracy measurements were also carried out for both the x-axis and y-axis along the full stroke of 1500 mm.

The measurements confirmed that Z-Drive accuracy was well within class F and H specifications, in accordance with DIN ISO 2678. One remaining influence on final part accuracy is the resulting material shrinkage after cool-down occurs towards the end of the L-PBF process. Luckily, this factor can be mitigated by rescaling the 3D model before it is sliced into individual layers, thus decoupling shrinkage compensation from the actual machine hardware.

For the investigation of the second aspect, structural integrity, ample use was made of finite element analysis tools shown as Fig. 14 to perform calculations on key structural components within the NXG 600E. This was crucial, as many components are affected by the increased build envelope, including those which had to be moved into and out of the system regularly, such as the build cylinder and plate package. Overall, the total load to be handled safely could reach 52.3 kN or 5334 kg, while the maximum allowed deformation for continuous and safe operation should not surpass 0.5 mm. As an example, the simulation results for the track are shown in Fig. 15. This track is needed to transport the build cylinder (containing the finished part) from inside of the machine to the external extraction location.

### 4.4. Analysis of Part Consistency

As previously demonstrated, a variety of technical innovations were developed to increase productivity, reliability, and repeatability within the metal L-PBF process. The final step was to validate that all innovations were operating in tandem to not only allow for the entire process to run in a stable manner for weeks without interruption, but also to guarantee that the solidified metal parts met the high expectations regarding part characteristics. A rigorous procedure to

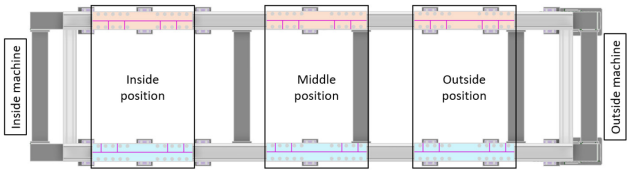


Fig. 15 Deformation positions along the linear track from inside to outside position

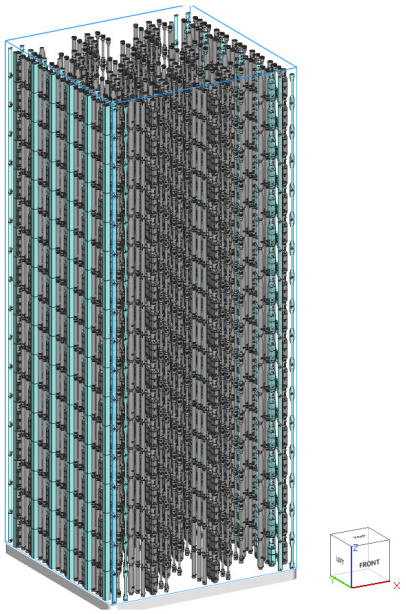


Fig. 16 Seventeen vertically stacked sample part levels, over 1800 individual samples in total

develop, test and validate unique part generation parameters had to be carried out within each alloy category, that either focused on part quality or productivity. For the sake of simplification, the following descriptions and tables will only showcase the approach and results for Inconel 718 and a single parameter variant which features a balance between highest part characteristics and productivity. Furthermore, sample parts were subjected to three different heat treatment profiles:

- No heat treatment, machined surface
- Solution annealing + aging, machined surface
- Hot isostatic pressing + solution annealing + aging, machined surface

The showcased sample results are those which were solution annealed and aged as per AMS 2774 S1750DP. Emphasis was placed on ensuring that the entire NXG 600E build envelope across its full height of 1500 mm was assessed. For this purpose, the sample generation was repeated over 17 individual levels, which each feature the same specimen geometries and layout in x and y directions. These layers can be seen in Fig. 16 (corresponding to Fig. 7).

In this process, the main focus was placed mainly on part density, hardness, and tensile properties. These characteris-

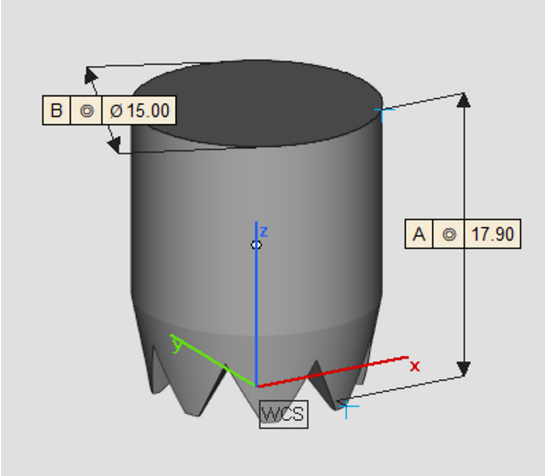


Fig. 17 3D models of a standardized CT specimen

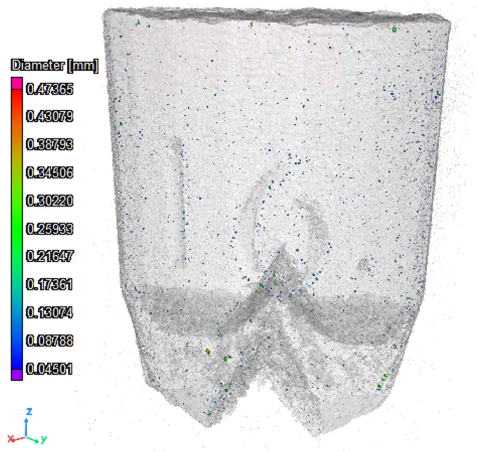


Fig. 18 Visual representation of Micro-CT results for a single specimen

tics are crucial to ensure the highest quality of additional secondary properties, which could be investigated at a later stage.

For density investigations, ample use was made of non-destructive material testing, in which information on external and internal defects was acquired. Potential defects include porosities and inclusions, among others. One such technology is Micro-CT, for which hundreds of CT-specimens (Fig. 17, 18) were scrutinized down to a voxel size of just 15 µm, enabling the detectability of anomalies down to 45 µm. This is sufficient to identify defects or inclusions with serious implications for a solidified part's long-term stability. To accelerate the analysis of hundreds of specimens, an automatic sample changer was utilized, which allowed up to 63 samples to be run in one single batch. For each sample, the result was an elaborate report offering insights into the total number of pores, pore sizes, pore distribution, sphericity characteristics of individual pores, and pore distance to the part surface. Additionally, localized porosity hotspots were visualized, in which a pre-defined porosity threshold is exceeded. This was then assessed to enable further fine tuning of L-PBF process parameters for either maximized productivity or part density. Figure 19 shows a histogram of density distributions for one sample level, where a MEAN value of 99,97% was achieved. This corresponds very well to

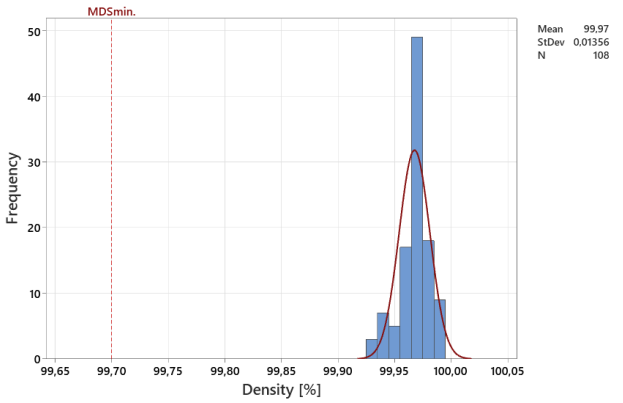


Fig. 19 Histogram of Density [%]

the sample analysis of all remaining levels from the same L-PBF process.

For the validation of tensile properties and hardness, each level within the previous layout features over 60 dedicated samples that can be subjected to multiple tests. The main characteristics of interest were Ultimate Tensile Strength (UTS), Yield Strength (YLD), Elongation at Break, and Hardness. As can be seen from the results in Fig. 20a-d, the L-PBF process within the NXG 600E delivers highly stable properties over the full build height in each level, especially for UTS and Elongation. Within the narrow distribution of mechanical properties, there is no upwards trend visible, the standard deviation also behaves consistently from one level

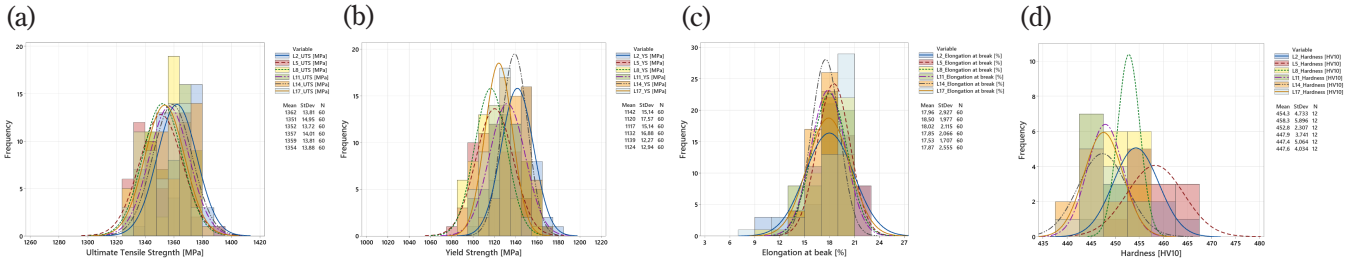


Fig. 20 Histograms of (a) Ultimate Tensile Strength, (b) Yield Strength, (c) Elongation, (d) Hardness

to the next. Furthermore, Vickers testing across all sample levels reveals a high degree of overlap in hardness with low anisotropy characteristics. This is a testament to the overall homogeneity within the machine's technological capabilities, resulting from years of testing and iterative improvements.

## 5 Conclusion

The NXG 600E expands on the initial capabilities of the NXG XII 600 system to deliver state-of-the-art productivity, reliability, output quality and will accelerate the adoption of L-PBF technologies across a variety of industries such as aerospace, automotive, defense, energy and healthcare. Through rigorous testing and design validation procedures, innovative solutions for multi-laser alignment, laminar gas flow generation and part consistency management were incorporated without sacrificing process performance or part characteristics. By pushing the boundaries of existing technology approaches within the L-PBF process, Nikon SLM Solutions will continue to develop products which exceed customer expectations and enable the use of AM technologies for novel applications in entirely new industries.

Sebastian FEIST
Nikon SLM Solutions AG

Daniel BRÜCK
Nikon SLM Solutions AG

Christoph WANGENHEIM
Nikon SLM Solutions AG

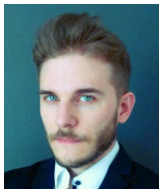
Sebastian FEIST


Daniel BRÜCK


Christoph WANGENHEIM

# ニコン「NIKKOR Z 400mm f/2.8 TC VR S」「NIKKOR Z 600mm f/4 TC VR S」の開発

猪原祐治，山下雅史，坂本祐輔

# Development of the 'NIKKOR Z 400mm f/2.8 TC VR S' 'NIKKOR Z 600mm f/4 TC VR S'

Yuji IHARA, Masashi YAMASHITA and Yusuke SAKAMOTO

ニコンの最先端技術を結集させ，高解像と美しいボケ味による臨場感あふれる描写力と高速・高精度オートフォーカスを備えた，テレコンバーター内蔵大口径超望遠レンズ「NIKKOR Z 400mm f/2.8 TC VR S」「NIKKOR Z 600mm f/4 TC VR S」をそれぞれ2022年 2 月，2022年11月に発売した．ここでは，上記 2 製品の様々な開発要素について説明する．

In 2022, we launched 2 super-telephoto prime lenses with built-in teleconverter, NIKKOR Z 400mm f/2.8 TC VR S and NIKKOR Z 600mm f/4 TC VR S. With cutting edge NIKKOR technologies, we provide photographers outstanding quality pictures that has high resolution and smooth bokeh. Furthermore, the newly developed high speed and high accurate VCM makes sure of that.

In this paper, we introduce some stories developing these lenses, technical features and backgrounds.

**Key words** ニコン Z マウント，交換レンズ，超望遠レンズ，内蔵テレコンバーター，VCM
Nikon Z mount, interchangeable lens, super-telephoto lens, built-in teleconverter, VCM

## 1 Introduction

In 2022, Nikon released two Z-mount super-telephoto prime lenses designated as "NIKKOR Z 400mm f/2.8 TC VR S" (hereinafter, "Z400/2.8") and "NIKKOR Z 600mm f/4 TC VR S" (hereinafter, Z600/4) (Fig. 1). Both these lenses, i.e., the Z400/2.8 and Z600/4, are equipped with a built-in 1.4x teleconverter, whereby the Z400/2.8 is able to switch between focal lengths 400 and 560mm, and the Z600/4 is able to switch between focal lengths 600 and 840mm.

Fig. 1 Top: NIKKOR Z 400mm f/2.8 TC VR S
Bottom: NIKKOR Z 600mm f/4 TC VR S

## 2 Background of the Built-in Teleconverter

Most telephoto lens use cases involve the application of a teleconverter for extending the focal length. In such cases, it becomes necessary to insert a general-purpose external teleconverter between the lens and camera body after removing them. This kind of setup changes have the potential to result in missed photo opportunities while shooting in the field. Additionally, these changes need to be done with care, particularly during bad weather, to prevent the ingress of moisture into the camera body and avoid water particles on the lens. Therefore, professional photographers always preferred built-in teleconverters for telephoto lenses. To meet this demand, Nikon adopted a built-in teleconverter in the F-mount zoom lens "AF-S NIKKOR 180–400mm f/4E TC1.4 FL ED VR." However, there was similar demand for such installation in prime lenses as well.

The photograph (Fig. 3) depicts a photographer holding the Z400/2.8 attached to a Z9. The built-in teleconverter switch is located on the right-hand side camera grip (Fig. 2). Placing the switch at a location where it can be operated with the middle finger of the right hand facilitates switching

the built-in teleconverter on and off while maintaining the shooting posture. Moreover, regardless of whether the built-in teleconverter is used or not, the user can continue to handle the lens in the usual manner when shooting in the field because the overall length and center of gravity of the lens remain unaltered.

In addition to ease of handling, the built-in teleconverter has a distinct advantage over general-purpose teleconverters in terms of performance. Most often, external teleconverters are designed to maintain the same performance as that of the lens to which they can be attached, whereas built-in teleconverters are designed specifically to match the performance of the specific model of the lens, thereby ensuring improved design performance. Moreover, various adjustments, such as the focus adjustment and the resolution performance inspections, are conducted during the production process for both scenarios, i.e., when the built-in teleconverter is in use and when not in use, to ensure high-quality photographs can be captured regardless of whether the built-in teleconverter is used or not.


Fig. 2　Built-in teleconverter switch

Fig. 3　Handheld shooting using Z400/2.8 and Z9

## 3 Achieving Both Robustness and Light Weight

During the development of these two lenses, another theme that was emphasized, similar to the inclusion of a built-in teleconverter, was the light weight of the lens barrel. A light weight super-telephoto prime lens is a major advantage during field work as well as with transporting the equipment. The new lenses are approximately 850 and 550 g lighter than the current F-mount models AF-S NIKKOR 400mm f/2.8 FL ED VR (hereinafter, AF-S400/2.8) and AF-S NIKKOR 600mm f/4 FL ED VR (hereinafter, AF-S600/4), respectively.

Developing light weight equipment required the camera system that retains the high image quality and robustness that NIKKOR lenses have cultivated over the years and can be relied upon by photographers. Hence, close attention was given to these aspects.

The structure itself was reviewed relative to conventional lens barrel structures, and the number of parts was reduced while the weight of the parts themselves was also reduced. A key aspect here was the simulation technology that applied data that were aggregated through development and verification activities in the past. This technology and data were utilized to select the parts thicknesses, determine structural strength, and validate appropriate material choice for these purposes to realize a product that was both lightweight and robustness.

For example, reducing the weight of a part requires either reducing its volume or density. Simply reducing the parts thickness will decrease rigidity, and selecting materials with low density will decrease the Young's modulus. Therefore, we attempted to balance the density and Young's modulus by effectively utilizing a combination of several materials, such as aluminum alloys, magnesium alloys, and engineered plastics. This was accomplished by conducting strength analysis repeatedly during the development process using simulations by optimizing material thickness while maintaining structural strength.

Finally, impact tests were carried out with a prototype to confirm the accuracy of the simulations and to guarantee the required strength that is expected when in the hands of users. These investigations aided us in realizing a significantly light weight product while maintaining the robustness, which is the unique selling proposition (USP) of Nikon products, as well as the reliability of Nikon tools that has been cultivated over the several decades.

## 4 Issues with Built-in Teleconverter and Z Mount

The shift from the F mount to the Z mount necessitated significant revamping of the optical design. This was neces-

sary to maintain an appropriate overall length of the lens barrel and to reduce the weight.

The existence of a Z mount has both advantages and disadvantages in terms of achieving a built-in teleconverter.

One advantage with the Z mount is that the mount aperture becomes larger, which enables more peripheral light to be captured even when a built-in teleconverter is installed.

On the other hand, the increased overall length of the lens barrel due to the short flange back is a disadvantage because it not only increases the mass but also makes its handling more difficult. Certain professional photographic equipment, such as the lenses and camera bodies, are very expensive, and obviously, users are quite concerned about their loss, theft, or damage during transportation.

Consequently, there is strong user demand for carrying lenses on board as carry-on luggage during air travel. This demand is particularly high for expensive super-telephoto lenses. Therefore, lenses that are compact enough to fit in carry-on bags are highly sought after.

However, simply shortening the overall lens barrel length would require each lens to have improved convergence power, which in turn could result in increased mass and compromise its optical performance. Here, the distance from the front lens to the sensor is called the total optical length, and the value obtained by dividing the total optical length by the focal length is called the telephoto ratio. A lower telephoto ratio results in higher aberration caused by the power that converges the light rays, and aberration correction becomes more difficult. Additionally, increasing the convergence power involves approaches such as reducing the radius of curvature of the lens and increasing the refractive index of the glass used in the lens. However, the former approach has a tendency to increase the volume, whereas the latter has a tendency to increase the density of the glass. Evidently, both approaches are counterproductive from the point of view of developing light weight equipment.

In other words, it is imperative that an optimal solution needs to be devised; one that would enable realization of equipment with built-in teleconverter that are significantly lighter by weight, whose overall lens barrel length is low while maintaining improved optical performance.

## 5 Key Optical Materials and Design Approaches

Chromatic aberration correction is the key to design performance in super-telephoto lenses. Chromatic aberration is a phenomenon in which there are shifts in the image formation position of each color (wavelength) of light that passes through a lens. This shift causes the colors to appear blurry on the photograph. Various types of glass concave and convex lenses are combined in optical design to correct the image formation position of each color. In each era, materials that excel in correcting chromatic aberration, such as extra-low dispersion (ED) glass and fluorite, have been used to evolve super-telephoto lenses.

The reason for the excellent properties of materials such as ED glass and fluorite is due to their anomalous dispersion. Anomalous dispersion, in the context of the design of camera lenses that handle visible light, mainly refers to the behavior of short-wavelength light, such as blue or purple. However, ED glass and fluorite behave differently in comparison to ordinary glass. Therefore, materials with anomalous dispersion can be used in appropriate locations to effectively correct chromatic aberration from red to purple, i.e., throughout the entire visible range.

Furthermore, the present design used short-wavelength refractive (SR) glass, which is a special glass material with anomalous dispersion that has been exclusively developed by the Nikon Group. Although conventional fluorite and ED lenses are also materials with anomalous dispersion in the lower dispersion range, SR lenses have the feature of greatly refracting short-wavelength light, such as blue and purple, in the higher dispersion range. Additionally, its combination with fluorite and ED lenses allows the lens to greatly contribute to chromatic aberration correction throughout the entire visible range. Its lower density also makes it an essential material for designs that align with the current themes of light weight and high performance.

Next, the specific approach using these materials is explained. Conventional F-mount lenses have a lens with almost no refractive power at the front that has played the role of protecting the fluorite that follows. In the present case, this lens, which is made as a convex lens, is used as a combination of two convex lenses, including fluorite at the front part of the lens, adopted to reduce the aberration that occurs, as opposed to its use as a combination of a protective glass + fluorite composition. This allows the lenses that follow to be placed at a longer distance away from the two front lenses, thereby allowing a significant reduction of the lens diameter and leading to a significant reduction in volume and mass. Aberration generally worsens when the lens group in the middle part is moved backwards. However, appropriate placement of the SR lenses and super ED lenses with high aberration correction capabilities in the rear part compensates for the lack of aberration correction in the front part,

thus achieving good aberration balance for the entire optical system.

Conventional F-mount lenses use approximately three lenses in the focus group to suppress aberration fluctuations during focusing. Notably, optimizing the lens configuration closer to the object than the focus group enables the suppression of aberration fluctuations during close-up shooting, even when a focus group with fewer lenses is used. The lighter weight of the focus lens also offers more freedom in the focus actuator design, and further efforts could be made in achieving high-speed, high-precision, and quiet operation.

An important element in optical design using a built-in teleconverter is correcting aberrations not only in the entire optical system but also in the lens system as parts of a whole. Specifically, when dividing the camera system into the three parts of ① lens system that is closer to the object than the teleconverter, ② teleconverter section, and ③ camera side behind the teleconverter, this refers to the two parts ① and ②. When the teleconverter expands the focal length, it also expands the aberrations in the optical system. Suppressing the aberration fluctuations during use or non-use of the teleconverter requires suppressing the difference between the level of aberration in ① that occurs during non-use of the teleconverter and the level of aberration in ① that occurs during use of the teleconverter and that is magnified by the magnification of the teleconverter in ② along with the level of aberration in the partial system ②. High optical performance regardless of use of a teleconverter is achieved by proceeding with the design while paying attention to the aberration of the entire optical system as well as the aberration of these partial systems.

Please take a look at the actual photographs to observe the results of the aforementioned design.

The photograph (Fig. 4) exhibits a subject with splashes of water, which is generally prone to significant color bleeding, taken at 600 and 840mm using the built-in teleconverter. The proper chromatic aberration correction accomplished by the special glass allows for the splashes of water to be visible from the maximum aperture, regardless of the built-in teleconverter use. Color bleeding due to chromatic aberration is more likely to occur at shorter shooting distances, such as at 4–5 m, but photographers have praised the lens for its clear depiction regardless of shooting distance.

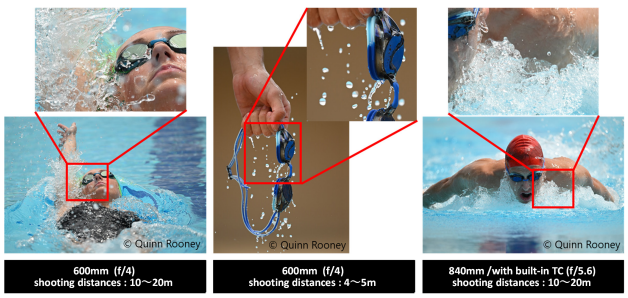


Fig. 4 Effect of chromatic aberration correction

The photograph (Fig. 5) shows the same subject taken at 600 and 840mm using the built-in teleconverter. Even subjects with fine lines, such as animal hair, are depicted in detail at the maximum aperture, with each line individually depicted, and the high resolution that was achieved can be observed regardless of the built-in teleconverter use. There is the illusion of the sheep and shoebill being right in front of the viewer. This expressive power is the appeal of the super-telephoto prime lenses to photographers, who will not be able to resist the temptation to take them out for shooting.

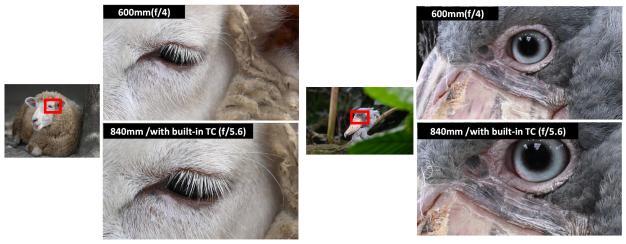


Fig. 5 Image quality when using built-in teleconverter

## 6 Development of Elemental Technologies That Support Light Weight

In parallel with the design, we investigated technologies for thinning the large-diameter lens in the front and for holding the lens in order to reduce the mass of the lens barrel.

We have previously described chromatic aberration correction during the design of super-telephoto lenses, but maintaining the precision of the lens surface during lens processing and assembly is also a very important element in the manufacturing of super-telephoto lenses. In terms of lens polishing, processing a large-diameter lens with high precision is not only technically difficult to begin with, but the desire to reduce the lens thickness for lightweight equipment further increased the processing difficulty.

There was also the issue of holding this lens securely in the lens chamber. Large-diameter lenses have a large mass themselves, so maintaining performance even when the lens is unintentionally subjected to shock or vibration during field shooting requires mechanisms and assembly conditions for holding the lens securely. The lens needs to be held with sufficient force to prevent its movement, but excessive application of force will cause lens distortion and destroy the precision of the lens surface, which may lead to a degradation of its optical performance. Determining the balance between reliability and performance is crucial here.

To achieve these efforts, we set the goals of light weight equipment and processing accuracy for the lens processing with the technical team members, and we proceeded with the design while receiving feedback from the processing experiment results and checking the balance between performance and mass. The design, manufacturing, and assembly came together for the lens holding mechanism, while simulations and prototypes were used to adopt a structure that maintained high performance while ensuring reliability.

## 7 Autofocus That Never Misses a Photo Opportunity

Fast-moving subjects such as athletes and wild animals are an indispensable element for shooting scenes with super-telephoto lenses. Super-telephoto lenses require autofocus (AF) performance for accurately capturing the precise moments of such subjects. Although summarized as "AF performance", its output is influenced by various elements. For example, to capture the instance when the ball is passed to another player in the team through a careful pass in a soccer game, the camera needs the explosive power to instantly adjust the focus and capture the scene where the player dribbles past an opponent; the camera requires the tracking power to continue capturing the irregular movement.

A major breakthrough is needed in the focusing unit when designing the present model for meeting the above-mentioned needs. There is a need for the adoption of an actuator that could drive a large lens with superior response and stop it with high precision. Maintaining higher optical performance requires having a mechanism that minimizes the tilt of the focus group. After several design configurations and prototypes, the Silky Swift VCM was born, which uses a VCM that can directly apply the driving force to the lens chamber, a guide mechanism with less backlash and friction, and high-rigidity engineered plastic (Fig. 6).

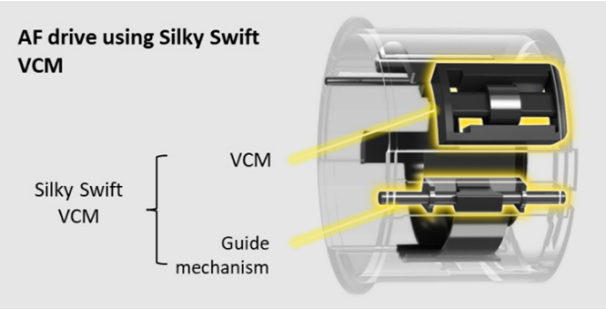


Fig. 6 Silky Swift VCM

Furthermore, the optical ABS encoder that was used as the lens position encoder detects the lens position by reading a precise scale with light, which enables position detection at a resolution approximately 20 times finer than in conventional models. The combination of this encoder with the Silky Swift VCM enables precise position control. This drive system was first installed in the focus lens of the Z400/2.8 and was later used in the Z600/4 as well, with an optimized design that matches the lens arrangement and drive specifications.

This improved the actuator performance of the focus lens, but this alone does not result in improved AF performance. AF accuracy is improved by not only the optical performance of the lens but also the cooperation of the equipment as a camera system, including the Z9's image plane phase difference AF. The combination helps improve the shooting yield of images captured when dealing with subjects that require high-speed, high-precision lens position control, such as the soccer game scenarios mentioned earlier.

## 8 Excellent Backlight Resistance

The Meso Amorphous Coat, which was first used on the Z400/2.8, is a coating comprising a unique material that was born from elemental development to achieve the highest anti-reflection performance in the history of NIKKOR lenses. The Meso Amorphous Coat has a bulky structure that is formed by connecting particles that are smaller than the Nano Crystal Coat particles to form an amorphous structure. This results in the formation of mesopores (gaps between particles) throughout the film and achieves high film porosity. A refractive index that is even lower than that of Nano Crystal Coat is achieved through the inclusion of air in these mesopores. Furthermore, the precise configuration of a bulky structure comprising fine particles enables a high-porosity, low-scattering film structure that cannot be achieved with Nano Crystal Coat in a simple manner [1].

This results in the material achieving a performance that surpasses Nano Crystal Coat, which has a high anti-reflection effect against oblique incident light. The Meso Amorphous Coat also possesses an anti-reflection effect equal to or greater than that of ARNEO Coat against directly incident light, which renders the developed material the ability to significantly reduce ghosts and flares caused by various incident light.

In the present study, we have understood the respective features of not only the newly-developed Meso Amorphous Coat but also those of the Nano Crystal Coat, ARNEO Coat, and Super Integrated Coating, and their application in the appropriate locations to reduce ghost effects. We also con-

ducted ray tracing simulations at the design stage and optimized the shape and placement of the mechanical parts to prevent ghosts and flare from those parts.


Fig. 7　Example of photograph with strong light source on screen

The photograph (Fig. 7) is an example of a silhouette of a giraffe against the backdrop of a sunset. Clear images with good clarity can be captured even in such scenes thanks to the use of the Meso Amorphous Coat and ARNEO Coat, as well as mechanical parts designed with consideration to ghosts and flare.

## 9 Operability and Mobility That Do Not Rely on Vision

The Z400/2.8 and Z600/4 were two products designed with a focus on usability that enables professional photographers to use them without stress in their daily work.

Additionally, operating parts such as the various rings, switches, and buttons are implemented. Also included are the lens-function (hereinafter, L-Fn) 2 buttons, Fn ring, control ring, focus ring, L-Fn button, various slide switches, memory set button, and built-in teleconverter switch.

These control elements are configured to provide users a variety of shooting experiences. For example, the Fn ring, installed for the first time in this model, can record different focus positions for each direction of rotation, i.e., to the left or right, and can be assigned the function of instantly calling out the focus position according to changes in the subject. Previous models allowed the focus position call-out function to be assigned to L-Fn2 buttons, but only one focus position can be called out. The present model allows the focus position to be called out with the Fn ring, so different functions such as FX/DX switching can be assigned to the L-Fn2 buttons. This significantly increases the number of compositions and scenes that can be captured while maintaining the shooting position. Assigning the high-resolution zoom to the control ring enables changes to the composition as though a zoom lens were being used, even though it is a prime lens. Since the release of these two models, we have responded to user feedback through firmware upgrades that improved the operability. One such improvement was the swapping of the focus ring and control ring functions. Operating parts have been arranged to achieve a shooting method that defies conventional wisdom, with the hope that users will explore the settings so as to be tailored to them and have a shooting experience with higher yield than ever before.

Several 3D models, prototypes, and mockups were created and tested repeatedly to enable easy operability when used either in the handheld mode or with a tripod. Through this, an arrangement of operating parts that can be used in a variety of ways was accomplished. Careful attention was paid to the design detail of the shape of the parts to ensure that the operating parts are distinguishable merely by touch rather than relying on vision. Furthermore, the operating parts of these two products are identical from the perspective of the camera. Thus, operability, which has been a particular focus of ours, is implemented in a consistent manner across both of these products.

The change in the center of gravity of the lens has also significantly contributed to mobility and handling. The lighter weight of the front lens components and mechanism parts compared to that of the F-mount AF-S400/2.8 and AF-S600/4 resulted in not only a reduced lens barrel weight but also in a significant shift of the center of gravity toward the camera. Consequently, this led to reduced force of inertia when panning the lens in handheld or monopod shooting, thereby enabling smoother changes to the composition and panning shots. Users who actually attach the lens to a camera and take handheld shots will be able to feel the effects that go beyond numbers-based weight reductions.

Even though the Z600/4 has a longer overall product length, the two models have been designed to minimize the difference in the center of gravity between them to ensure that the feel when shooting is consistent. We believe that these products are intuitive and easy to use, even for users who use both models for different occasions depending on the shooting scene.

## 10 Conclusion

The Z400/2.8 and Z600/4 are lenses that combine mobility, image quality, and functionality. Using them in combination with the built-in teleconverter renders users an enjoyable shooting experience that is similar to switching between two super-telephoto prime lenses without actually changing the equipment.

Many photographers have used these lenses and highly

praised them for their operability, image quality, AF performance, and ease of handling. We wish to continue creating products that connect users to new shooting experiences.

## References

[1] R. Suzuki, "Fabrication of a porous $SiO_2$ thin film with an ultralow refractive index for anti-reflective coatings," *J Sol-Gel Sci Technol*, vol. 106, no. 3, pp. 860–868, 2023.

猪原祐治　Yuji IHARA
光学本部 第二開発部
2nd Development Department
Optical Engineering Division

山下雅史　Masashi YAMASHITA
光学本部 第三設計部
3rd Designing Department
Optical Engineering Division

坂本祐輔　Yusuke SAKAMOTO
光学本部 第二開発部
2nd Development Department
Optical Engineering Division

猪原祐治
Yuji IHARA

山下雅史
Masashi YAMASHITA

坂本祐輔
Yusuke SAKAMOTO

# デジタル倒立顕微鏡に搭載したHCA用アプリケーションの技術と実施例の紹介

林　耕磨，門井宏平，柴田美智太郎，大井宏美，星野哲朗

# Introduction of HCA Application Technology and Examples Installed on Digital Inverted Microscopes

Kohma HAYASHI, Kohei KADOI, Michitaro SHIBATA, Hiromi OI and Tetsuro HOSHINO

創薬分野において，High Content Analysis（HCA）と呼ばれる顕微鏡観察により薬剤の効果を評価する技術は，重要性を増してきている．一方で，HCA を実施するためには，細胞培養，画像取得，解析等の高度な専門知識が必要となる．ニコンは，誰でも簡単に HCA を実施できるようにするため，デジタル倒立顕微鏡 ECLIPSE Ji と，本顕微鏡専用ソフトウェア，NIS-Elements SE（Smart Experiment）を開発した．本稿では，Smart Experiment に搭載された技術の紹介と，実際の撮像例に関して紹介する．1 章にて背景を説明し，2 章では Smart Experiment を利用したときの画像取得から解析結果表示までのシステムワークフローを紹介する．3 章では，Smart Experiment のシステムワークフローを実現するために開発した，CellFinder.ai によるオートフォーカス技術と NIS.ai による細胞セグメンテーション技術を紹介する．4 章では，Size and Morphological analysis と Cytotoxicity の実施例を紹介することで，Smart Experiment にてどのような実験結果を出力できるか示す．最後に 5 章では，本技術を振り返って，今後の展望について説明したい．

In drug discovery, High Content Analysis (HCA), a microscope-based drug efficacy evaluation screening approach, is becoming increasingly important with imaging technology development. However, performing HCA requires advanced expertise in several fields (e.g., cell culture, image acquisition, analysis, etc.). Nikon developed a digital inverted microscope, ECLIPSE Ji, and corresponding software, NIS-Elements SE (Smart Experiment), for easy HCA execution using this microscope. In this study, we introduce the technology installed in Smart Experiment, along with actual imaging examples. Chapters 1 and 2 introduce the background and workflow from image acquisition to analysis result display when using Smart Experiment, respectively. Chapter 3 discusses the autofocus and cell segmentation technologies by CellFinder.ai and NIS.ai, respectively (both developed to realize Smart Experiment). Chapter 4 presents size and morphological analyses as well as cytotoxicity examples as actual assays. Finally, Chapter 5 provides a future outlook.

**Key words** 顕微鏡，深層学習，自動化，ライフサイエンス，創薬
microscope, deep learning, automation, life science, drug discovery

## 1 Introduction

Image analysis techniques for evaluating the effects of drugs through microscopic observation are known as high content analysis (HCA). Conducting HCA, which requires various advanced expertise, is becoming increasingly important in the field of drug discovery alongside developments in imaging technology [1]. Expertise requirements include knowledge of preparing cell samples and constructing experimental systems for drug evaluation, knowledge of acquiring quantitative microscopic images, knowledge of image processing to extract features from captured images, and knowledge of statistical analysis to present drug effects from the extracted features. Given the need for such complex knowledge, HCA has the problem of having high barriers to entry for those who are conducting it for the first time. Nikon has sought to solve this problem by developing a digital inverted microscope called ECLIPSE Ji and software dedicated to this microscope called NIS-Elements SE (Smart Experiment) as a system for automating the complex workflow involved in conducting HCA. In this paper, we introduce the technologies installed in Smart Experiment and demonstrate an actual example of conducting HCA.

## 2 Smart Experiment System Workflow

In this section, we briefly introduce the Smart Experiment system workflow. In NIS-Elements SE, the imaging and analysis proceed according to the system workflow depicted in Fig. 1 so that the user can conduct the assay without having to configure various settings. Each step is explained below.

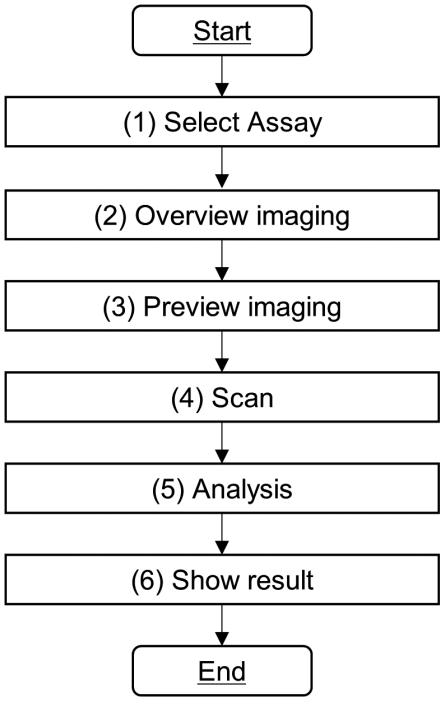


Fig. 1 Smart Experiment workflow overview

**(1) Select Assay**

After initial preparation of the sample, it is mounted on the stage of Ji and the corresponding assay is selected from the SE mode of NIS-Elements.

**(2) Overview Imaging**

The system determines how many wells the sample placed by the user is in, and the XY tilt of the plate is corrected.

An image is acquired at the center of each well to detect the presence of cells. Next, the cell density and the bias within the field of view of this image are analyzed to detect the optimal field of view for high-magnification observation.

**(3) Preview Imaging**

Subsequently, automatic illumination condition adjustment is conducted using AI (Autosignal.ai), either for the wells selected by the user or for all the wells within the imaging range. This result is used as a basis to calculate the illumination conditions (LED power, exposure time) that will not saturate the brightness of the brightest well among the scanned wells. Autofocus is also conducted in the bright field on the first well to be scanned initially; subsequently, autofocus is conducted for each fluorescent channel of the images. These autofocus results are used to calculate the offset value between the focal position in the bright field caused by axial chromatic aberration and the focal position for each fluorescent channel. AI-based bright field autofocus (CellFinder.ai) is used to calculate the bright field focus.

**(4) Scan**

The image to be used for analysis is acquired using the XY position determined in *Overview Imaging*, the illumination conditions determined in *Preview Imaging*, and the offset value of each fluorescent channel from the bright field.

**(5) Analysis**

The analysis recipe defined for each assay is executed for the image captured during *Scan* step.

**(6) Show Result**

Finally, the analysis results are displayed on the result display screen.

## 3 AI Technologies used in Smart Experiment

In this section, we introduce the AI technologies installed in Smart Experiment.

### 3.1. Autofocus by CellFinder.ai

#### 3.1.1. Principle Overview

Conventional autofocus methods used in microscopes follow a method in which the focal plane is determined from the brightness information of each image while acquiring images in the Z direction. The conventional method requires the focal plane to be within the Z operation range, so an appropriate Z range must be set in advance. When this range is narrow, the Z operation will not reach the focal plane, leading to autofocus failure. Conversely, when the Z range is set too wide, the autofocus process lasts unnecessarily over a long time.

We avoided the above issues by developing a new autofocus method for Smart Experiment. As shown in Fig. 2, this method uses a procedure for estimating the distance to the focal plane from two images with different Z positions. A deep neural network (DNN) is used for estimating the focal plane.

#### 3.1.2. Training Method

Z-stack images were acquired for each objective lens, and the distance to the focal plane was labeled for two images with different Z positions for learning. The cell types in Table 1 were used for training. The focal plane in the bright field observation was defined as the Z position where the contrast was at a local minimum.

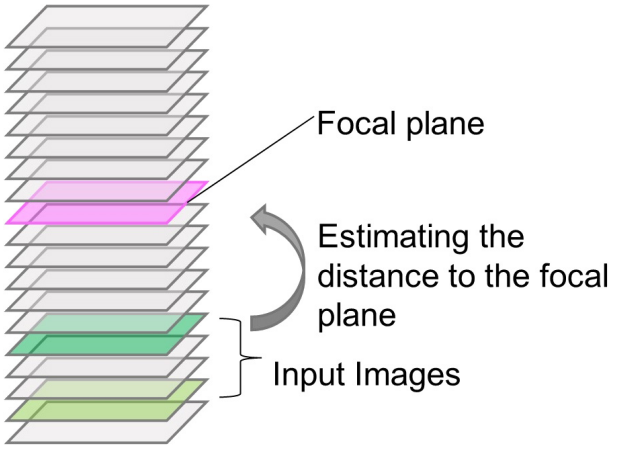


Fig. 2 Principle of CellFinder.ai

Table 1 The cell types used for CellFinder.ai

| Cell Type | Origin |
|---|---|
| **HeLa** | RIKEN BRC, RCB0007 |
| **HepG2** | JRCB cell bank, JCRB1054 |
| **HT-29** | ATCC, HTB-38 |
| **COS-7** | RIKEN BRC, RCB0539 |
| **CHO-K1** | JRCB cell bank, JCRB9018 |
| **A-431** | NIHS, JCRB 0004 |
| **Neuro2a** | ATCC, CCL-131 |
| **iPSC derived Neurons** | Elixirgen Scientific, EX-SeV-CW50065 |
| **BS-C-1** | NIHS, JCRB9126 |
| **J774.1** | NIHS, JCRB0018 |

#### 3.1.3. Performance

The error from the focal plane was evaluated using 3 × SD (standard deviation). The verification was conducted in the range of ± 250 μm from the focal plane. Table 2 shows the evaluation results.

Table 2 The evaluation results of the CellFinder.ai

| Objective lens | Error range from the focal plane (± 3 × SD) |
|---|---|
| **Plan Apo λD 4x** | < ± 10 μm |
| **Plan Apo λD 10x** | < ± 8 μm |
| **Plan Apo λD 20x** | < ± 5 μm |

### 3.2. Cell Segmentation using NIS.ai

#### 3.2.1. Principle Overview

The first step in analyzing the images captured by the microscope requires the segmentation of the measurement targets, e.g. the cell nuclei and cell regions. The images are generally binarized by setting a brightness threshold, and post-processing such as morphological transformation is added to segment only the measurement target object. However, this method requires parameters such as the threshold to be fine-tuned depending on the imaging conditions and subtle differences in sample preparation conditions (e.g., staining time, concentration of staining reagent, time since reagent was opened). Complex image processing processes must also be considered to extract the cell nuclei and cell regions from the bright field and phase contrast images.

Meanwhile, segmentation methods using DNNs, such as Pixel2Pixel and U-net, have emerged in recent years and are beginning to be used for cell samples [2]. Our company's NIS-Elements also includes the aforementioned DNN-based segmentation technology in the form of Segmentation.ai and ObjectSegment.ai in NIS.ai. Advantages of this method are that it does not require parameter adjustments by training in advance the differences in samples that occur due to differences in experimental conditions. Moreover, less time is needed for analysis than conventional methods due to the GPU-based calculations. Because the detailed principles and application examples of this method have already been published in Nikon Research Report Vol. 3, they have been excluded from this paper.

#### 3.2.2. Training Method

NIS-Elements SE is equipped with four types of learning models: two training models that segment cell nuclei and cell regions from fluorescent images, and two training models that segment cell nuclei and cell regions from bright field images. A binary image segmented from a fluorescent image using a conventional method as a training image was used to create a segmentation model from a fluorescent image. Initially, a fluorescently stained sample was prepared, bright field and fluorescent images were captured, and the fluorescent image was segmented using a conventional method for creating a training image to create a segmentation model from a bright field image. Similarly, an image in which the cell nucleus was stained with Hoechst33342 (Nacalai Tesque, Kyoto, Japan, 19172-51) was utilized for cell nucleus segmentation, and an image in which the cell region was stained with CellMask™ Deep Red (Thermo Fisher Scientific, Massachusetts, US, C10046) was used for cell region segmentation. The SegmentObject.ai function was used for cell nucleus training, and mainly the Segment.ai function for cell region training. Table 3 lists the cell types used in learning.

Table 3 The list of the cell types used for AI trainning

| Cell type | Origin |
|---|---|
| **HeLa** | RIKEN BRC, RCB0007 |
| **HepG2** | JRCB cell bank, JCRB1054 |
| **COS-7** | RIKEN BRC, RCB0539 |
| **CHO-K1** | JRCB cell bank, JCRB9018 |
| **A-431** | NIHS, JCRB 0004 |
| **J774.1** | NIHS, JCRB0018 |
| **Neuro2a** | ATCC, CCL-131 |

#### 3.2.3. Evaluation Method

The segmentation model created using NIS.ai was subjected to a sensory evaluation and quantitative evaluation by confirming the appearance of the detected region when applied to the image of the trained cell type. Data obtained separately from the training data were used for the evaluation. For the model to detect cell nuclei, the ratio of the number of nuclei detected by the segmentation model to the number of cell nuclei detected from the fluorescent image of Hoechst33342 (Nacalai Tesque) was calculated, and it was confirmed that the ratio was 90–110% (Fig. 3(B)). For the segmentation model to detect cell regions, the ratio of the area of the cell region detected by the segmentation model to the area of the cell region detected from the fluorescent image of CellMask™ Deep Red (Thermo Fisher Scientific) was also confirmed to be in the range of 90–110% (Fig. 3(C)). In addition to conducting accuracy evaluations of the segmentation model, a comprehensive evaluation was carried out to confirm that the difference between the positive and negative controls prepared under the conditions recommended by Nikon for the intended use of the assay was sufficiently detectable. The Z'-factor, which is an index of system stability, was used as an evaluation criterion [1].

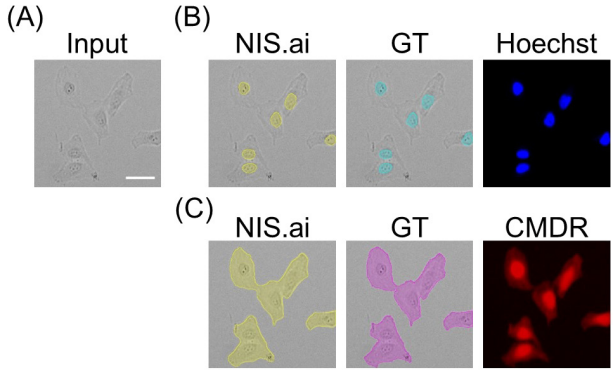


Fig. 3 Region detection by NIS.ai segmentation model
(A) Bright field image input to NIS.ai. Scale bar is 50 μm. (B) From left, nuclear region inference result by NIS.ai (yellow region), ground truth of the nuclear region detected from Hoechst33342 fluorescent image (light blue region), and Hoechst33342 fluorescent image (blue). (C) From left, the cell region inference result by NIS.ai (yellow region), ground truth of cell region detected by CellMask™ Deep Red fluorescent image (magenta region), and CellMask™ Deep Red fluorescent image (red).

## 4 Examples of Assays using Smart Experiment

In this section, we introduce examples of measurements made using Smart Experiment.

### 4.1. Cell Morphology Analysis using Size and Morphological Analysis

#### 4.1.1. Assay Overview

Cells undergo various morphological changes during physiological phenomena. For example, cell enlargement is known to progress with cell aging caused by DNA damage, oxidative stress, and cancer gene activation [3]. Screening drugs that target cascades related to such cell morphological changes and evaluating toxicity to cells using cell morphology as an index are important. The purpose of this assay is to provide an application that can measure the morphological features such as the size, circumference, and circularity of cells and cell nuclei.

In this assay, images are acquired using a 10x objective lens for image analysis, and morphological features are measured by segmenting the cell nucleus region and cell region from the fluorescent images of the cell nucleus and cell region, respectively.

#### 4.1.2. Evaluation Experiment Overview

In the evaluation experiment of this assay, the concentration dependency of cell size was verified using camptothecin (Sigma-Aldrich, Missouri, US), which is an inhibitor of DNA topoisomerase I. HeLa cells were seeded in a 96-well plate (AGC Technoglass, Shizuoka, Japan 5866-096) and cultured. Subsequently, culturing was conducted for 24 hours in a medium containing a dilution series of camptothecin (Sigma-Aldrich) (0–1000 nM, 10 concentration points). Finally, the cells were fixed with 4% PFA, and the cell nuclei were stained with Hoechst 33342 and the cell membranes with CellMask™ Deep Red (Thermo Fisher Scientific) [4].

The sample plate was mounted in the Ji, and a Size and Morphological Analysis assay was conducted. To calculate the Z'-factor, a 0 nM camptothecin (Sigma-Aldrich) range was set as a negative control, and a 333 nM camptothecin (Sigma Aldrich) range was set as a positive control. Six replicate wells were setup for each concentration, and the experiment was conducted thrice as biological replicates.

#### 4.1.3. Evaluation Results

Figure 4 presents the evaluation results.

The representative image examples at each concentration point are shown in Fig. 4(A), the heat map of cell area shown in Fig. 4(B), and the concentration dependence curve shown in Fig. 4(D) confirmed that the cell area increases in a concentration-dependent manner. As shown in Fig. 4(C), the Z'-factor was > 0.5 (0.52), thereby confirming that the assay exhibited sufficient performance. Additionally, the EC50 in this experiment was 12.8 nM.

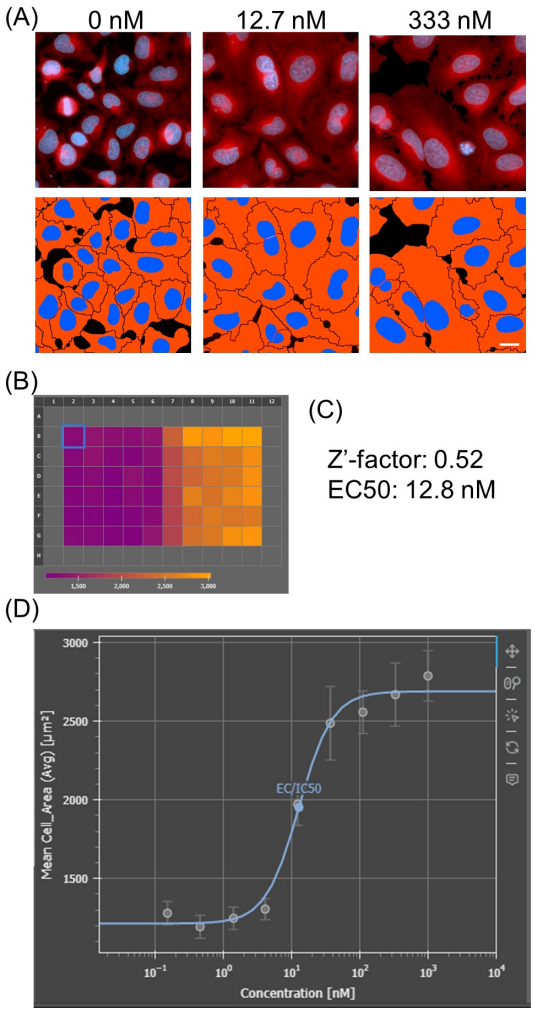


Fig. 4　Size and Morphological Analysis evaluation results
(A) Cell images at concentrations of 0, 12.7, and 333 nM from the left. The top row shows an image of brightness only (blue: Hoechst33342, red: CellMask™ Deep Red), and the bottom row shows the segmented mask (blue: cell nucleus region, red: cell region). The scale bar is 20 µm. (B) Cell area shown in a heat map. (C) Calculation results of Z'-factor and EC50 when cell area is used as index. (D) Concentration dependence curve with cell area on vertical axis and camptothecin concentration on horizontal axis. The error bars indicate standard deviation between replicates. The blue line indicates the fitting of a plot to a sigmoid curve.

## 4.2. Drug Toxicity Evaluation Results using Cytotoxicity

### 4.2.1. Assay Overview

Evaluating cytotoxicity is important for evaluating drugs, culture conditions, environment, and other stresses on cells. The purpose of this assay is to measure the percentage of stained dead cells.

In this assay, images are acquired using a 10x objective lens for image analysis, and the total number of cells and the number of dead cells are determined from the fluorescent images of cell nuclei and dead cells, from which the ratio of the live to dead cells is calculated.

### 4.2.2. Evaluation Experiment Overview

The evaluation experiment of this assay involved the use of a protein kinase inhibitor such as staurosporine (Sigma Aldrich, Missouri, US) to induce cell death and the verification of the concentration dependence of the number of dead cells [5]. HeLa cells were seeded in a 96-well plate (AGC Technoglass) and cultured. Subsequently, culturing was conducted for 24 hours in a medium containing a dilution series of staurosporine (Sigma-Aldrich) (0–1000 nM, 10 steps).

Finally, the cell nuclei were then stained with Hoechst33342 (Nacalai Tesque), whereas the dead cells

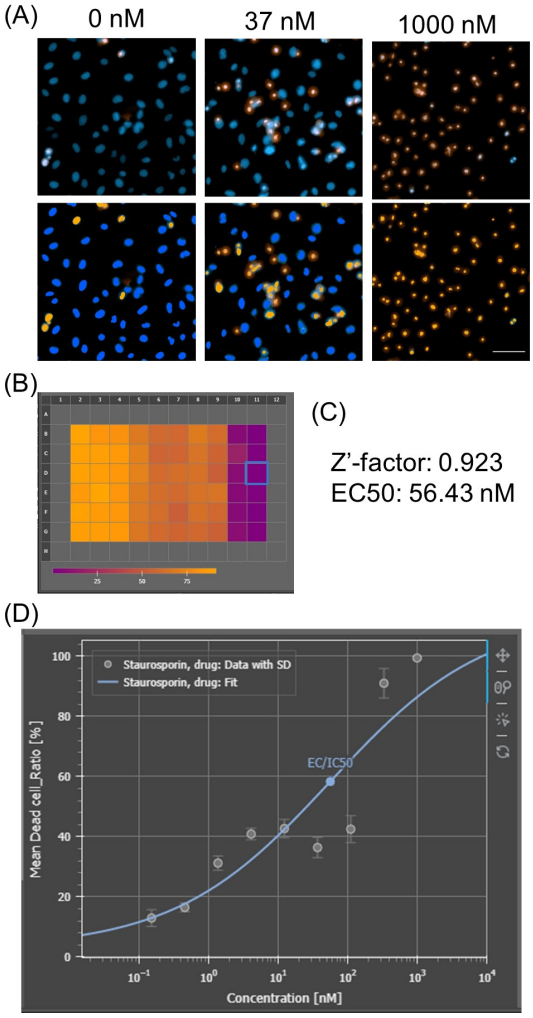


Fig. 5　Cytotoxicity evaluation results
(A) Cell images at concentrations of 0, 37, and 1000 nM from the left. The top row shows an image of brightness only (blue: Hoechst33342, red: EthD-1), and the bottom row shows the segmented mask (blue: live cells, orange: dead cells). The scalebar is 100 µm. (B) Cell death rate shown in a heat map. (C) Calculation results of Z'-factor and EC50 when cell area is used as index. (D) Dose response curve with cell area on the vertical axis and staurosporine (Sigma Aldrich) concentration on the horizontal axis. The error bars indicate standard deviation between replicates. The blue line indicates the fitting of a plot to a sigmoid curve.

were stained with ethidium homodimer-1 (EthD-1) (Thermo Fisher Scientific, Massachusetts, US, L3224).

The sample plate was mounted in the Ji, and a Cytotoxicity assay was conducted. To calculate the Z'-factor, a 0 nM staurosporine (Sigma Aldrich) range was set as a negative control, and a 1000 nM staurosporine (Sigma Aldrich) range was set as a positive control. Six replicate wells were setup for each concentration, and the experiment was conducted thrice as biological replicates.

#### 4.2.3. Evaluation Results

Figure 5 shows the evaluation results.

The representative image examples at each concentration point shown in Fig. 5(A), the heat map of the Dead cell ratio shown in Fig. 5(B), and the dose responce curve shown in Fig. 5(D) confirmed that the cell death rate increased in a concentration-dependent manner. As shown in Fig. 5(C), the Z'-factor was > 0.5 (0.923), thereby confirming that the assay exhibited sufficient performance. Additionally, the EC50 in this experiment was 56.43 nM.

## 5 Conclusion

NIS-Elements SE makes it easy to conduct assays using the newly installed AI functions. In this paper, we introduced the kinds of measurements that are possible using the AI technologies installed in NIS-Elements SE as well as the two assays Size and Morphological Analysis and Cytotoxicity. There are 11 other assay types installed as of the time of writing this paper, and they can be used in many cell-evaluation experiments. We will continue to expand the functions and types of assays with the aim of contributing to the efficiency of the research, particularly in the field of drug discovery and the search for new drugs.

## References

[1] W. Buchser, M. Collins, T. Garyantes, R. Guha, S. Haney, V. Lemmon, Z. Li, and O. J. Trask, "Assay Development Guidelines for Image-Based High Content Screening, High Content Analysis and High Content Imaging," *Assay Guidance Manual*, 2012.

[2] T. Falk, D. Mai, R. Bensch, Ö. Çiçek, A. Abdulkadir, Y. Marrakchi, A. Böhm, J. Deubner, Z. Jäckel, K. Seiwald, A. Dovzhenko, O. Tietz, C. D. Bosco, S. Walsh, D. Saltukoglu, T. L. Tay, M. Prinz, K. Palme, M. Simons, I. Diester, T. Brox, and O. Ronneberger, "U-Net: deep learning for cell counting, detection, and morphometry," *Nature Methods*, vol. 16, pp. 67–70, 2019.

[3] R. Katasho, T. Nagano, T. Iwasaki, and S. Kamada, "Nectin-4 regulates cellular senescence-associated enlargement of cell size," *Scientific Reports*, vol. 13, 21602, 2023.

[4] Y. Futamura, M. Kawatani, S. Kazami, K. Tanaka, M. Muroi, T. Shimizu, K. Tomita, N. Watanabe, and H. Osada, "Morphobase, an encyclopedic cell morphology database, and its use for drug target identification," *Chemistry & Biology*, vol. 19, no. 12, pp. 1620–1630, 2012.

[5] H. -J. Chae, J. -S. Kang, J. -O. Byun, K. -S. Han, D. -U. Kim, S. -M. Oh, H. -M. Kim, S. -W. Chae, H. -R. Kim, "Molecular mechanism of staurosporine-induced apoptosis in osteoblasts," *Pharmacologial Res.*, vol. 42, no. 4, pp. 373–381, 2000.

林　耕磨　Kohma HAYASHI
ヘルスケア事業部 技術統括部 システム開発部
System Development Department
Technology Solutions Sector
Healthcare Business Unit

門井宏平　Kohei KADOI
ヘルスケア事業部 技術統括部 システム開発部
System Development Department
Technology Solutions Sector
Healthcare Business Unit

柴田美智太郎　Michitaro SHIBATA
ヘルスケア事業部 技術統括部 システム開発部
System Development Department
Technology Solutions Sector
Healthcare Business Unit

大井宏美　Hiromi OI
ヘルスケア事業部 技術統括部 システム開発部
System Development Department
Technology Solutions Sector
Healthcare Business Unit

星野哲朗　Tetsuro HOSHINO
先進技術開発本部 数理技術研究所
Mathematical Sciences Research Laboratory
Advanced Technology Research & Development Division


林　耕磨
Kohma HAYASHI


門井宏平
Kohei KADOI


柴田美智太郎
Michitaro SHIBATA


大井宏美
Hiromi OI


星野哲朗
Tetsuro HOSHINO

# デジタル正立顕微鏡を用いた複数免疫染色標本の位置合わせ機能の開発†

森山真樹，佐藤慎哉，渡邉博忠，山浦遼平，森屋健太郎，
古田伸一，苅田　聡，平尾大介，中田千枝子

# Position Alignment Function Development of Multiple Immunostained Specimens using a Digital Imaging Microscope

Masaki MORIYAMA, Shinya SATO, Hirotada WATANABE, Ryohei YAMAURA, Kentaro MORIYA,
Shinichi FURUTA, Satoshi KANDA, Daisuke HIRAO and Chieko NAKADA

病理診断では病変部位から細胞や組織のサンプルを採取し，薄くスライスして染色を施すことで病理標本を得て，病理医が顕微鏡を用いて細胞や組織の形態を観察することで，病気の原因や進行状況を明らかにする．特定のたんぱく質やその他の物質を抗体を用いて特異的に染色する免疫染色では，組織のサンプルを連続に薄くスライスすることで近接した位置の連続標本を得て，各標本 1 枚ずつに 1 種類の染色を施し，総計 3 ～20枚程度の免疫染色標本を観察して診断に供する．さらに各標本で同じ位置を顕微鏡で観察しながら探索して結果を記憶する必要があり，病理医の負担となっている．

デジタル正立顕微鏡では標本全体のデジタル画像を取得可能である．標本全体の画像を用いて標本間の位置ずれを自動検出し，同じ位置を自動探索する位置合わせ機能を開発した．さらに各標本の同一位置における拡大画像をモニターに並べて表示する機能を開発することで，顕微鏡観察時の探索や記憶といった病理医の負担軽減を目指した．

本稿では，複数免疫染色標本の位置合わせ機能に関して，デジタル正立顕微鏡の特徴及びデジタル画像を用いた位置合わせ方法について解説する．

In pathological diagnosis, pathologists routinely examine stained cell or tissue samples, extracted from lesion sites, to identify disease causes and assess progression. This process often involves immunohistochemical staining, where antibodies are used for selectively staining specific proteins or other substances within the samples. However, this approach can be demanding for pathologists as locations must be consistently observed and the results from identical locations should be memorized across multiple specimens.

To mitigate this challenge, we leveraged digital imaging microscope capable of capturing digital images of the entire specimen in a single shot. We developed a function that uses these images to detect any positional shift between the specimens automatically and, subsequently, automatically search for identical locations for alignment. Furthermore, we aimed at alleviating the burden on pathologists during microscopic observation by developing a feature that displays microscopic images of higher magnification from identical positions across different specimens side by side on a monitor.

In this study, we present digital imaging microscopic features and the alignment approach using digital images related to the alignment function for multiple immunostained specimens.

**Key words** 顕微鏡，位置合わせ，自動化，病理切片，デジタルパソロジー
microscope, alignment, automation, pathological specimen, digital pathology

## 1 Introduction

Pathological diagnosis entails cell or tissue sampling from the affected area, which are then thinly sliced and stained to prepare pathological specimens. Pathologists then use a microscope to observe the morphology of the cells or tissue and clarify the cause and progression of the disease. Developments of immunohistochemistry techniques that use antibodies to selectively stain specific proteins and other substances, have enabled a more detailed understanding of various pathological conditions and more precise diagnoses [1]. Immunostaining involves the staining of 3–20 or more

† This article is not intended to advertise any specific medical devices.

different proteins and other substances, which requires the same number of pathological specimens to be prepared. To do so, tissue samples are sliced in succession to obtain consecutive specimens at the same tissue coordinates, and each specimen is stained with a different immunostain for observation. However, the task of observing the same tissue position for each specimen and recording the results from memory imposes a large burden on pathologists.

Nikon has developed a digital upright microscope that does not require an eyepiece and allows the observation to be viewed on a display screen. This digital upright microscope acquires images of the entire specimen in a single shot, and we have developed an alignment function that automatically searches for the same position between different specimens using the acquired images. An additional function has also been developed to display the magnified microscope images of the same position of each specimen side by side on a monitor, with the aim of reducing the burden imposed on pathologists.

In this paper, we explain the alignment function of multiple immunostained specimens using this digital upright microscope, with a focus on the alignment method using digital images.

## 2 Uses and Challenges of Immunostained Specimens

Immunostaining, which selectively stains specific proteins and other substances, has contributed to the development of medical research and diagnosis / treatment. The basic principle of immunostaining is the use of specific bonds formed between antibodies and antigens. Antibodies have a high affinity towards specific antigens, so they can selectively target antigens. Immunostaining is used in many fields owing to its ability to clearly determine the presence and location of specific proteins. Immunostaining has become a particularly indispensable technique in medical applications such as disease diagnosis, treatment effectiveness predictions, and new drug development.

Increasing the number of proteins that can be identified by immunostaining in medical research and pathological diagnosis could lead to the elucidation of new mechanisms and improved diagnostic accuracy. Below, we describe the outline of the process from specimen preparation to evaluation in pathological diagnosis and medical research, as well as the associated issues (underlined parts A–D).

■ Specimen preparation (Fig. 1)

① The sample extracted from the target organ is fixed and embedded in paraffin to prepare a block.

② Slices that are cut to a thickness of about 4 μm are attached to a glass slide (block is cut into thin slices and about 3–20 slices are prepared).

③ The slices are stained on the glass slide (HE staining, immunostaining with Ki67, CD3, etc.).

④ The slices are protected using a cover glass and mounting medium.

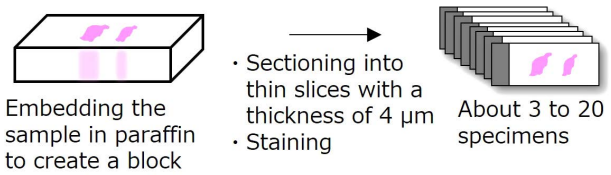


Fig. 1 Sample preparation

■ Specimen observation and evaluation (Fig. 2)

The following process is usually conducted using an upright microscope.

① Observe the HE-stained specimen and determine 3–5 points of interest. At this time, the observer remembers the position and appearance of the points of interest (A).

② The first immunostained specimen is observed. Based on the position and appearance that were memorized in the HE stain, the observer makes observation by looking for the same position (B). The findings (e.g., presence of target proteins) are memorized (C).

③ The second immunostained specimen is observed. Based on the position and appearance that were memorized in the HE stain, the observer makes observation by looking for the same position (B). The findings (e.g., presence of target proteins) are memorized (C).

④ The aforementioned pattern of observations of immunostained specimens is repetitively conducted on up to about 20 specimens, and the results are analyzed. Given the

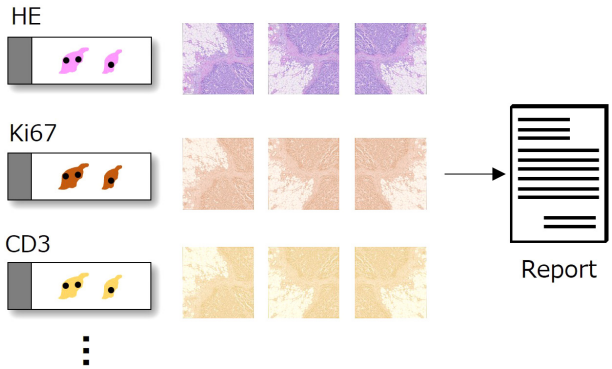


Fig. 2 Observation and evaluation of the specimens with HE staining and immunostaining

difficulty of memorizing all the findings at once, a report could be written for every few specimens, for example. Observers who would like to confirm again can re-observe the specimen (D).

This heavily memory-reliant type of specimen observation and evaluation method is repeated on a daily basis in pathological diagnosis, which imposes a heavy burden on pathologists.

## 3 Alignment Function using Digital Upright Microscope

The specimen is set on the digital upright microscope, and the load button is pressed to take a macro image that gives an overview of the entire specimen. When the specimen is placed at the observation position, the image obtained through the objective lens (micro image) is displayed live on the display, and the macro image is also displayed simultaneously (Fig. 3). The system can memorize the observation position of the macro image, and the micro image at the observation position can be saved.

We devised a method that uses the macro image that is acquired when loading specimens into the digital upright microscope to detect and correct the misalignment of multiple specimens, enabling the exploration and display of the same locations. This method achieves the system workflow shown in Fig. 4. Each step is explained below.


Fig. 3 Display of digital upright microscope
(Center image is micro image (top) and macro image (bottom)

①–②: Acquisition of macro image of first specimen

The observer sets and loads the first specimen into the digital upright microscope. The system acquires a macro image of the first specimen (Fig. 5). Usually, HE stain is

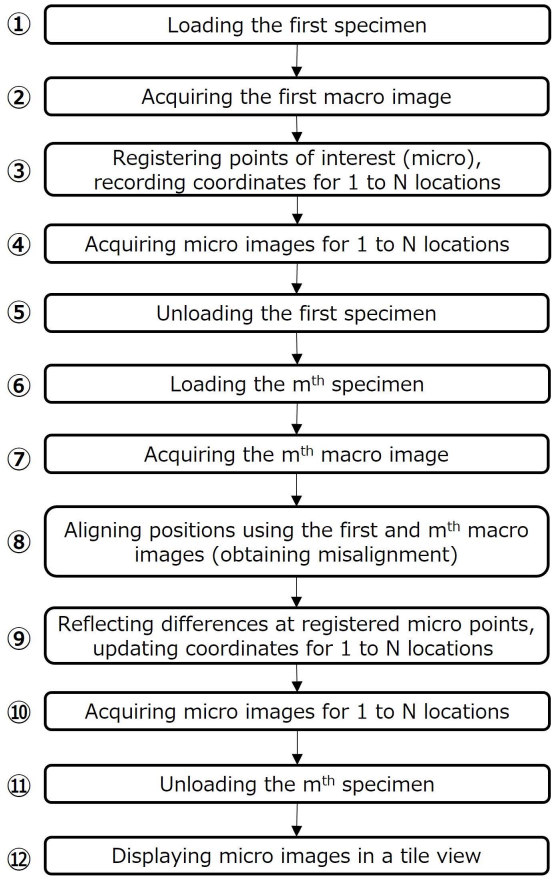


Fig. 4 Alignment function workflow overview

selected for the first specimen to understand the tissue morphology.

③–④: Registration of points of interest of first specimen

The observer visually checks the micro image and registers the points of interest in the first specimen in the system. The system captures and stores the micro images of the registered points (Fig. 5). Multiple points of interest, usually around 3–5 points are often registered (up to a maximum of 12 points can be registered).

⑤: Unloading of first specimen

The observer unloads the first specimen.

⑥–⑦: Acquisition of macro image of $m^{th}$ specimen

The observer sets and loads the $m^{th}$ specimen into the digital upright microscope. The system acquires a macro image of the $m^{th}$ specimen (Fig. 5). Immunostained specimens are often selected for the second and subsequent images. Up to approximately 20 immunostained specimens are prepared in pathological observation.

⑧ Alignment using macro images

The system aligns the first and $m^{th}$ specimens using the

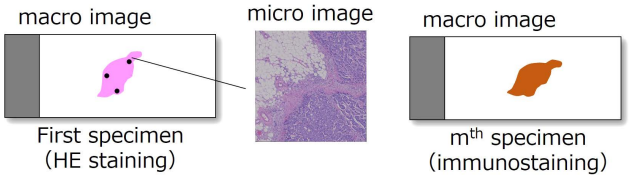


Fig. 5 Macro and micro images

macro images (Fig. 6). The alignment algorithm uses the Scale Invariant Feature Transform (SIFT) [2] to calculate the positional and angular shifts (ΔXY, Δθ) between the macro images. Details on SIFT are presented in Section 4.

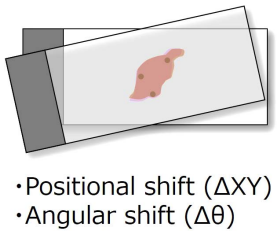


Fig. 6 Detection of extent of misalignment in macro images using SIFT

⑨–⑩: Acquisition of micro image of $m^{th}$ specimen

The system reflects the positional shift ΔXY obtained in step ⑧ to the coordinates of the point of interest in the first specimen in step ③, which allows acquisition and updating of the coordinates of the same point of interest in the $m^{th}$ specimen. The system acquires a micro image at the new coordinates and stores the rotated image that reflects the angular shift Δθ. Steps ⑥–⑩ are repeated for the second to $m^{th}$ specimens to acquire a micro image of the same point of interest in each specimen.

As shown in Fig. 7, the first and $m^{th}$ micro images are in the same position, so their morphology is similar, and the $m^{th}$ micro image is recorded as a rotated image according to the extent of rotational misalignment.

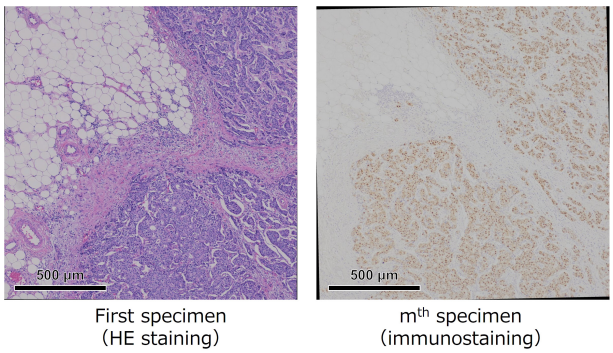


Fig. 7 First and $m^{th}$ micro images

⑪: Unloading of $m^{th}$ specimen

The observer unloads the $m^{th}$ specimen.

⑫: Display of micro images in a tile view

The observer selects up to 10 micro images from all the recorded micro images and displays them in a tile view. The system displays micro images of the same point of interest for each selected specimen in a tile view on the display (Fig. 8).

When any of the images displayed side by side are zoomed in or out or moved laterally in the XY direction by the observer, then all the images move in tandem (Fig. 8). The observer can compare the details of each point while zooming in on the images.

Fig. 8 Display of micro images in a tile view
(Top: standard, bottom: digital zoom)

The above workflow of the alignment function of the digital upright microscope provides solutions to the problems of HE stained and multiple immunostained specimens, as shown in Table 1. Particularly, it is expected to reduce the burden imposed on pathologists in pathological observation.

Table 1 Problems and solutions for HE stained and multiple immunostained specimens

| Problem/ Solution | Content |
|---|---|
| **Problem A** | The observer memorizes the position and appearance. |
| **Solution A** | The system memorizes the position and appearance. |
| **Problem B** | The observer searches for the same position. |
| **Solution B** | The system searches for the same position. |
| **Problem C** | The observer memorizes findings from the observed images. |
| **Solution C** | The system memorizes the images. |
| **Problem D** | The observer re-examines the specimen. |
| **Solution D** | The system displays the images in a tile view. |

## 4 Alignment Function Algorithm and Accuracy Evaluation

SIFT was adopted as the alignment algorithm for the digital upright microscope. SIFT is a feature detection method for image recognition that was published by David G. Lowe in 1999 [2]. The method is widely used for image alignment and object recognition because it has the ability to detect features that are strongly invariant to changes in scale, rotation, viewpoint, and lighting. The algorithm for the alignment function in sample images is described below.

First, feature points of the macro image are extracted. As shown in Fig. 9, the macro image is smoothed and a difference of Gaussian (DoG) image is created, which is the difference between images with the scale (blur intensity) changed. A comparison is made between the pixel value of target and the pixel values of 26 neighboring pixels to identify those pixels with extreme DoG values, including the scale direction. Pixels with extreme DoG values exhibit a remarkable change in contrast and are expected to contain a high volume of information. The above process is used to extract pixels with a high volume of information as candidates for feature points, and top feature points are used for alignment.

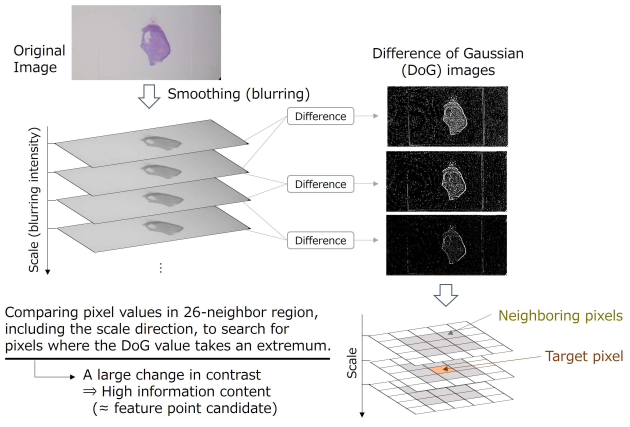


Fig. 9 Extraction of feature points in specimen images using SIFT

Next, the feature values of the feature points are calculated. As shown in Fig. 10, the area around the feature points is divided into 4 × 4 blocks, and the gradient intensity of brightness is calculated in the eight directions for each block. The number of blocks and gradient intensity are used to create a feature value as 128-dimensional gradient intensity information.

Finally, the feature points are matched, and the positional and angular shifts (ΔXY, Δθ) between the two images are calculated. As shown in Fig. 11, the Euclidean distance between one feature value of HE stained specimen and all

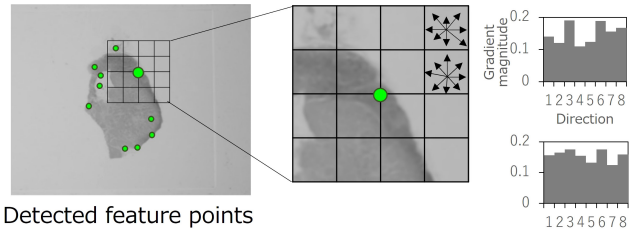


Fig. 10 Calculation of feature values of specimen images using SIFT

feature values of immunostained specimen is calculated. The feature point with the lowest Euclidean distance is determined as the corresponding feature point. The lowest Euclidean distance means that the difference is the lowest in comparison with the aforementioned 128-dimensional gradient intensity.

In cases where there are at least two corresponding feature points, the positional and angular shifts (ΔXY, Δθ) between the two images are obtained by overlaying the images so that these feature points match.

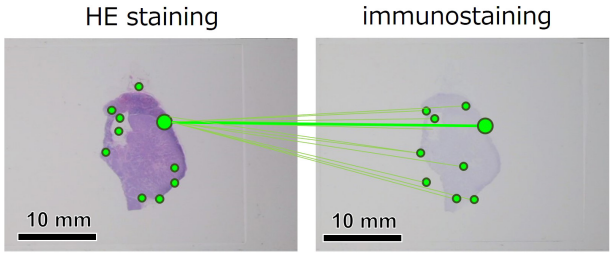


Fig. 11 Matching feature points of specimen images using SIFT

In the alignment algorithm for the digital upright microscope, the parameters for each of the aforementioned steps were optimized using numerous specimens. Evaluation of the accuracy of this alignment function is explained below.

For accuracy evaluation, the images obtained through the 10x objective lens of the digital upright microscope were used. The micro images of the two specimens obtained after alignment were manually superimposed by visual inspection so that the fine structures of the images were completely overlapped. As shown in Fig. 12, the overlapping area (blue diagonal line) was divided by the total area of the micro images (green frame) to determine the accuracy index. This index ranges from 0 to 1, and an index value closer to 1 implies higher alignment accuracy.

A set of 22 specimen pairs was prepared from 44 specimens, and the alignment accuracy of the micro images obtained by the alignment function was evaluated. An alignment accuracy of approximately 0.95 was attained, as shown in the box-and-whisker plot in Fig. 12. It is worth mentioning here that specimens have a wide range of shapes and colors, and we will continue to investigate ways to improve the accu-

racy and robustness so that this method can be utilized for such specimens as well.

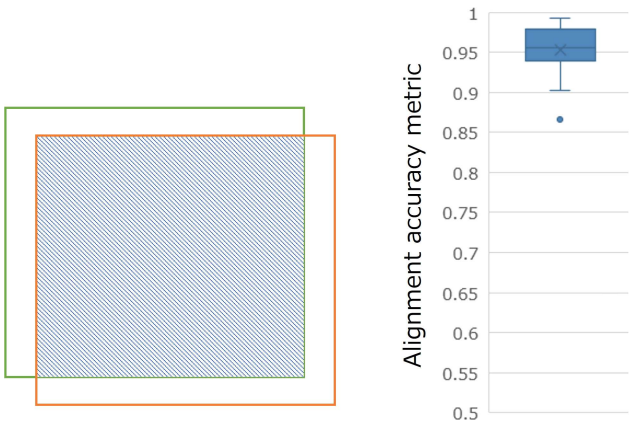


Fig. 12 Alignment accuracy evaluation index (left) and results (right)

## 5 Conclusion

The digital upright microscope can obtain macro images of the entire specimen and enlarged micro images of the point of interest. Through this study, we demonstrated the possibility of accurately and quickly extracting micro images on multiple immunostained specimens at the same site on the tissue of interest to the observer using the alignment function with the macro images. Further, the alignment algorithm has also been explained in detail. The observation support provided by the alignment function is expected to reduce the burden imposed on observers. In future, we will further improve the accuracy and robustness of the alignment function to increase the accuracy of the observations and evaluation of multiple immunostained specimens for smaller lesions for which there is current demand in the field. We expect this study to make a positive contribution to the development of medical research and pathological diagnosis.

## References

[1] M. L. Compton, M. Hogan, and E. S. Reisenbichler, "Differences in immunohistochemistry utilization by general and breast subspecialty pathologists at a large academic institution," *Annals of Diagnostic Pathology*, vol. 42, pp. 92–95, 2019.

[2] D. G. Lowe, "Object recognition from local scale-invariant features," *Proceedings of the Seventh IEEE International Conference on Computer Vision,* vol. 2, pp. 1150–1157, 1999.

森山真樹　Masaki MORIYAMA
ヘルスケア事業部 技術統括部 システム開発部
System Development Department
Technology Solutions Sector
Healthcare Business Unit

佐藤慎哉　Shinya SATO
地方独立行政法人神奈川県立病院機構神奈川県立がんセンター
Kanagawa Cancer Center Research Institute

渡邉博忠　Hirotada WATANABE
ヘルスケア事業部 技術統括部 システム開発部
System Development Department
Technology Solutions Sector
Healthcare Business Unit

山浦遼平　Ryohei YAMAURA
株式会社ニコンシステム
Nikon Systems Inc.

森屋健太郎　Kentaro MORIYA
株式会社ニコンシステム
Nikon Systems Inc.

古田伸一　Shinichi FURUTA
ヘルスケア事業部 技術統括部 設計部
Designing Department
Technology Solutions Sector
Healthcare Business Unit

苅田　聡　Satoshi KANDA
ヘルスケア事業部 技術統括部 システム開発部
System Development Department
Technology Solutions Sector
Healthcare Business Unit

平尾大介　Daisuke HIRAO
ヘルスケア事業部 技術統括部 システム開発部
System Development Department
Technology Solutions Sector
Healthcare Business Unit

中田千枝子　Chieko NAKADA
ヘルスケア事業部 技術統括部 システム開発部
System Development Department
Technology Solutions Sector
Healthcare Business Unit

# 研究開発論文

# Research and Development Reports

# 風車翼型へのリブレット適用による揚力改善効果検証†

柳瀬菜穂，東野嵩也，倉島高広，土橋晋太郎，久保徳嗣，田中元史

# Verification of Lift Improvement by Applying Riblets to Airfoil for Wind Turbines

Naho YANASE, Takaya HIGASHINO, Takahiro KURASHIMA,
Shintaro TSUCHIHASHI, Noritsugu KUBO and Motofumi TANAKA

リブレットは，流体機器の粘性摩擦抵抗を低減する生体模倣技術であり，風車ブレード表面に適用することで要素翼の揚抗比の改善が見込まれ，風力発電効率の向上が期待できる．効率向上の基礎的な評価として，二次元断面の風車翼模型に対してリブレットを加工したフィルムを貼付け，風洞実験にてまずは揚力性能の改善量を評価した．その結果，失速前の広範囲の迎角において，揚力が平均3.4%増加することを実証した．

Riblets are a biomimetic technology that reduces the viscous friction resistance of fluid machinery. By applying riblets to the surface of wind turbine blades, an improvement in the lift-to-drag ratio of the blades is expected that, in turn, can enhance the efficiency of wind power generation. As a fundamental evaluation of the efficiency improvement, a film with riblets was attached to a two-dimensional sectional model of a wind turbine blade, and its lift performance improvement was assessed through wind tunnel experiments. The results demonstrated an average increase of 3.4% in lift across a wide range of angles of attack prior to stall.

**Key words** リブレット，レーザー加工，流体解析，粘性抵抗低減，揚力改善，風力発電，風洞試験
riblet, laser processing, CFD, drag reduction, lift improvement, wind turbines, wind tunnel

## 1 はじめに

現在，地球温暖化の進行に伴い，世界各国で脱炭素社会の実現に向けた再生可能エネルギーの導入が推進されている．日本では“2050年カーボンニュートラルに伴うグリーン成長戦略”が2020年に宣言されており，風力発電は今後成長を期待される分野の一つとされている．このような状況下で，国内の風力発電供給の拡大を維持するためには，風力発電の効率向上が重要な課題となる．

風力発電の効率を向上させる有効な方法の一つに風車ブレードの揚抗比改善がある．揚抗比は，ブレード翼素断面における揚力の向上，および抗力の低減により改善される．風車ブレードをはじめとする流体機器が受ける流体抵抗は，圧力抵抗（慣性抵抗）と摩擦抵抗（粘性抵抗）に大別される．特にレイノルズ数が高い流れ場は壁面境界層が乱流化しやすく，境界層が乱流化した流れ場は層流に比べて壁面において大きな摩擦力を生じる［1］．この壁面摩擦力は抵抗として流体機器のエネルギーを損失させるので，これを低減することは揚抗比の改善につながり，さらには流体機器の効率を向上させることを可能とする．

ところで，速く泳ぐ種のサメにおいては，鱗の一つ一つの表面に 35～100 μm 程度の微小な縦溝が存在することが知られている［2］，［3］．この流れに沿った縦溝構造はリブレット（riblet）と呼ばれ，平滑面に対して 8 ～10%程度の摩擦抵抗の低減をもたらすことが実験的に明らかにされている［4］．

リブレット構造によって摩擦抵抗が低減することは，物体表面に形成される境界層内の速度分布が変化していることを意味する．翼素において境界層速度分布が変化すると摩擦抵抗だけでなく，圧力抵抗および揚力も変化する可能性がある．

しかしながら，実際の流体機器の表面に対してリブレットを適用した例は少ない．リブレットは，そのサイズと形状を流体機器の表面の流れ場に合わせて成形する必要があり，これが実用化の難易度を高くしている．株式会社ニコンでは，自社のコア技術である光・精密技術を発展させ，

† 本稿は，著者の引用文献［5］の日本風力エネルギー学会より転載の許諾を得ている．

レーザー加工による任意形状のリブレットを適用する技術を開発した．Fig. 1 にレーザー加工したリブレットの SEM 画像を示す．

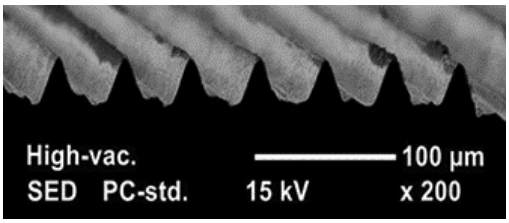


Fig. 1　リブレット加工表面 SEM 画像

現在，我々は様々な流体機器へのリブレット適用の可能性を見出し，その一つとして風車へのリブレット適用に関する研究を進めている．

リブレット適用の困難さから国内における中・大型風車へのリブレット適用の事例は未だなく，それら風車ブレードでの実用化においてはリブレット効果の定量的評価がまず課題として挙げられる．そこで我々は，代表的な風車翼型の二次元翼模型に対して，風洞実験を行い，リブレット適用による翼素の性能特性変化を評価した．本報告では，その中でも特に揚力性能の変化に関する結果を紹介する．

## 2 実験セットアップ

### 2.1. 実験装置

風洞実験は，産業技術総合研究所が所有するつくば北風洞にて実施した．本風洞は試験部流路断面 1.4 m×1.4 m を有する回流式風洞である．最大風速は 48 m/s，乱れ度は風速 10 m/s 以上において0.5%以下である．

実験対象として用いた翼型は，将来フィールド実証試験に使用予定の SUBARU 15/40（定格出力 40 kW）のブレードにおける代表翼型 MEL18M31を用いた．供試翼は，コード長 0.3 m，スパン長 1.4 m のものを使用し，風洞流路中央に上下壁の端から端までを渡すように配置した．翼はピッチ軸をモーターつなぎ，迎角を任意に変化させた．迎角は絶対式ロータリーエンコーダーを用いて測定した．また翼表面にはコード方向に直径 0.5 mm の静圧孔を開け，電子式多点圧力スキャナーを用いて表面圧力分布の測定を行った．Fig. 2 に本風洞のテストセクションの外観写真を示す．

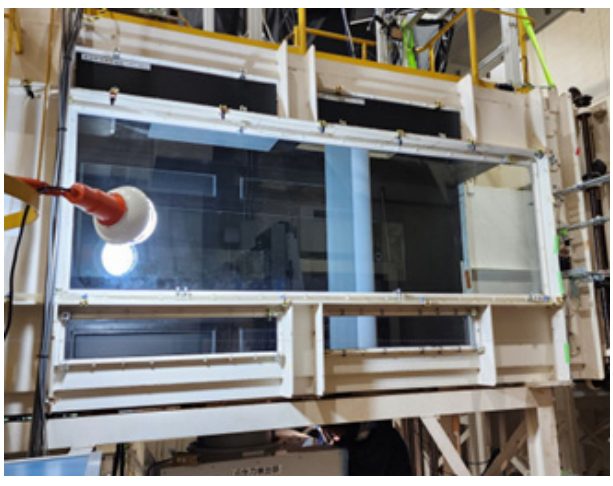

Fig. 2　つくば北風洞　写真

### 2.2. 実験方法

本研究では，５種類の実験条件による揚力特性を比較することで，リブレット効果の定量評価を行った．実験条件ごとにフィルムを用意し，それぞれを同一の翼型に貼り付けて風洞試験を実施し，翼表面の静圧分布を取得した．静圧分布の取得中，翼型は流れの中で静止状態におき，圧力測定が終了する都度，次の迎角姿勢に変化させた．取得した翼面静圧分布をコード方向に積分することで揚力を算出し，同時に取得した流入気流の情報を用いて揚力係数に無次元化して比較した．

リブレット設計にあたり，まず，対象風車ブレードについて MEL18M31翼型を持つ翼素断面において，設計点である迎角 7 deg で二次元翼の流体解析を行った．その結果をもとに最適なリブレット形状を算出した．設計形状をレーザー加工によりフィルム上に成形し，表面がリブレット成形されたフィルムを翼面に貼り付けた．フィルムには，風車エロージョン保護シートとして実績のある3M 社製のポリウレタンフィルムを使用した．

### 2.3. 実験条件

風洞実験は風速 u＝40 m/s，レイノルズ数 Re＝800,000，迎角 AoA＝－6～27 deg で行った．リブレット貼付条件は Table 1 に示す通りである．流体条件は対象風車の通常の運転条件に相当する．以下に実験条件の一覧を示す．

① Reference
　フィルム貼付なし
② Smooth-Full
　未加工フィルムを翼模型全体に巻き付けるように貼付
③ Riblet-Full
　部分的にリブレット加工が施されたフィルムを全体に巻き付けるように貼付

Table 1　実験条件

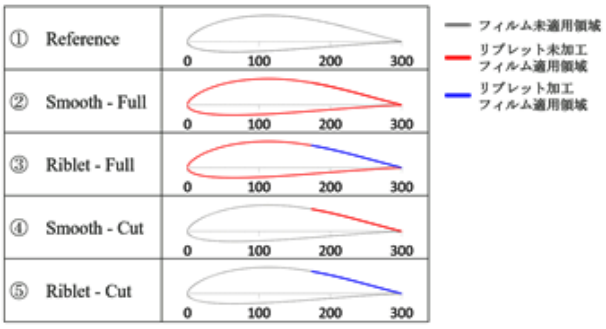

④ Smooth-Cut
未加工フィルムを翼後縁側にのみ貼付
⑤ Riblet-Cut
リブレット加工フィルムを翼後縁側にのみ貼付

## 3 結果および考察

### 3.1. リブレットによる揚力の変化

まずは純粋なリブレット効果を評価するために条件① Reference，条件② Smooth-Full および条件③ Riblet-Full を比較する．

Fig. 3 に揚力係数と迎角の関係を，Fig. 4 に Reference 条件に対する他 2 条件の揚力係数の増加割合 $K_{cl}$ を示す．

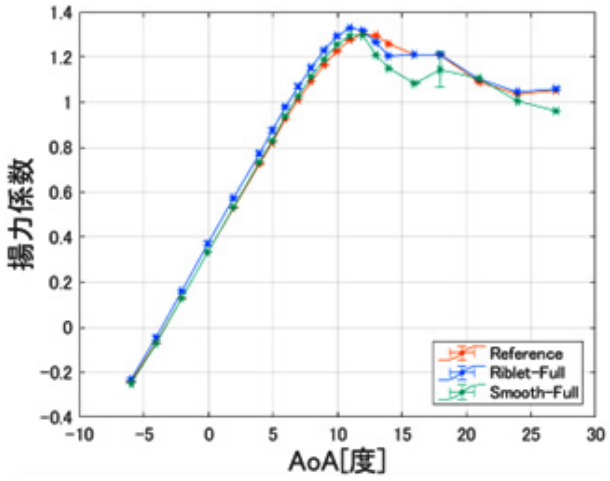


Fig. 3　リブレットが揚力係数に与える影響

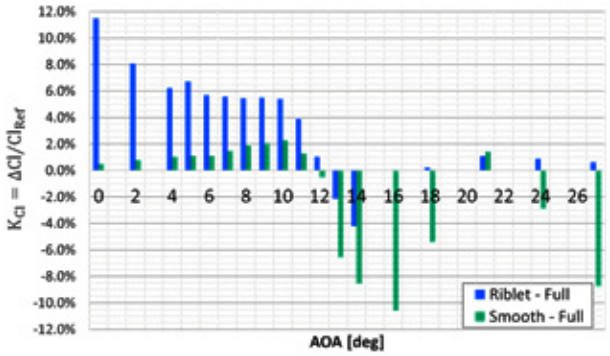


Fig. 4　リブレットが揚力係数の増加割合に与える影響

Fig. 3 より，最大揚力を示す迎角よりも浅い迎角となる，0 ≤ AoA ≤10 deg の範囲において，Riblet-Full は他のリブレットなし条件に比べ高い揚力係数を示す．その増加割合は Fig. 4 に示す通りであり，Reference に対し Riblet-Full は平均6.7%であった．一方 Reference と Smooth-Full を比べると，同様に揚力係数は増加するものの，Fig. 4 よりその増加割合は1.4%であり，リブレットが翼素の揚力を増加させる効果を持つことは明らかである．

リブレットによる揚力増加の要因を特定するには今後さらなる研究が必要であるが，現時点で考えうる要因の一つとして翼後縁側における境界層の整流が挙げられる．リブレットにより整流され，境界層の運動量損失が抑えられると，翼型後縁部での運動量が回復する．これが流れ方向を正とする右手系でみたときの時計回りの翼の循環を増加させ，揚力の増加につながったと考えられる．実際，翼の循環増加は本実験結果における翼面圧力分布にも現れている．Fig. 5 に迎角 7 deg における翼面圧力係数（Cp）分布を示す．

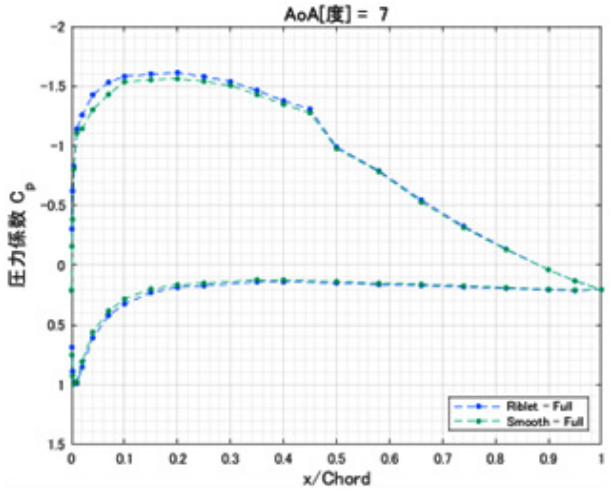


Fig. 5　迎角 7 deg の Cp 分布
※リブレット加工領域：約0.5<x/Chord

Fig. 5 にて，Smooth-Full と Riblet-Full を比較すると，0 ≤ x/Chord ≤ 0.5の領域で，圧力が負圧面において低下し，一方で正圧面においては上昇する．この結果はリブレットにより Fig. 5 において時計回りの翼の循環が増加したことを示している．

### 3.2. Riblet-Cut フィルムよる揚力の変化

次に既存の実機風車にリブレットフィルムを貼り付けることを想定して，良好な施工性を備える小面積なフィルムの実験条件⑤ Riblet-Cut の揚力性能変化を評価する．

Fig. 6 に Reference と Riblet-Cut の揚力係数と迎角の関係を，Fig. 7 に Reference に対する Riblet-Cut フィルムの揚力係数の増加割合 $K_{cl}$ を示す．

Fig. 7 より Reference に Riblet-Cut を適用することで，設計点の迎角 7 deg において揚力係数は2.9%増加し，さらに最大揚力付近よりも浅い迎角 0 deg ≤ AoA ≤10 deg の範囲において平均4.5%の揚力係数の増加が示された．従って，Riblet-Cut を貼付けた場合でも，設計点である 7 deg だけではなく，最大揚力よりも浅い広範囲の迎角において揚力増加を得られ，リブレットは迎角に対してロバストな効果を示すと言える．

一方で，最大揚力の迎角（12 deg）では揚力係数の減少がみられた．その程度は Fig. 7 に示す通り2.8%であった．これは，Riblet-Cut による揚力係数の変化が単純なリブレット

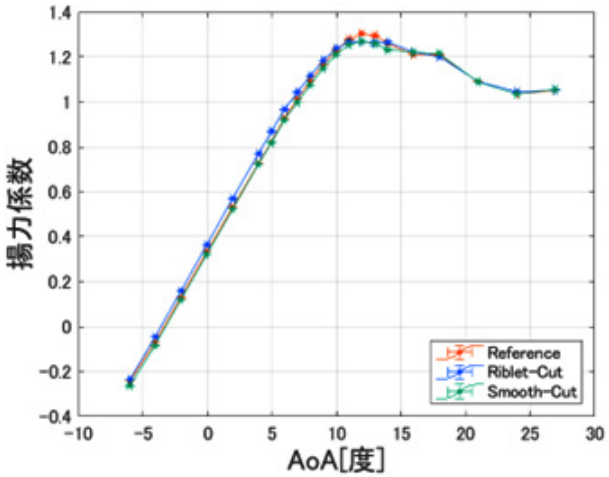


Fig. 6　小面積カットフィルムが揚力係数に与える影響

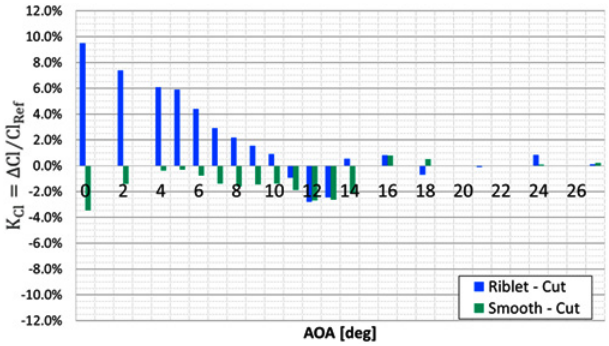


Fig. 7　小面積カットフィルムが揚力係数の増加割合に与える影響

による効果だけではないことが要因と考えられる．次節ではこの要因がRiblet-Cutフィルム端部の段差にあると考え，端部段差が揚力係数に与える影響を評価した．

### 3.3. フィルム端部の段差が与える影響

Riblet-Cutフィルムの端部は翼素コード方向の中央付近に位置するため，この端部の段差が流れを乱し，翼素の性能が低下する可能性がある．この影響を評価するため，条件①Referenceと条件④Smooth-Cutフィルムの揚力係数を比較した．Fig. 6に両者に関する揚力係数と迎角の関係を示す．Fig. 7に揚力係数の増加割合 $K_{cl}$ を示す．

Fig. 6より，Referenceに対しSmooth-Cutフィルムを適用することで揚力係数の減少が迎角11≤ AoA ≤14degの範囲でみられた．特に迎角6度を境に揚力係数の勾配が変化し，最大揚力となる迎角で最も大きな差が見られた．Fig. 6に示す通り，段差の影響はリブレットの効果を低下させ，最大揚力となる迎角（12 deg）で揚力係数は2.7%低下した．この結果は，Fig. 7に示した最大揚力付近におけるReferenceに対するRiblet-Cutの揚力係数の減少と定量的にも一致する．従って，3.2節で評価されたRiblet-Cutの最大揚力付近での揚力係数減少はフィルム端部の段差によることが分かった．

## 4　まとめ

本研究は，風車ブレードにおけるリブレットの実用化に向け，リブレット成形されたフィルムの揚力係数へ効果を二次元翼の風洞試験により定量的に評価した．その結果，以下に示す3つの結論を得た．

Ⅰ．リブレットによる純粋な効果として，迎角最大揚力よりも浅い迎角範囲で平均6.7%の揚力係数増加が示された．

Ⅱ．実用化に向け有力なRiblet-Cutフィルムにおいても，設計点の迎角7 degだけではなく，広範囲の迎角で平均4.5%の揚力係数増加を得て，迎角に対するロバストな効果が示された．

Ⅲ．フィルム端部に段差がある場合，その影響はリブレットの効果を減じ，最大揚力付近の迎角で顕著に表れることが示唆された．

今後は，本実験結果から抗力を算出し，揚抗比の観点からリブレットがブレード空力性能へ与える影響を評価する．また，この評価結果をもとに風車ブレードへのリブレットフィルム適用によるAnnual Energy Production（AEP）改善量を見積る計画である．

### 謝　辞

本成果の一部は，福島県における再生可能エネルギーの導入促進のための支援事業費補助金（福島再生可能エネルギー研究所最先端研究・拠点化支援事業）「風力発電の維持管理等の技術開発・人材育成拠点の形成」における技術研修を活用して得られた．

## 引　用　文　献

［1］三宅裕，“壁乱流の渦，”*ながれ*，vol. 22, no. 1, pp. 29–34, 2003.

［2］鈴木雄二，笠木伸英，“壁面乱流の知的能動制御，”*セーブメーション・レビュー マイクロフローセンサ特集号*, pp. 50–57, 2001.

［3］D. W. Bechert, G. Hoppe, and W.-E. Reif, “On the drag reduction of shark skin,” in *Proc. 23rd Aerospace Sciences Meeting*, 1985, doi: 10.2514/6.1985-546.

［4］D. W. Bechert, M. Bartenwerfer, G. Hoppe, and W.-E. Reif, “Drag reduction mechanisms derived from shark skin,” in *Proc. 15th Congr. ICAS*, pp. 1044–1068, Sep. 1986.

［5］柳瀬菜穂，東野嵩也，倉島高広，土橋晋太郎，久保徳嗣，田中元史，“風車翼型へのリブレット適用による揚力改善効果検証，”*第45回風力エネルギー利用シンポジウム*, pp. 376–379, 2023.

柳瀬菜穂　Naho YANASE
次世代プロジェクト本部 第二開発部
2nd Development Department
Next Generation Project Division

東野嵩也　Takaya HIGASHINO
次世代プロジェクト本部 第一開発部
1st Development Department
Next Generation Project Division

倉島高広　Takahiro KURASHIMA
先進技術開発本部
Advanced Technology Research & Development Division

土橋晋太郎　Shintaro TSUCHIHASHI
次世代プロジェクト本部 第一開発部
1st Development Department
Next Generation Project Division

久保徳嗣　Noritsugu KUBO
国立研究開発法人 産業技術総合研究所
National Institute of Advanced Industrial Science and Technology

田中元史　Motofumi TANAKA
国立研究開発法人 産業技術総合研究所
National Institute of Advanced Industrial Science and Technology


柳瀬菜穂
Naho YANASE


東野嵩也
Takaya HIGASHINO


倉島高広
Takahiro KURASHIMA


土橋晋太郎
Shintaro TSUCHIHASHI


久保徳嗣
Noritsugu KUBO


田中元史
Motofumi TANAKA

# 宇宙空間光通信用 連続波単一横モード偏波保持 10 W Er/Yb 共添加ファイバー増幅器の開発

小林啓紀，狩野良子，瀬尾崇志，鈴木康史，水田栄一，橋本洋輔，荒木智宏，高田康利

# Development of a Continuous Wave Single Transverse Mode Polarization-Maintaining 10 W Er/Yb-Codoped Fiber Amplifier for Space Communications†

Hiroki KOBAYASHI, Ryoko KANO, Takashi SEO, Yasushi SUZUKI, Eiichi MIZUTA, Yosuke HASHIMOTO, Tomohiro ARAKI and Yasutoshi TAKADA

宇宙空間でのデータ通信量の増加に伴い，宇宙空間光通信への注目が高まっている．ニコンと JAXA は，大容量宇宙光ネットワーク開発の一環として，変調連続波信号用の単一横モード動作，10 W 偏波保持 Er/Yb 共添加ファイバー (EYDF) 増幅器の開発を進めてきた．現在，エンジニアリングモデル（EM）の開発を完了し，2024年に国際宇宙ステーションにて，光通信実証実験を行う予定である．

光増幅器は，耐放射線性 EYDF を用いた 3 段の後方励起構成からなる．励起用レーザーダイオードと寄生発振防止のためのモニター用フォトダイオードを備え，いずれも十分な放射線耐性を確認した．また，制御基板も含んでいる．外形寸法は，300 mm× 380 mm× 76 mm，重さは 6.3 kg であった．

室温大気圧下，−3 dBm の信号光入力時に，合計 34 W 励起で 10 W の光出力を得，ウォールプラグ効率10.1% を達成した．また，室温大気圧下で，出力光量 10 W，2000時間の動作を達成した．

宇宙用コンポーネントとしての信頼性を確保するため，振動試験と熱真空試験を実施した．動作温度範囲の上下端，± 0℃と +50℃で，出力光量 10 W，偏光消光比（PER）16 dB 以上を達成し，性能劣化は認められなかった．

Space optical communications have attracted growing attention as space data traffic volumes continue to increase, and as part of ongoing efforts to develop high-speed optical space networks, Nikon and JAXA have been developing a single-transverse-mode 10 W polarization-maintaining Er/Yb-codoped fiber (EYDF) amplifier for modulated continuous-wave signals. We have finished developing the engineering model (EM) and plan to demonstrate this amplifier as a part of optical communication system on the International Space Station in 2024.

The EM amplifier has a three-stage backward pumping structure with radiation-hardened EYDF. It also includes pump laser diodes, and power monitoring photodiodes to avoid parasitic lasing, both of which have been confirmed to have adequate radiation tolerance, as well as a control driver circuits. The overall dimensions are 300 mm × 380 mm × 76 mm, and it weighs 6.3 kg.

The EM amplifier achieved optical output power of 10 W at pumping power of 34 W in total under standard temperature and pressure conditions (STP: room temperature, 1 atm) with a −3 dBm signal input. The total wall-plug efficiency reached 10.1%. The amplifier achieved an operating time of 2000 hours at 10 W under STP.

We conducted a mechanical vibration test and an operating thermal vacuum test to ensure the reliability of the amplifier as a space component. At the upper and lower end of the operation temperature range, ± 0 and +50°C, the output power and polarization extinction ratio (PER) were > 10 W and > 16 dB, respectively, without any degradation of the amplification gain or PER.

**Key words** 自由空間光通信，高出力光ファイバー増幅器，宇宙運用，真空，放射線耐性
free space optical communications, high power fiber amplifiers, space operations, vacuum, radiation tolerance

## 1 Introduction

The volume of data traffic in space communications continues to increase. However, the channel capacity of conventional radio waves is reaching to its limit, and the carrier frequency has been extended to millimeter-wave band.

Free-space optical communications have attracted attention in recent years as a means of exceeding this limitation

† This paper is reprinted with permission from SPIE, the international society for optics and photonics [6].

by increasing the carrier frequency dramatically. In 1994, the Communications Research Laboratory (CRL, now the National Institute of Information and Communications Technology, NICT) in Japan achieved the first ground-to-space optical communication using the Laser Communication Equipment (LCE) on ETS-VI [1], which was developed and launched by the National Space Development Agency (NASDA, now part of JAXA). Following that, the European Space Agency (ESA) achieved the first space-to-space optical communication between SPOT-4 and ARTEMIS in 2001 [2]. JAXA and ESA also achieved the first space-to-space bi-directional optical communication link between OICETS and ARTEMIS in 2005 [3].

Since these demonstrations were in the early days of free-space optical communications, the signals were transmitted by 0.8 μm laser diodes (LDs) using the intensity modulation-direct detection (IM-DD) method [4]. The data transfer rate limitation can be increased by applying advanced modulation methods, such as phase-shift keying, compared with IM-DD.

Today, data transfer rates on the ground have exceeded 100 Gbit/(s·fiber). Our goal is for the space-based backbone network to communicate as rapidly as ground-based optical communications, and the optical high-power amplifier (OHPA) is one of the key components.

JAXA is developing an optical data relay system named "LUCAS," which stands for the Laser Utilizing Communication System [5]. To promote faster communication with smaller size, weight, and power (SWaP) optical communication terminals in the near future, compared with the present LUCAS, we began to develop a 10 W OHPA and to install and evaluate it on the International Space Station (ISS). In this article, we provide details of the developed engineering model (EM), which was used to evaluate the environmental tolerances required in order to advance to the proto-flight model (PFM) to be launched.

## 2 Amplifier Design

To achieve the aims described above, we designed the amplifier as follows.

### 2.1. Target Specification

We set the target specifications as shown in Table 1, with reference to the overall system requirements and the ISS Japanese Experiment Module (JEM) interface specifications.

### 2.2. System Structure

The amplifier contains the optical fiber amplifiers and the electrical control driver board in a single package (Fig. 1). The PDs monitor the optical power and protect the amplifier by detecting anomalies such as parasitic lasing.

### 2.3. Amplifier Optical Structure

The amplifier has three stages of Er/Yb-codoped fibers (EYDFs) (Fig. 2). All of these stages have backward pumping configurations. The passive optical components, the LDs, and the photodiodes (PDs) are commercial off-the-shelf (COTS) products. The radiation tolerances of the EYDFs were confirmed by the manufacturer. The booster LDs (#2 & #3) are driven together by one control driver.

Table 1 Target specifications for evaluation on the ISS and actual measured values of the OHPA

| Item | | Unit | Target specification | Achieved value |
|---|---|---|---|---|
| Input optical power level | | dBm | −3.0 to +3.0 | |
| Output optical power level | | dBm | > +40.0 | > +40.0 |
| Optical power gain | | dB | 37 to 43 | |
| Signal wavelength | | nm | 1560.606 | |
| Signal modulation | | — | RZ-DPSK | |
| Modulation rate | | GHz | > 2.5 | |
| Polarization extinction ratio (PER) | | dB | > 15 | > 16 |
| Return light at 10 W operation | | dBm | < −39 | < −45 |
| Total power consumption (EOL at 25°C, see §5) | | W | < 151 | 103 |
| Wall-plug efficiency (EOL at 25°C, see §5) | | — | > 8% | 9.7% |
| Storage temperature | | °C | −40 to +70 | |
| Operating temperature | | °C | ± 0 to +50 | |
| Dimensions (Protrusions not included) | Width | mm | < 360 | 300 |
| | Depth | mm | < 300 | 300 |
| | Height | mm | < 100 | 76 |
| Weight | | kg | < 7.0 | 6.3 |
| Operating period | | year | > 3 | |
| Operating duty | | — | 5% | |

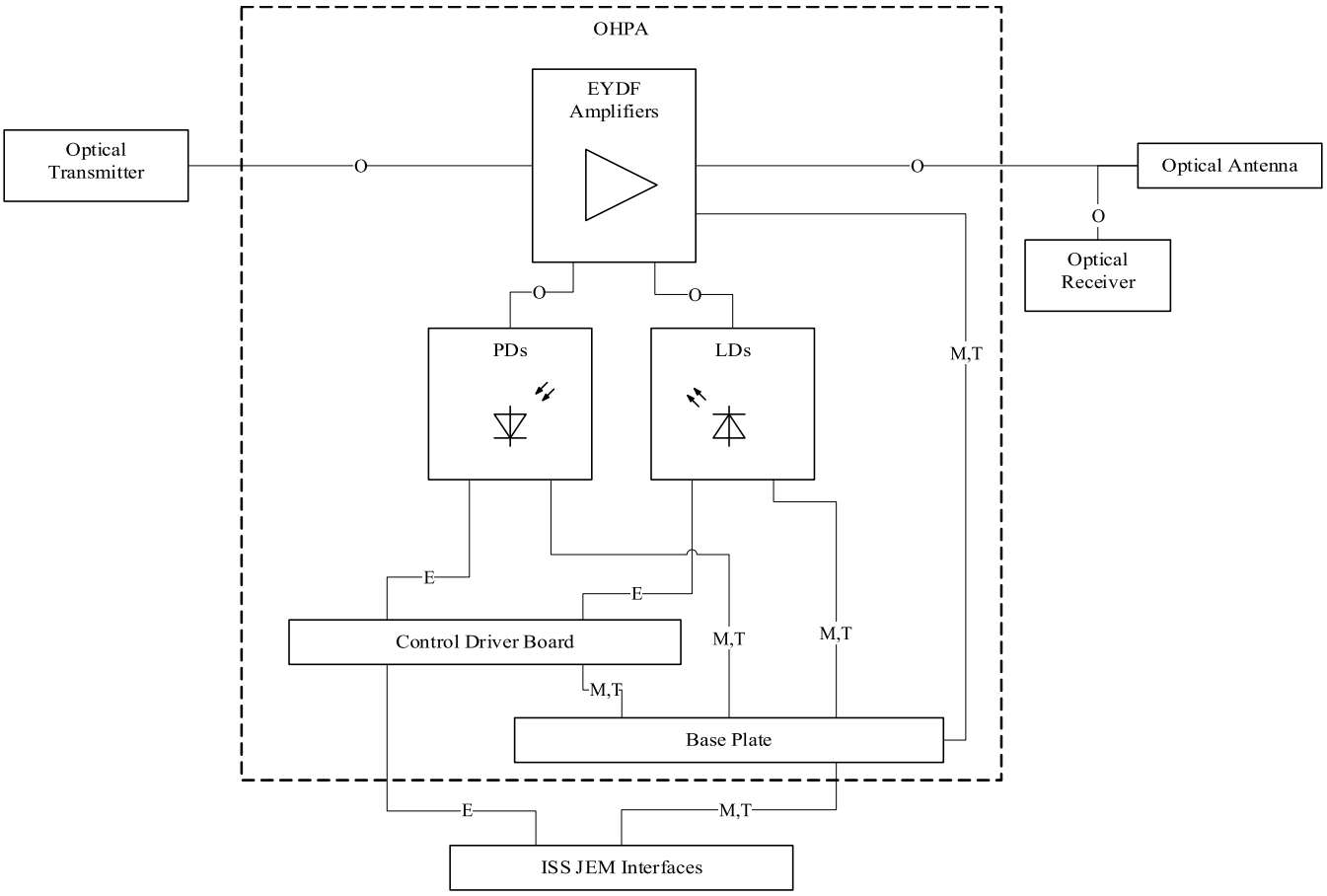


Fig. 1 System block diagram of the optical transceiver: the letter symbols on the connecting lines represents, the electrical (E), mechanical (M), optical (O), and thermal (T) interfaces.

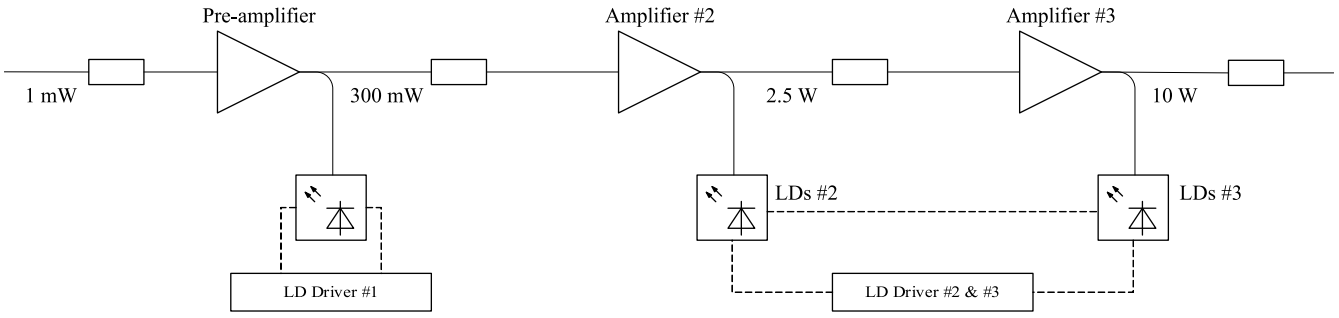


Fig. 2 Optical block diagram

### 2.4. Mechanical and Electrical Design

The total dimensions of the amplifier are 300 mm × 380 mm × 76 mm, and its appearance is shown in Fig. 3. The amplifier weighs 6.3 kg, including the control driver board and the electrical components. It has one optical connector for the input signals, one optical output pigtail, and 3 electrical connectors for a DC 28 V power supply and telemetry & command communications.

Fig. 3 Appearance of the amplifier

## 3 Radiation Tolerance of Semiconductor Components

### 3.1. Radiation Dose Condition

To ensure radiation tolerance, experiments were conducted in which radiation was applied to the semiconductor electro-optical (e-o) components.

Table 2 describes the radiation dose conditions for the ISS experiment, assuming 1 year of operation on the ISS with a 50% margin. Table 3 describes more severe conditions, which anticipate future changes in operating conditions, such as 10 years of operation in geostationary orbit (GEO).

The tests confirmed that the changes in the characteristics were sufficiently small for the target operating period of the amplifier (see §5).

### 3.2. LDs Exposed to Gamma Ray Radiation

Four samples of the same LD products were irradiated with gamma rays. The results in Fig. 4 shows output power degradations of < 2.8% and < 4.7% at exposures of 30 Gy and 1000 Gy, respectively.

### 3.3. LDs Exposed to Proton Radiation

Four samples of the same LD products were irradiated with protons. The results in Fig. 5 show output power degradations of < 0.8% and < 1.4% at exposures of $1.5 \times 10^9$ $p^+/cm^2$ and $1.0 \times 10^{11}$ $p^+/cm^2$, respectively.

### 3.4. PDs Exposed to Gamma Ray Radiation

The measurement was conducted at the same time as the experiment described in §3.2. Four samples of the same PD products were irradiated with gamma rays. The results in Fig. 6 show e-o conversion efficiency decreases of < 1.3% and < 1.3% at exposures of 30 Gy and 1000 Gy, respectively.

### 3.5. PDs Exposed to Proton Radiation

Four of the same PD products were irradiated with protons at the same time as the experiment described in §3.3. The results in Fig. 7 show the e-o conversion efficiency decrease of almost 0% and < 4.9% at exposures of $1.5 \times 10^9$ $p^+/cm^2$ and $1.0 \times 10^{11}$ $p^+/cm^2$, respectively.

## 4 Test Results for the OHPA

### 4.1. Optical Output Power under STP

The amplifier emitted output power of 10 W with a −3 dBm input and a total booster pumping power of 31.5 W under standard temperature and pressure (STP: room temperature, 1 atm) (Fig. 8). The input signal was a 1.5 μm continuous-wave (CW), and the linewidth was ~5 GHz. The pumping power for the preamplifier was fixed to 2.3 W. The total power pumping of the LDs was 33.7 W, which means the total (from the preamplifier to the booster amplifiers) optical-optical (o-o) conversion efficiency was 29.7%.

Table 2 Radiation dose conditions for the ISS experiment

| Type | Energy | Flux | Fluence |
|---|---|---|---|
| Protons ($p^+$) | 70 MeV | $1.0 \times 10^7$ $p^+/(cm^2 \cdot s)$ | $1.5 \times 10^9$ $p^+/cm^2$ |
| Gamma rays ($^{60}Co$) | 1.17 & 1.33 MeV | 62 Gy/h | 30 Gy |

Table 3 Radiation dose conditions for future plans with more severe conditions

| Type | Energy | Flux | Fluence |
|---|---|---|---|
| Protons ($p^+$) | 70 MeV | $1.0 \times 10^8$ $p^+/(cm^2 \cdot s)$ | $1.0 \times 10^{11}$ $p^+/cm^2$ |
| Gamma rays ($^{60}Co$) | 1.17 & 1.33 MeV | 225 Gy/h | 1000 Gy |

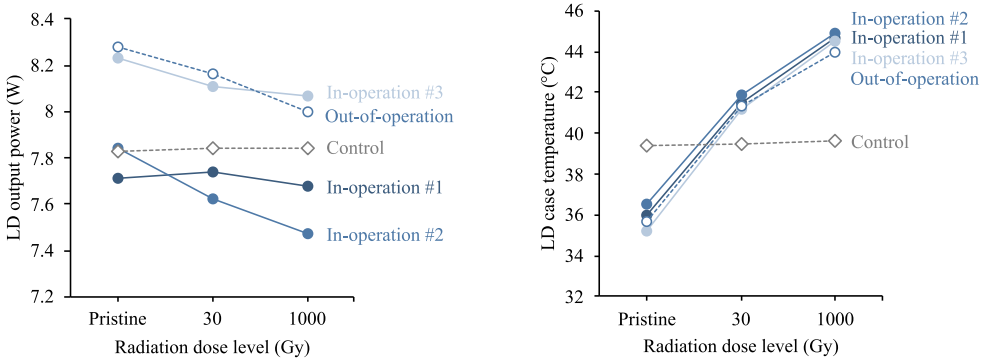


Fig. 4 Output power at 9.0 A operation versus radiation dose (left) and LD case temperature versus radiation dose (right): three in-operation samples (filled blue circles), one out-of-operation sample (open blue circle), and one non-irradiated control sample (open gray diamond)

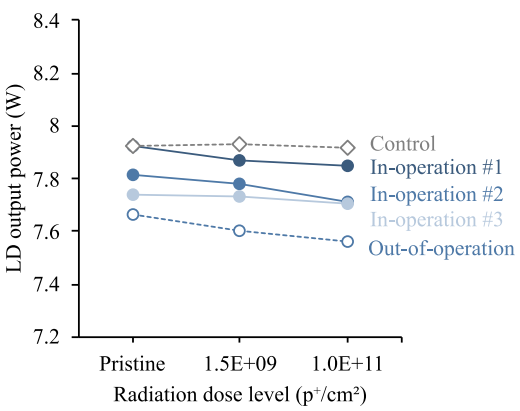


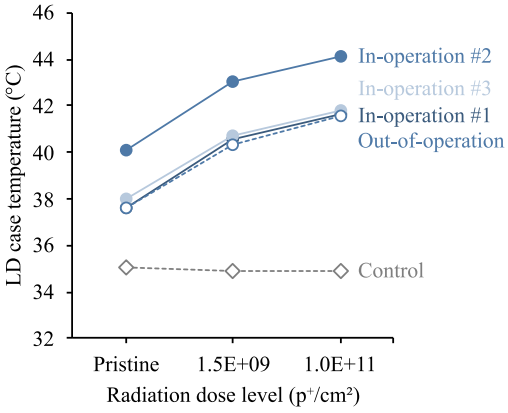


Fig. 5 Output power at 9.0 A operation versus radiation dose (left) and LD case temperature versus radiation dose (right): three in-operation samples (filled blue circles), one out-of-operation sample (open blue circle), and one non-irradiated control sample (open gray diamond)

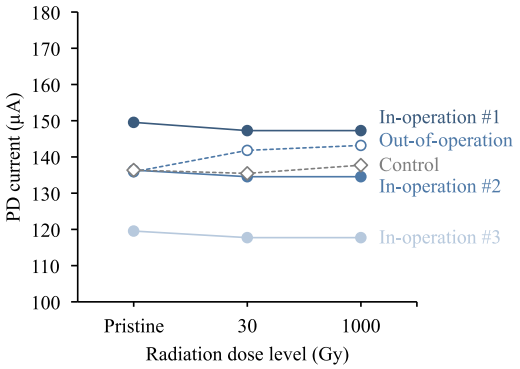


Fig. 6 Output power at 150 μW input versus radiation dose: three in-operation samples (filled blue circles), one out-of-operation sample (open blue circle), and one non-irradiated control sample (open gray diamond)

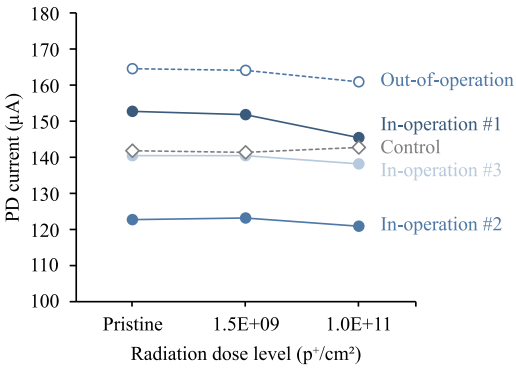


Fig. 7 Output current at 150 μW input versus radiation dose three in-operation samples (filled blue circles), one out-of-operation sample (open blue circle), and one non-irradiated control sample (open gray diamond)

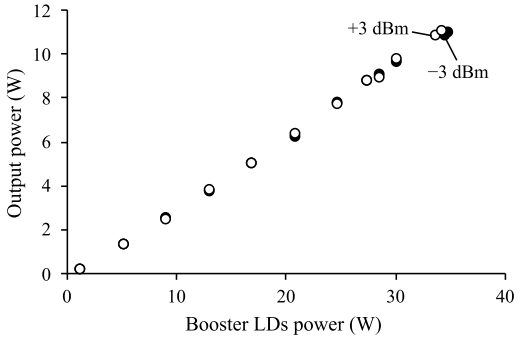


Fig. 8 Output power versus pumping power for inputs of −3 dBm (filled) and +3 dBm (open)

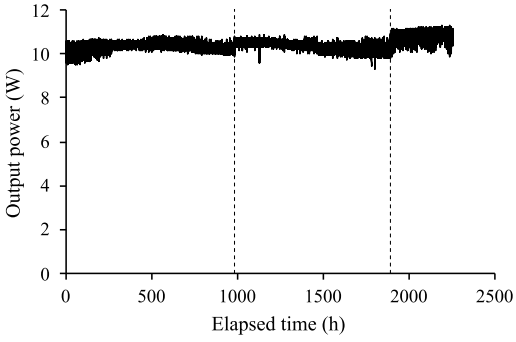


Fig. 9 Output power (solid line) versus elapsed time: at elapsed times of 990 and 1870 hours (dashed line), the amplifier was restarted.

### 4.2. Energy Conversion Efficiency

The estimated energy conversion efficiency at each part of the amplifier at output power of 10 W is shown in Table 4. The amplifier achieved a total wall-plug efficiency of 10.1% measured at 10.8 W operation under STP.

### 4.3. Long-Term Operation under STP

Under STP, long-term operation was applied to an experimental model of the amplifier, which has the same optical structure as the one described in §4.1. No power degradation was observed (Fig. 9). This indicates that the photodarkening effect was sufficiently small. Additionally, although the input signal had high coherence, this caused

Table 4 Estimated energy conversion efficiency at each part of the amplifier under STP: the total input power consists of the items shown in bold. Upright: electrical power; italic: optical power

| Item | Input (W) | Output (W) | Efficiency | Consumption (W) |
|---|---|---|---|---|
| **LD driver #1** | 0.4 | — | — | 0.4 |
| **LD #1 DC-DC** | 5.9 | 4.2 | 71.3% | 1.7 |
| LD #1 e-o | 4.2 | *2.2* | 52.9% | 2.0 |
| Preamplifier o-o | *2.2* | *0.3* | 12.9% | 1.9 |
| **LD driver #2 & #3** | 11.4 | — | — | 11.4 |
| **LD #2 & #3 DC-DC** | 75.0 | 54.8 | 73.0% | 20.2 |
| LD #2 & #3 total e-o | 54.8 | *31.5* | 57.5% | 23.3 |
| Booster amplifiers #2 & #3 o-o | *31.5* | *10.0* | 31.8% | 21.5 |
| **Other electrical components** | 5.4 | — | — | 5.4 |
| **Total wall-plug efficiency** | **98.1** | ***10.0*** | **10.1%** | **88.1** |

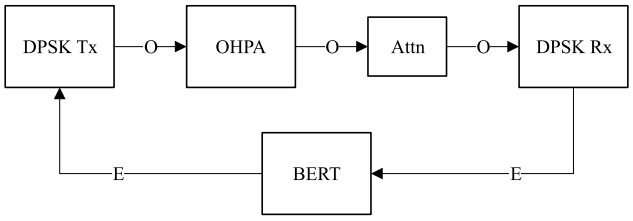


Fig. 10 Communication test system setup: DPSK Tx: DPSK transmitter, Attn: optical attenuator, DPSK Rx: DPSK receiver, and BERT: bit-error-rate tester

Table 5 Communication test conditions.

| Item | Value |
|---|---|
| Modulation method | DPSK (RZ-33%) |
| Transfer rate | 2.5 Gbps |
| Signal pattern | PRBS $2^{15}-1$ |

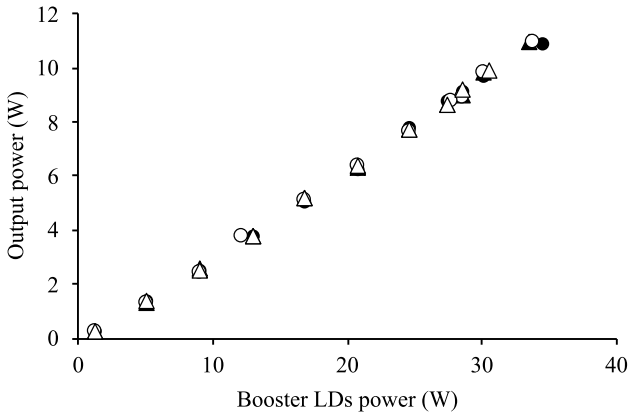


Fig. 11 Output power versus pumping power: before excitation (filled circle), and after *z*-axis (filled triangle), *x*-axis (open circle), and *y*-axis (open triangle) excitation

almost no higher-order transverse mode instability (HOMI), and no power degradation.

### 4.4. Communication Test

The amplifier was subjected to a communication test with the setup shown in Fig. 10 and conditions shown in Table 5. No error was observed throughout 30 s measurement duration, and it shows that the bit-error-rate (BER) value was below $4 \times 10^{-11}$ with the 95% confidence level.

### 4.5. Vibration Test

The amplifier was subjected to a vibration test in the order of *z*-axis, *x*-axis, and *y*-axis excitation (Fig. 12). Almost no power degradation was observed (−0.5% as a measured value) throughout the three-axis test (Fig. 11).

### 4.6. Thermal Vacuum Test

The amplifier was subjected to a thermal vacuum test (Fig. 13) followed by the vibration tests. The test sequence is shown in Fig. 14. During the cycle #1, some function checks with turn-on and turn-off were performed. The temperature range was set to ± 0 to +56°C, taking into account the test margin. Throughout the test, the atmospheric pressure was maintained at $< 1.3 \times 10^{-3}$ Pa.

There was an 8% power degradation observed after vacuuming (Fig. 15). At +56°C, the slope efficiency decreased 12% compared with that at +25°C, while at ± 0°C, the efficiency increased 2%. The change between the initial and post-test measurements was caused by temperature difference. As the OHPA reached the temperature equilibrium, the output power returned. The amplifier emitted over 8.7 W throughout the test in the temperature range of ± 0 to +56°C (Fig. 16). The PER values at ± 0 and +56°C were > 16 dB (Fig. 17). The power limitation was caused by the temperature of the booster LDs becoming higher than the set upper limit, due to the large thermal resistance and temperature variation of the vacuum chamber. In the operating temperature range of ± 0 to +50°C, however, the amplifier emitted > 10 W.

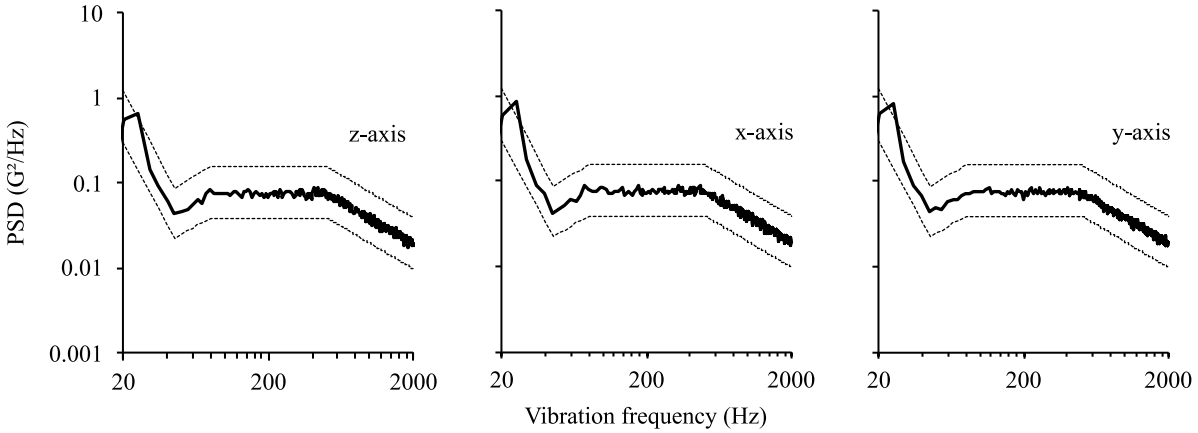


Fig. 12 Power spectral density (PSD) versus vibration frequency: measured values (bold solid) and target conditions ± 3 dB (thin dashed)

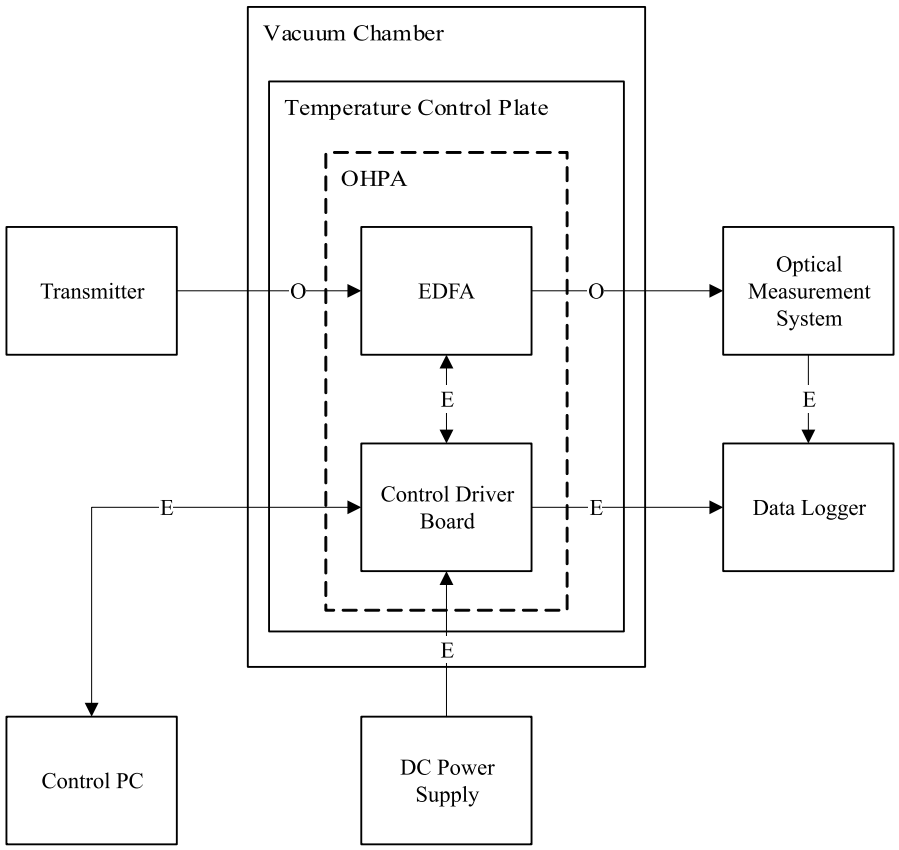


Fig. 13 Setup for the thermal vacuum test

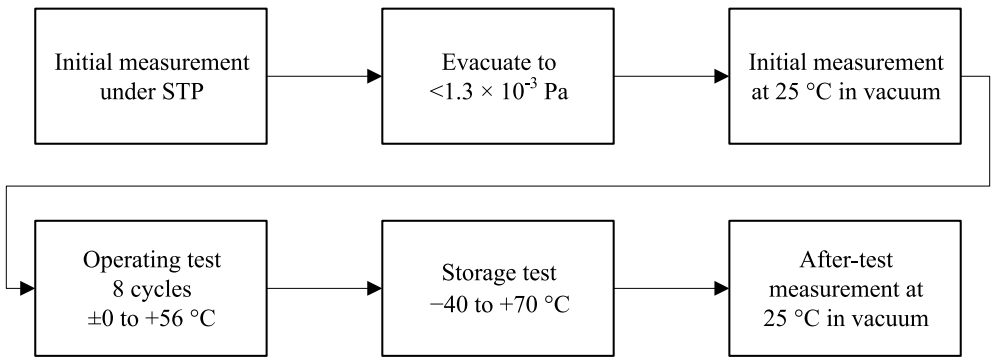


Fig. 14 Test sequence for the thermal vacuum test

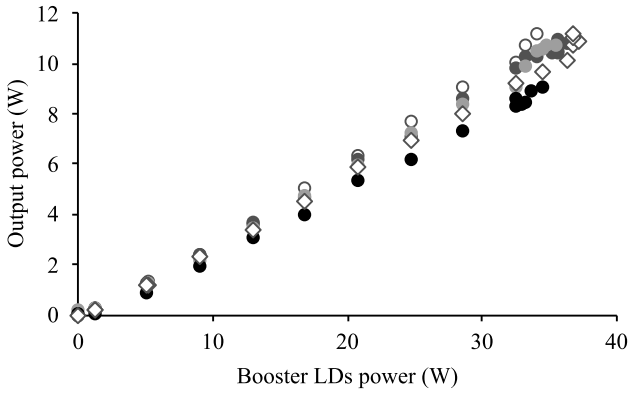


Fig. 15 Output power versus pumping power: initial measurement under STP (open dark gray circle), initial measurement at +25°C in vacuum (filled dark gray circle), ± 0°C in vacuum (filled light gray circle), and +56°C in vacuum (filled black circle), and post-test measurement at +25°C in vacuum (open dark gray diamond)

In the next step, development of the PFM, we plan to revise the design and evaluation setup to improve the thermal conductivity, thereby suppressing the temperature of the LDs.

## 5 Estimated End-of-Life (EOL) Characteristics

The target lifetime of the OHPA is 1500 hours of operation (Table 1). We estimated the EOL characteristics at 25°C of the amplifier. The estimated total wall-plug efficiency was 9.7% and the output decrease factor was expanded, as shown in Table 6.

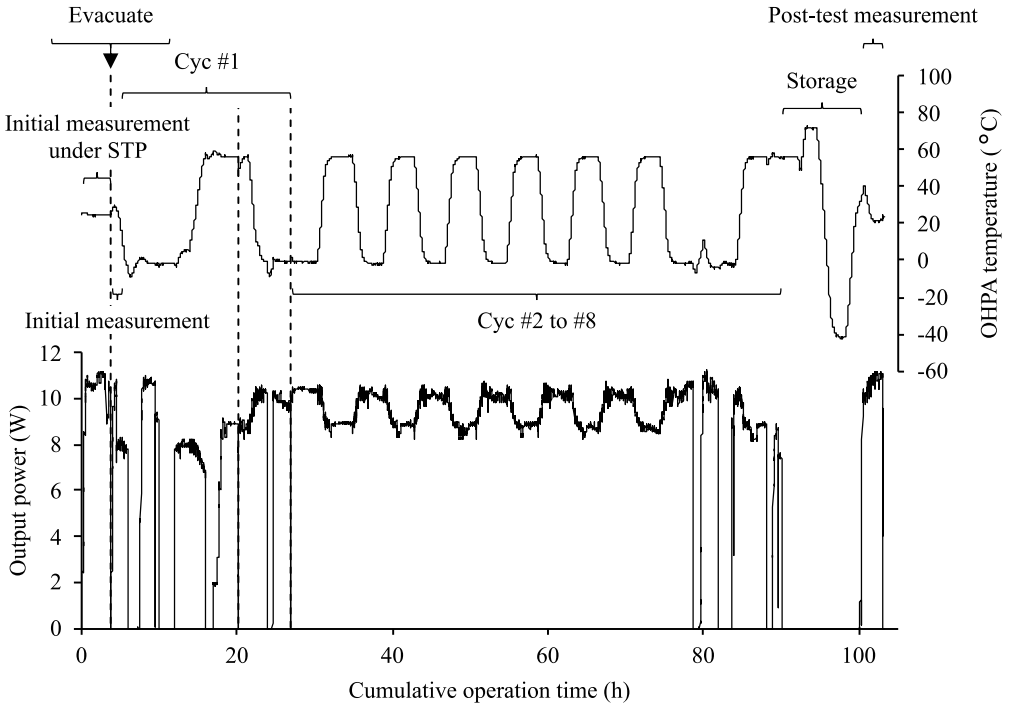


Fig. 16 Optical output power and temperature profiles throughout the test: the dashed lines show suspensions.

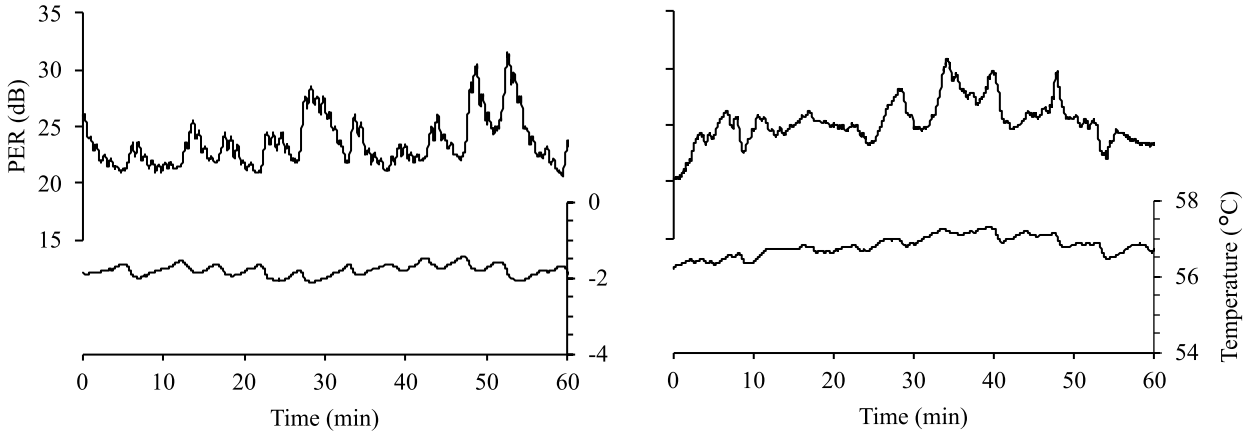


Fig. 17 PER and OHPA temperature time transitions at ± 0 (left) and +56°C (right)

Table 6 Output decrease factors, BOL and EOL specifications, and decrease rates

| Input | BOL | EOL | Difference |
|---|---|---|---|
| LD #1 e-o | 52.9% | 51.0% | −1.9 pp |
| Preamplifier o-o | 12.9% | 12.7% | −0.2 pp |
| LD #2 & #3 total e-o | 57.5% | 55.6% | −1.9 pp |
| Booster amplifiers #2 & #3 o-o | 31.8% | 31.3% | −0.5 pp |
| Other electrical components | 12.0 W | 13.2 W | +1.2 W |
| **Total wall-plug efficiency** | **10.1%** | **9.7%** | **−0.4 pp** |

## 6 Conclusion

We have described our CW single-transverse-mode polarization-maintaining 10 W EYDF amplifier.

The beginning-of-life (BOL) power consumption was 98.1 W at an optical output power of 10 W. The LDs and PDs were subjected to radiation tests, and < 4.7% power degradation of the LDs and almost no changes in the e-o characteristics of the PDs were observed. The amplifier was also subjected to vibration and thermal vacuum tests, and no power degradations were observed. These degradations had little influence on the amplifier's performance. Due to undesirable thermal conditions in the vacuum chamber, the output power was limited to 8.7 W at +56°C, but in the operating temperature range, the amplifier emitted > 10 W. The estimated EOL (1500 hours) power consumption was 102.9 W and the total wall-plug efficiency was 9.7%.

**Acknowledgment.** The authors would like to thank everyone involved in this work at Nikon and JAXA. Furthermore, support for the communication test from the Human Spaceflight Technology Center, Human Spaceflight Technology Directorate, JAXA, is greatly appreciated.

## References

[1] K. Araki, Y. Arimoto, M. Shikatani, M. Toyoda, M. Toyoshima, T. Takahashi, S. Kanda, and K. Shiratama, "Performance evaluation of laser communication equipment onboard the ETS-VI satellite," in *Proc. SPIE* 2699*, Free-Space Laser Communication Technologies VIII*, 1996.

[2] Z. Sodnik, B. Furch, and H. Lutz, "Optical intersatellite communication," *IEEE Journal of Selected Topics in Quantum Electronics,* vol. 16, no. 5, pp. 1051–1057, 2010.

[3] T. Jono, Y. Takayama, K. Shiratama, I. Mase, B. Demelenne, Z. Sodnik, A. Bird, M. Toyoshima, H. Kunimori, D. Giggenbach, N. Perlot, M. Knapek, and K. Arai, "Overview of the inter-orbit and the orbit-to-ground laser communication demonstration by OICETS," in *Proc. SPIE* 6457*, Free-Space Laser Communication Technologies XIX and Atmospheric Propagation of Electromagnetic Waves*, 2007.

[4] T. Araki, "Research and development trends of space optical communications for realizing large capacity communication," *IEICE Communications Society Magazine,* vol. 13, no. 3, pp. 205–215, 2019.

[5] S. Yamakawa, Y. Satoh, T. Itahashi, Y. Takano, S. Hoshi, Y. Miyamoto, M. Sugiho, T. Yoshizawa, Y. Koizumi, M. Yukizane, S. Suzuki, and H. Kohata, "LUCAS: The second-generation GEO satellite-based space data-relay system using optical link," in 2022 *IEEE International Conference on Space Optical Systems and Applications (ICSOS)*, 2022.

[6] H. Kobayashi, R. Kano, T. Seo, Y. Suzuki, E. Mizuta, Y. Hashimoto, T. Araki, and Y. Takada, "Development of a continuous wave single transverse mode polarization-maintaining 10 W Er/Yb-codoped fiber amplifier for space communications," in *Proc. SPIE* 12413*, Free-Space Laser Communications XXXV*, 2023.

小林啓紀　Hiroki KOBAYASHI
先進技術開発本部 光デバイス開発センター
Opto Device Development Center
Advanced Technology Research & Development Division

狩野良子　Ryoko KANO
精機事業本部 半導体装置事業部 開発統括部 第一開発部
1st Development Department
Development Sector
Semiconductor Lithography Business Unit
Precision Equipment Group

瀬尾崇志　Takashi SEO
先進技術開発本部 光デバイス開発センター
Opto Device Development Center
Advanced Technology Research & Development Division

鈴木康史　Yasushi SUZUKI
カスタムプロダクツ事業部 開発部
Development Department
Customized Products Business Unit

水田栄一　Eiichi MIZUTA
宇宙航空研究開発機構
Japan Aerospace Exploration Agency

橋本洋輔　Yosuke HASHIMOTO
宇宙航空研究開発機構
Japan Aerospace Exploration Agency

荒木智宏　Tomohiro ARAKI
宇宙航空研究開発機構
Japan Aerospace Exploration Agency

高田康利　Yasutoshi TAKADA
先進技術開発本部 光デバイス開発センター
Opto Device Development Center
Advanced Technology Research & Development Division

# 高性能反射防止膜“メソアモルファスコート”用超低屈折率多孔質シリカ薄膜の作製

鈴木涼子

# Fabrication of a Porous $SiO_2$ Thin Film with an Ultralow Refractive Index for High Performance Anti-reflective Coatings “Meso Amorphous Coat”†

Ryoko SUZUKI

光学機器を製造・販売しているニコンにおいて，反射防止膜は透過率向上や迷光の抑制のために欠かせない重要な技術である．工業的に広く用いられている多層反射防止膜のなかでも，最上層の低屈折率化はその性能向上に最も大きな影響を与える．低屈折率層には空気を含む多孔質構造が求められるが，光の散乱を防ぐためにはその構造は微細なものでなくてはならない．本稿では簡便なゾル - ゲル法を用いた多層反射防止膜の最上層用の低屈折率薄膜の作製について説明する．反応に用いる原料に適切な分子構造の溶媒と高い塩基性を有する塩基触媒を選択することにより，微細な多孔質構造を有する屈折率1.17の多孔質シリカ薄膜を作製することに成功した．膜構造の観察とシミュレーションにより，低散乱および超低屈折率の形成要因を明らかにした．さらに，作製した膜に疎水性官能基を導入することにより空気中の水分の吸着による屈折率変化を低減した．この薄膜は“メソアモルファスコート”の最上層としてカメラレンズに搭載されている．

Anti-reflective coatings are a key technology in Nikon Corporation, which manufactures optical equipment, for improving transmittance and reducing stray light. A lower refractive index of the top layer in the multilayer antireflective coatings, which is widely used in industry, has the greatest effect on improving its performance. The top layer must have a porous structure containing air, but the structure must be fine to prevent light scattering. This paper describes a simple sol-gel method for fabricating a thin film with a low refractive index for the top layer of a multilayer anti-reflective coating. By selecting solvent with appropriate molecular structures and base catalyst with high basicity as raw materials for the reaction, porous $SiO_2$ thin films with a refractive index of 1.17 and a fine porous structure were successfully fabricated. Observation of the film structure and simulation revealed the formation process of low scattering and ultra-low refractive index. Furthermore, by introducing hydrophobic functional groups into the fabricated films, the variation of refractive index due to the adsorption of moisture in the air was reduced. This thin film is applied to camera lenses as the top layer of “Meso Amorphous Coat”.

**Key words** 反射防止膜，低屈折率膜，光学薄膜，多孔質シリカ，ゾル - ゲル法
anti-reflective coating, low refractive index film, optical thin film, porous silica, sol-gel method

## 1 Introduction

Anti-reflective (AR) coatings are used in various optical products, such as cameras, microscopes, and display panels [1]-[3]. A multilayer AR coating comprises several stacked layers with varying refractive indices [4]. Among these layers, the top layer contributes the most to AR performance. Decreasing the refractive index (n) of the top layer is necessary to improve AR performance. $MgF_2$ has the lowest refractive index (n = 1.38) but is not sufficiently low for AR coatings [5].

Most low refractive index materials possess a porous structure. The total refractive index of an AR film can be reduced by forming pores containing air (n = 1) in the film. To date, various porous materials, such as $CaF_2$, $MgF_2$, and $Al_2O_3$ have been synthesized [6]–[8]. In particular, $SiO_2$ was

† This paper uses the following copyrighted work with modifications (*).
Ryoko Suzuki, “Fabrication of a porous $SiO_2$ thin film with an ultralow refractive index for anti-reflective coatings,” *J Sol-Gel Sci Technol*, vol. **106**, pp. 860–868, 2023. (https://doi.org/10.1007/s10971-023-06108-8) ©Suzuki, R. 2023 Licensed under CC BY 4.0 (http://creativecommons.org/licenses/by/4.0/)
* Main content of the modifications
The title, abstract, and author are translated into Japanese, and both English and Japanese are printed.

focused on materials for preparing porous structures [9]–[11]. The use of large amount of air to decrease the refractive index of a film tends to cause considerable scattering of light [12], [13]. Moreover, these materials have unstable refractive indices because their pores adsorb moisture from the air easily [14]. To prevent the adsorption of moisture, hydrophilic Si-OH groups of the film surface are often capped. However, the refractive index of the film increases unless the amount of capping agent is controlled [15], [16].

Many studies have reported that a multi-coating of a porous film that contains $SiO_2$ and whose refractive index is lesser than 1.20 can achieve high transmittance [17], [18]. Therefore, a thin film with $n < 1.20$ is required for AR coating. However, porous $SiO_2$ thin films prepared via sol-gel reactions often contain large $SiO_2$ particles (several tens of nanometers) in their inner structure and exhibit large Rayleigh scattering, which decreases the transmittance of the film [5], [19], [20]. Therefore, a finely structured thin film of porous $SiO_2$ is required for optical applications. In this study, an easy sol-gel method was used to prepare porous $SiO_2$ thin films. The obtained porous $SiO_2$ films exhibited low light scattering and were humidity resistant. In addition, structural analysis and calculations were conducted, and the factors responsible for the low refractive index and scattering were discussed.

## 2 Experiment

### 2.1. Materials

Tetramethyl orthosilicate (TMOS; Tokyo Chemical Industry Co., Ltd., Tokyo, Japan) was used as the silica source. 1-Methoxy-2-propanol (PGME; FUJIFILM Wako Pure Chemical Corporation, Osaka, Japan) was used as a solvent. Triethylamine (TEA; Tokyo Chemical Industry Co., Ltd., Tokyo, Japan) was used as the catalyst for the sol-gel reaction. Hexamethyldisilazane (HMDS; Tokyo Chemical Industry Co., Ltd., Tokyo, Japan) was used for the surface treatment of the porous $SiO_2$ thin films.

### 2.2. Sample Preparation

The typical preparation methods are described in this section. First, PGME (54.43 g) was poured into a polytetrafluoroethylene (PTFE) bottle. $H_2O$ (1.731 $\mu$L), TEA (36.10 $\mu$L), and TMOS (7.310 g) were then added into the bottle at a molar ratio of TMOS : $H_2O$ : TEA = 1 : 2 : 0.01 and stirred for ~27 h at the room temperature. The as-prepared coating liquid containing 4.54 wt% of $SiO_2$ was filtered using a PTFE filter having a pore size of 5.0 $\mu$m and then spin-coated onto a substrate. The films thus obtained were heated to 160°C for 3 h to obtain a film denoted as $SiO_2$_PGME_TEA. After heating, the $SiO_2$_PGME_TEA was treated with HMDS to enhance its hydrophobicity. Subsequently, the film, which was coated on a substrate with 30 mm diameter, was sealed in a closed vessel with HMDS (0.6135 $\mu$L) for 24 h at room temperature. Finally, the product was heated at 60 °C for 0.5 h to form $SiO_2$_HMDS.

## 3 Results and Discussions

### 3.1. Effect of Solvent on $SiO_2$ Thin Films

The relationship between the sol-gel reaction time and the refractive index of the films was investigated. In addition, the experiment was repeated with different solvents namely, PGME, methanol, 1-propanol, and 1-pentanol, to investigate the effect of a solvent on the relationship. Figure 1 shows the relationship between the sol-gel reaction time and the refractive index of the prepared films. In all cases, the refractive index decreased with reaction time. This behavior was consistent with previously reported results [21]. The behavior is attributed to generating a bulky structure that consists of $SiO_2$ and enlarges over time in the reaction mixture. The bulkier the $SiO_2$ structure, the more the number of and larger pores, formed that contain air. Therefore, the refractive index of the thin films decreases over time. The largest decrease in the refractive index was observed when 1-pentanol was used as a solvent. The refractive indices of the thin films prepared using methanol and 1-propanol were almost equal ($n \sim 1.20$).

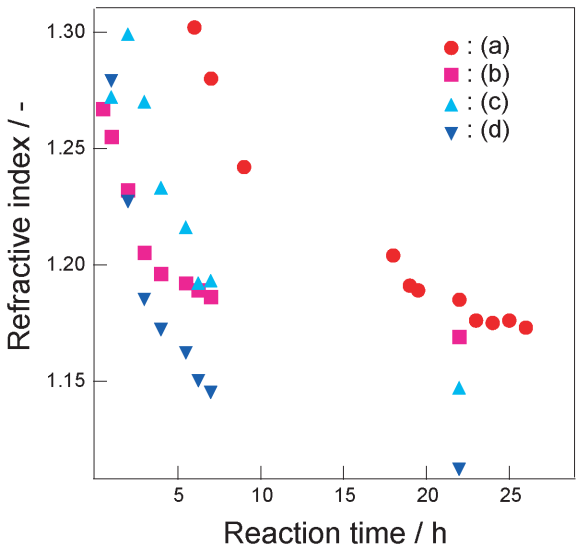


Fig. 1 Relationship between the sol-gel reaction time and the refractive index of thin films prepared with (a) PGME, (b) methanol, (c) 1-propanol, and (d) 1-pentanol as solvents

Figure 2 shows the relationship between refractive index of the film prepared from the coating liquid reacted for an arbitrary time and transmittance at 350 nm of the same coating liquid for different solvents. In all cases, the transmittance and refractive index decreased with reaction time simultaneously. As shown in Fig. 1, $SiO_2$ structures grew and aggregated in coating liquid during the sol-gel reaction, which increased the porosity of the $SiO_2$ thin films. Figure 2 provides data to consider how $SiO_2$ fine structure can be formed without particle growth and aggregation, increasing scattering and decreases transmittance. The transmittance corresponding to PGME was higher than that corresponding to methanol and 1-propanol when the refractive indices of the thin films were almost the same; for example, the refractive index was approximately 1.20. The reaction mixture containing 1-pentanol exhibits the highest transmittance. These results indicate that finely structured $SiO_2$ was formed when PGME and 1-pentanol were used as solvents.

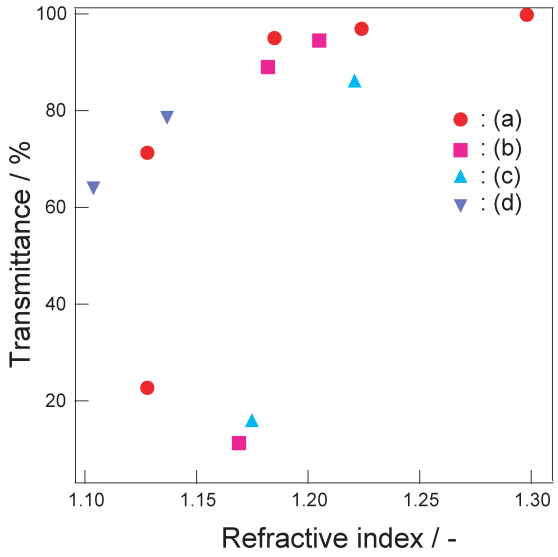


Fig. 2 Relationship between refractive index of the thin film and the corresponding transmittance at 350 nm of the same coating liquid prepared using (a) PGME, (b) methanol, (c) 1-propanol, and (d) 1-pentanol

The results showed transesterification occurred between the methoxy group of TMOS and the solvent during the sol-gel reaction. The reactivity of silanes that underwent transesterification was lower than that of TMOS, possibly because silanes contain a bulkier alkoxy group than TMOS. The bulky alkoxy group on the surface of the $SiO_2$ structure prevented the aggregation of the $SiO_2$ particles. The transesterification reaction also prevented the growth and aggregation of $SiO_2$ structures. In addition, PGME is considered a suitable solvent for controlling the refractive index of AR coatings because it tends to reduce the refractive index near 1.20 gradually.

Figure 3 shows the photographs and optical microscopic images of the thin films prepared in this study. As shown in Fig. 3a-b, radial striations can be observed in the $SiO_2$ thin film surface prepared using methanol. In contrast, thin films prepared using 1-propanol (Fig. 3c-d), 1-pentanol (Fig. 3e-f), and PGME (Fig. 3g-h) exhibit smooth surfaces.

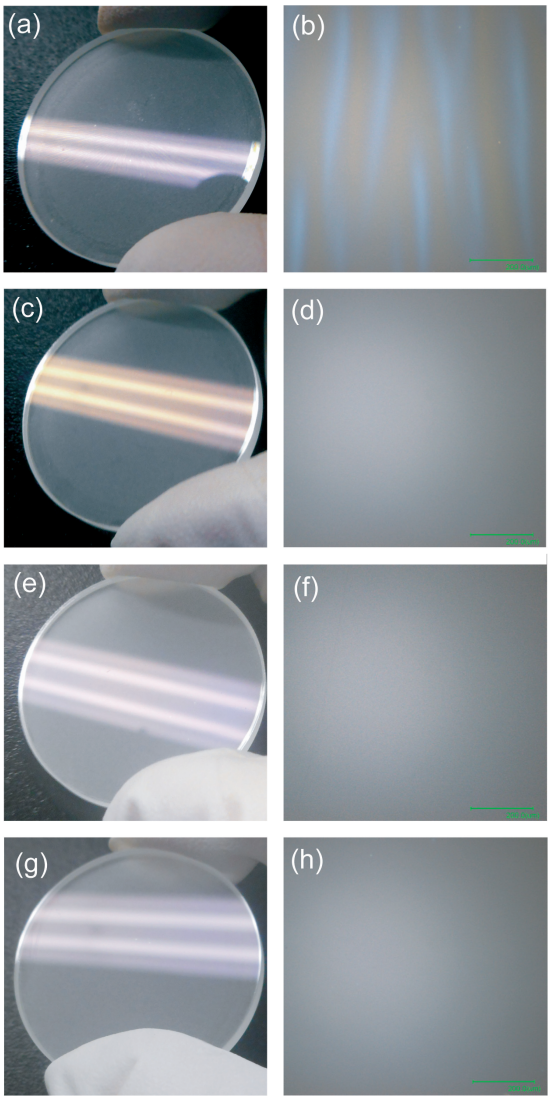


Fig. 3 Appearance of a thin film prepared using a coating liquid containing (a) methanol, (c) 1-propanol, (e) 1-pentanol, and (g) PGME; (b), (d), (f), and (h) represent the corresponding optical microscopic images. (Scale bar in b, d, f, and h represents 200 μm.)

From the above results, PGME can be considered a suitable solvent for fabricating porous silica thin films as AR coating from view points of control of refractive index and appearance.

### 3.2. Effect of the Base on the Structure of Porous $SiO_2$ Thin Films

To investigate the effect of the base on the structure of $SiO_2$ thin films, $SiO_2$ thin films were prepared using $NH_3$,

propylamine (PA), and diethylamino (DEA) in place of TEA in the original preparation method. In each experiment, the refractive index of the thin films was adjusted to n = 1.17 by controlling the reaction time.

Figure 4 shows the cross-sectional SEM images of the thin films. A $SiO_2$ framework comprising small connected particles was observed in all porous $SiO_2$ thin films. In Fig. 4, the diameter of a $SiO_2$ primary particle was considered corresponding to the thickness of the framework. Therefore, the $SiO_2$ primary particle diameter was measured at four points and averaged in each SEM image. $SiO_2$_PGME_$NH_3$ (Fig. 4a) and $SiO_2$_PGME_PA (Fig. 4b) possessed thick frameworks. The second thinnest and thinnest frameworks were observed in $SiO_2$_PGME_DEA (Fig. 4c) and $SiO_2$_PGME_TEA (Fig. 4d), respectively. The thicknesses of the $SiO_2$_PGME_$NH_3$, $SiO_2$_PGME_PA, $SiO_2$_PGME_DEA, and $SiO_2$_PGME_TEA frameworks, measured using their SEM images, were 15.8 nm, 15.3 nm, 11.0 nm, and 9.8 nm, respectively.

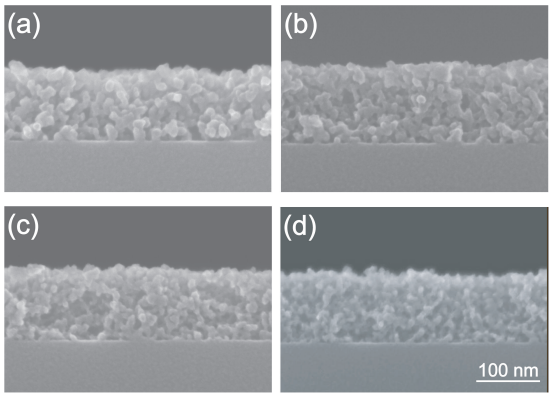


Fig. 4 Cross-sectional SEM images of (a) $SiO_2$_PGME_$NH_3$, (b) $SiO_2$_PGME_PA, (c) $SiO_2$_PGME_DEA, and (d) $SiO_2$_PGME_TEA

Table 1 shows the amount of scattered light at 350 nm by thin films. The amount of light scattered by $SiO_2$_PGME_PA was the highest, whereas that scattered by $SiO_2$_PGME_TEA was the smallest.

Figure 5 shows the viscosity of the reaction mixture to reaction time. The viscosity increased with reaction time for samples prepared using PA, DEA, and TEA catalysts. Notably, the maximum increase in viscosity is observed for TEA. The type of basic catalyst affected the formation of $SiO_2$ because of the inductive effect, steric hindrance of the catalysts and solvent [22]. The pKa values of $NH_3$, propylamine, diethylamine and triethylamine in water are 9.21, 10.53, 10.98 and 10.65, respectively [23]. It means that basicity decreases in the order diethylamine > triethylamine > propylamine > $NH_3$. However, the pKa values listed here are those in water, which have been widely reported, and these values vary with the solvent. It has been reported that tertiary amines may have a higher pKa than secondary amines in organic solvents [24]. This is owing to the stability of the generated cationic species in the solvent and other factors. Therefore, it must be noted that the reaction of this study was carried out in an organic solvent, mainly PGME. Furthermore, the composition of solvent was changed with the progress of reaction owing to methanol produced by hydrolysis. Therefore, discussing the reactivity of the base from the pKa value of a particular solvent is difficult. However, TEA has the highest reactivity in PGME than other bases. This may be because TEA has three alkyl chains, which are electron-donating groups, and the $NH(C_2H_5)^{3+}$ generated from TEA has stability in organic solvents owing to its three alkyl chains. SEM images and viscosity measurements showed that small $SiO_2$ nanoparticles were simultaneously generated and interconnected when TEA was used as a basic catalyst.

Table 1 Amount of scattered light at 350 nm by the porous $SiO_2$ thin films

| | Amount of scattering at 350 nm/ppm |
|---|---|
| $SiO_2$_PGME_$NH_3$ | 248 |
| $SiO_2$_PGME_PA | 388 |
| $SiO_2$_PGME_DEA | 265 |
| $SiO_2$_PGME_TEA | 204 |

These results indicate that the structure of the porous $SiO_2$ thin films differed depending on the organic base used. In particular, a fine-structured low-scattering film was obtained using a highly basic catalyst (TEA). However, gelation did not

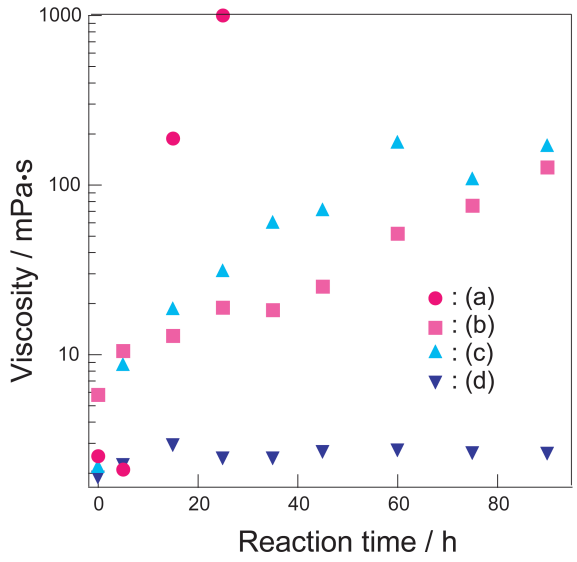


Fig. 5 Viscosity of the reaction mixture containing (a) TEA, (b) DEA, (c) PA, and (d) $NH_3$ as the catalyst to reaction time

proceed when $NH_3$ was used as a basic catalyst. The refractive index of the thin film could be decreased by interlinking small $SiO_2$ nanoparticles using TEA and by growing $SiO_2$ nanoparticles using $NH_3$. In conclusion, TEA is a suitable catalyst for synthesizing porous $SiO_2$ thin films for AR coating.

### 3.3. Inner and Surface Structure of a Thin Film

The Structural characteristics of $SiO_2$_PGME_TEA (n = 1.17) were investigated. Figure 6 shows the pore distribution measured via positron annihilation spectroscopy. Two peaks were observed at 0.48 nm and 2.4 nm. The peak at 0.48 nm could be attributed to the gap in the siloxane framework [25] and that at 2.4 nm could be ascribed to the presence of pores in $SiO_2$ films.

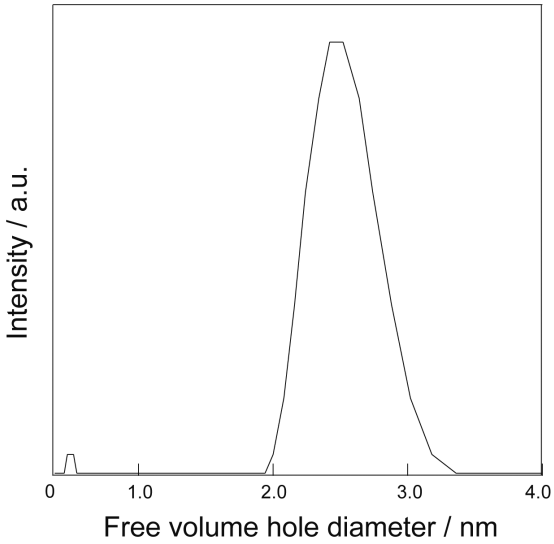


Fig. 6 Pore size distribution of $SiO_2$_PGME_TEA (n = 1.17) measured using positron annihilation spectroscopy

Figure 7 shows a 3D-TEM image of $SiO_2$_PGME_TEA. The colored areas represent pores that were detected by image analysis. Several pores were distributed inside the film. Image analysis also revealed the pore distribution, which showed that the pore diameter was in the range of 2–3 nm. This is consistent with the results induced via positron annihilation spectroscopy. Additionally, porosity was calculated to be 65 vol % via image analysis. Considering that the refractive index calculated from the reflectance measurement was n = 1.17, the porosity of the film was calculated from the Lorentz–Lorentz formula using the refractive index of $SiO_2$ and air and their volume fractions [26]. The porosity calculated using the refractive index was 62.2 vol %. This result indicates that a 3D-TEM structural analysis was appropriate. Therefore, $SiO_2$_PGME_TEA was confirmed to possess abundant pores of diameter 2–3 nm and a high porosity of over 60 vol%. This high porosity was attributed to the bulky colloidal $SiO_2$ structure grown in the coating liquid. If $SiO_2$ in the coating liquid were mono-dispersed spherical particles, the porosity of porous $SiO_2$ thin films would be 49.4 vol%, as calculated using Structure of NAno Particles (SNAP) simulation [27], [28]. This shows that the $SiO_2$ in the coating liquid possessed a bulky structure formed by connecting small $SiO_2$ nanoparticles. Because bulky $SiO_2$ structures could not be densely packed like mono-dispersed spherical nanoparticles, they formed a highly porous $SiO_2$ thin film.

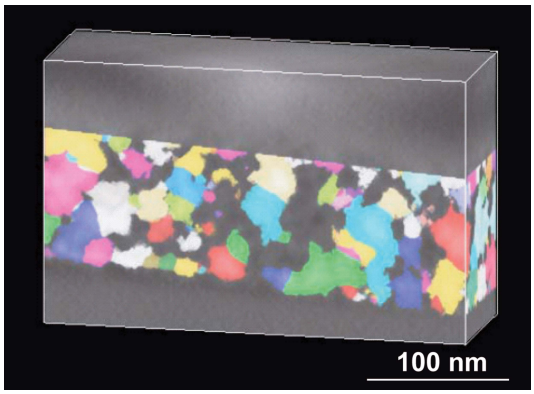


Fig. 7 3D-TEM image of $SiO_2$_PGME_TEA
The refractive indices of the films were adjusted to n = 1.17. Colored areas were detected pores using image analysis.

The size of the pores in $SiO_2$_PGME_TEA (2–3 nm) was smaller than the wavelength of visible light, indicating that $SiO_2$_PGME_TEA can exhibit a low scattering of light [29].

### 3.4. Enhanced Hydrophobicity of $SiO_2$_PGME_TEA

The adsorption of moisture from air into porous $SiO_2$ was reported to increase the refractive index [14]. When porous $SiO_2$ is used for AR coating, increasing the refractive index affects the optical properties. Therefore, the Si-OH groups in $SiO_2$_PGME_TEA should be capped by hydrophobic groups. HMDS was used for capping the Si-OH groups because it is commonly used for hydrophobization [30].

In the infrared reflection-absorption spectra (IR-RAS) (Fig. 8) of $SiO_2$_PGME_TEA and $SiO_2$_HMDS, an adsorption band at 1250 $cm^{-1}$ was observed in only $SiO_2$_HMDS, which was assigned to $\nu$(Si-C) [31]. It showed that HMDS was introduced into $SiO_2$_PGME_TEA.

In addition, the contact angles of $SiO_2$_PGEM_TEA and $SiO_2$_HMDS were measured to be 8.7° and 65°, respectively (Fig. 9). This indicated that $SiO_2$_PGEM_TEA possessed a hydrophilic surface, whereas $SiO_2$_HMDS possessed a hydrophobic surface. These results revealed that HMDS successfully capped the Si-OH group and increased the

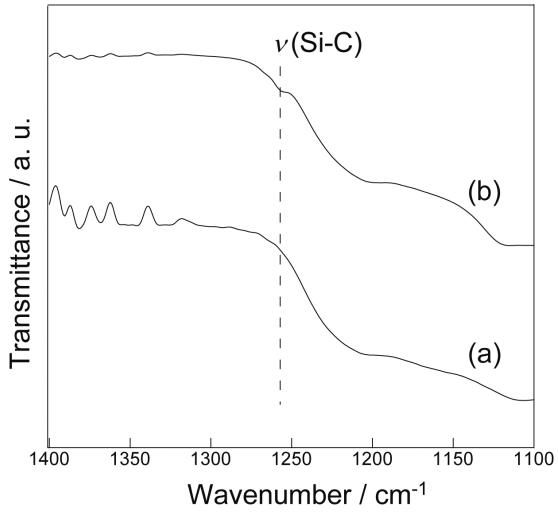


Fig. 8 IR-RAS spectra of $SiO_2$_PGME_TEA (a) before and (b) after HMDS treatment

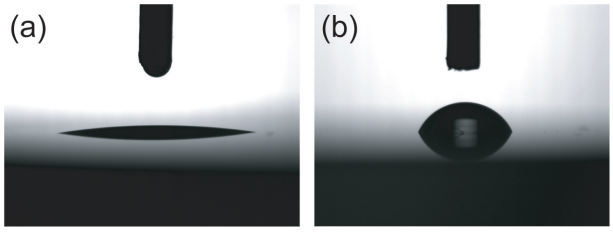


Fig. 9 Contact angle measurement of $SiO_2$_PGME_TEA (a) before and (b) after HMDS treatment

hydrophobicity of $SiO_2$_PGME_TEA.

The refractive indices of $SiO_2$_PGME_TEA and $SiO_2$_HMDS are listed in Table 2. The refractive index of $SiO_2$_HMDS was higher than that of $SiO_2$_PGME_TEA. It probably indicated that HMDS was introduced into the pores of $SiO_2$_PGME_TEA. Moreover, the changes in refractive indices after keeping the films at 24°C and 35% relative humidity for 7 d were compared. The increase in the refractive index of $SiO_2$_HMDS was smaller than that of $SiO_2$_PGME_TEA for 7 d.

Table 2 Refractive indices of $SiO_2$_PGME_TEA and $SiO_2$_HMDS on 0, and 7 d

| | n on day 0/ - | n on day 7/ - | Increase in n after 7 d/ - |
|---|---|---|---|
| $SiO_2$_PGME_TEA | 1.170 | 1.212 | 0.042 |
| $SiO_2$_HMDS | 1.197 | 1.209 | 0.012 |

Hence, the HMDS treatment prevented an increase in the refractive index of the porous $SiO_2$ thin films via the capping of the Si-OH groups.

## 4 Conclusion

Porous $SiO_2$ thin films having low refractive indices were successfully prepared via a simple sol-gel method. The choice of solvent and basic catalyst is a key factor for controlling the reactivity of the coating liquid and forming a smooth film that exhibits low scattering. The porous $SiO_2$ thin film fabricated in this study could be used as a broadband AR coating with stacked undercoating and as a lens and sensor in various optical devices.

**Acknowledgements.** The author wishes to acknowledge Mr. Masahiro Ousaka (Nikon Corp.) for the valuable simulation using SNAP.

## References

[1] H. G. Shanbhogue, C. L. Nagendra, M. N. Annapurna, S. A. Kumar, and G. K. M. Thutupalli, "Multilayer antireflection coatings for the visible and near-infrared regions," *Appl. Opt.*, vol. 36, pp. 6339–6351, 1997.

[2] X. Li, J. Gao, L. Xue, and Y. Han, "Porous polymer films with gradient-refractive-index structure for broadband and omnidirectional antireflection coatings," *Adv. Funct. Mater.*, vol. 20, pp. 259–265, 2010.

[3] D. Chen, "Anti-reflection (AR) coatings made by sol-gel processes: a review," *Solar Sol. Energy Mater. Sol. Cells*, vol. 68, pp. 313–336, 2001.

[4] X. Sun, J. Tu, L. Li, W. Zhang, and K. Hu, "Preparation of wide-angle and abrasion-resistant multi-layer antireflective coatings by $MgF_2$ and $SiO_2$ mixed sol," *Colloids Surf., A*, vol. 602, 125106, 2020.

[5] X. Zhang, P. Lan, Y. Lu, J. Li, H. Xu, J. Zhang, Y. P. Lee, J. Y. Rhee, K. L. Choy, and W. Song, "Multifunctional antireflection coatings based on novel hollow silica–silica nanocomposites," *ACS Appl. Mater. Interfaces*, vol. 6, pp. 1415–1423, 2014.

[6] I. M. Thomas, "Porous fluoride antireflective coatings," *Appl. Opt.*, vol. 27, pp. 3356–3358, 1988.

[7] S. Fujihara, Y. Kadota, and T. Kimura, "Role of organic additives in the sol-gel synthesis of porous $CaF_2$ antireflective coatings," *J. Sol-Gel Sci. Tech.*, vol. 24, pp. 147–154, 2002.

[8] N. Yamaguchi, K. Tadanaga, A. Matsuda, T. Minami, and M. Tatsumisago, "Antireflective properties of flowerlike alumina thin films on soda-lime silica glass substrates prepared by the sol-gel method with hot water treatment," *Thin Solid Films*, vol. 515, pp. 3914–3917, 2007.

[9] I. M. Thomas, "High laser damage threshold porous silica antireflective coating," *Appl. Opt.*, vol. 25, pp. 1481–1483, 1986.

[10] J. Moghal, J. Kobler, J. Sauer, J. Best, M. Gardener, A. A. R. Watt, and G. Wakefield, "High-performance, single-layer antireflective optical coatings comprising mesoporous silica nanoparticles," *ACS Appl. Mater. Interfaces*, vol. 4, pp.

854–859, 2012.

[11] A. Vincent, S. Babu, E. Brinley, A. Karakoti, S. Deshpande, and S. Seal, "Role of catalyst on refractive index tunability of porous silica antireflective coatings by sol-gel technique," *J. Phys. Chem. C*, vol. 111, pp. 8291–8298, 2007.

[12] M. P. J. Peeters and M. R. Bohmer, "Optical application of (pigmented) sol-gel coatings," *J. Sol-Gel Sci. Technol.*, vol. 26, pp. 57–62, 2003.

[13] C. Murray, C. Flannery, I. Streiter, S. E. Schulz, M. R. Baklanov, K. P. Mogilnikov, C. Himcinschi, M. Friedrich, D. R. T. Zahn, and T. Gessner, "Comparison of techniques to characterise the density, porosity and elastic modulus of porous low-*k* $SiO_2$ xerogel films," *Microelectron. Eng.*, vol. 60, pp. 133–141, 2002.

[14] Z. Wang and Z. Gu, "Optical humidity-sensitive mechanism based on refractive index variation," *Chin. Opt. Lett.*, vol. 7, pp. 756–759, 2009.

[15] W. Dou, P. Wang, D. Zhang, and J. Yu, "An efficient way to prepare hydrophobic antireflective $SiO_2$ film by sol-gel method," *Mater. Lett.*, vol. 167, pp. 69–72, 2016.

[16] S. Zhang, P. Xiao, P. Wang, J. Luo, and B. Jiang, "Spherical-chain silica with super-hydrophobic surface and ultra-low refractive index for multi-functional broadband antireflective coatings," *Sol. Energy*, vol. 207, pp. 1222–1230, 2020.

[17] X. Huang, Y. Yuan, S. Liu, L. Zhang, and R. Hong, "Preparation of hydrophobic broadband antireflective $SiO_2$ coating on flexible poly (methyl methacrylate) substrates," *Colloid Surf. A-Physicochem. Eng. Asp.*, vol. 538, pp. 519–525, 2018.

[18] H. T. Hsu, C. Y. Ting, C. Y. Mou, and B. Z. Wan, "Nanoporous $SiO_2$ films prepared by surfactant templating method - a novel antireflective coating technology," *Stud. Surf. Sci. Catal.*, vol. 146, pp. 539–542, 2003.

[19] H. Ren, J. Zhu, Y. Bi, Y. Xu, and L. Zhang, "Assembly of methylated hollow silica nanospheres toward humidity-resistant antireflective porous films with ultralow refractive indices," *J. Porous Mater.*, vol. 25, pp. 55–62, 2018.

[20] J. H. Rouse and G. S. Ferguson, "Preparation of thin silica films with controlled thickness and tunable refractive index," *J. Am. Chem. Soc.*, vol. 125, pp. 15529–15536, 2003.

[21] K. Makita, Y. Akamatsu, and A. Takamatsu, "Sol-gel preparation of silica films with controlled surface morphology and their application to a low reflective glass," *J. Sol-Gel Sci. Technol.*, vol. 14, pp. 175–186, 1999.

[22] R. D. Hancock, B. S. Nakani, and F. Marsicano, "Relationship between Lewis acid-base behavior in the gas phase and in aqueous solution. 1. role of inductive, polarizability, and steric effects in amine ligands," *Inorg. Chem.*, vol. 22, pp. 2531–2535, 1983.

[23] J. F. Coetzee and G. R. Padmanabhan, "Properties of bases in acetonitrile as solvent. IV. proton acceptor power and homoconjugation of mono- and diamines," *J. Am. Chem. Soc.*, vol. 87, pp. 5005–5010, 1965.

[24] M. D. Cantu, S. Hillebranda, and E. Carrilho, "Determination of the dissociation constants ($pK_a$) of secondary and tertiary amines in organic media by capillary electrophoresis and their role in the electrophoretic mobility order inversion," *J. Chromatogr. A*, vol. 1068, pp. 99–105, 2005.

[25] M. Misheva, N. Djourelov, F. M. A. Margaca, and I. M. M. Salvado, "Positronium study of porous structure of sol-gel prepared $SiO_2$: influence of pH," *J. Non-Cryst. Solids*, vol. 279, pp. 196–203, 2001.

[26] P. Falcaro, D. Grosso, H. Amenitsch, and P. Innocenzi, "Silica orthorhombic mesostructured films with low refractive index and high thermal stability," *J. Phys. Chem. B*, vol. 108, pp. 10942–10948, 2004.

[27] K. Hasegawa, A. Nasu, and M. Fuita, "Behavior analysis of coating layer particles in cosmetic materials during drying by observation and computational simulation," *Mathematical Monographs*, vol. 9, pp. 75–88, 2016.

[28] M. Fujita and Y. Yamaguchi, "Development of three-dimensional structure formation simulator of colloidal nanoparticles during drying," *J. Chem. Eng. Jpn.*, vol. 39, pp. 83–89, 2006.

[29] P. K. Jain, K. S. Lee, I. H. El-Sayed, and M. A. El-Sayed, "Calculated absorption and scattering properties of gold nanoparticles of different size, shape, and composition: applications in biological imaging and biomedicine," *J. Phys. Chem. B*, vol. 110, pp. 7238–7248, 2006.

[30] O. Nalamasu, M. Cheng, A. G. Timko, V. Pol, E. Reichmanis, and L. F. Thompson, "An overview of resist processing for deep-UV lithography," *J. Photopolym. Sci. Technol.*, vol. 4, pp. 299–318, 1991.

[31] T. Hirotsu and C. Tagaki, "Plasma copolymer membranes of acrylic acid and the adsorption of lysozyme on the surface," *Thin Solid Films*, vol. 457, pp. 20–25, 2004.

鈴木涼子　Ryoko SUZUKI
先進技術開発本部 材料・要素技術研究所
Materials & Advanced Research Laboratory
Advanced Technology Research & Development Division

鈴木涼子
Ryoko SUZUKI

# フッ化物リン酸塩ガラスの光学特性と局所構造に対するO/P比の寄与

吉本幸平，上田　基，山本優也，水口雅史

# Impact of the O/P Ratio on the Optical Properties and Structures of Fluoride–Phosphate Glass†

Kohei YOSHIMOTO, Motoi UEDA, Yuya YAMAMOTO and Masafumi MIZUGUCHI

フッ化物リン酸塩ガラスは，低屈折率・低分散，良好な紫外域透過率，正の異常分散など特異な光学特性を有することから光学材料として多用されている．しかし，その組成の複雑さのためか，光学特性や構造の組成依存性に関する系統的な知見は少ない．本研究では，$Ca(PO_3)_2$–$AlF_3$–$CaF_2$–$BaF_2$–BaO系フッ化物リン酸塩ガラスを溶融急冷法により作製し，その光学特性や構造の組成依存性をO/P比に着目して評価した．結果，ガラスの光学特性や局所構造が，O/P比に対して非線形的な挙動を示すことが明らかとなった．例えば，O/P=3.0–3.4におけるバンドギャップエネルギーは概ね一定であるが，O/P比が3.6から4.0にかけて急激な低下を示した．また，Lorentzモデルに基づく屈折率分散の解析から，バンドギャップエネルギーと同様に紫外域の共鳴周波数もO/P=3.6–4.0において急激に低下することが明らかになった．さらに，赤外吸収分光法およびラマン散乱分光法によるガラスの局所構造解析から，O/P比が3.6から4.0にかけて，リン酸鎖の切断や孤立$Q^0$構造の増加など，劇的な構造変化が生じることも示唆された．前記光学特性と局所構造の特徴的なO/P比依存性を包括するメカニズムを示すため，電気陰性度や光学的塩基度の考え方を活用して原子間の化学結合状態に基づく考察を行った．

$Ca(PO_3)_2$–$AlF_3$–$CaF_2$–$BaF_2$–BaO glasses were prepared by the melt quenching method, and the effects of the O/P ratio on the optical properties and glass structure were investigated. The bandgap energy showed no significant change at O/P = 3.0–3.4 but drastically decreased with the increase in the O/P from 3.6 to 4.0. In addition, the refractive index dispersion was analyzed based on the Lorentz model, and it was found that the decrease in the resonance frequency in the ultraviolet region with the increase in the O/P ratio resulted in an increase in the refractive index and dispersion. Analysis of the infrared absorption and Raman scattering spectra revealed that the phosphate chains were broken, and isolated $Q^0$ units were generated with the increase in the O/P ratio from 3.6 to 4.0. Based on the structural change of the glass, the origin of the nonlinear dependence of the optical properties on the O/P ratio was discussed.

**Key words** フッ素化合物，ガラス，光学材料／光学特性，リン酸，構造
fluorine/fluorine compounds, glass, optical materials/properties, phosphates, structure

## 1 Introduction

Fluoride–phosphate glass is widely used as an optical material owing to its unique optical properties, such as high optical transmittance in the ultraviolet (UV) to infrared (IR) range, low refractive index dispersion, and positive anomalous partial dispersion, which are not obtained with oxide glasses [1]–[4]. Although fluoride is not a typical glass-forming system, the addition of a small amount of phosphate dramatically improves its glass-forming ability and thermal and chemical stabilities while maintaining the unique optical properties resulting from the highly ionic cation–fluorine bonds. Owing to its excellent optical properties, the fluoride–phosphate system was commercially melted as optical glass at Schott in the 1960s [5], and many studies have since been conducted on the structure and physical properties of fluoride–phosphate glasses [1]–[4], [6]–[13]. Phosphorus oxide, which is a glass-forming oxide, plays an important role in constructing the glass network in fluoride–phosphate glass. It has been established that the phosphate units in phosphate glass exhibit various structures depending on the O/P ratio, such as networking ultraphosphate, $Q^3$ (O/P =

† This paper is reprinted with permission from John Wiley and Sons of reference [34]. We acknowledge John Wiley and Sons for the permission.

2.5), chain-like metaphosphate, $Q^2$ (O/P = 3.0), dimer-like pyrophosphate, $Q^1$ (O/P = 3.5), and isolated orthophosphate, $Q^0$ (O/P = 4.0) [14], where $Q^n$ denotes tetrahedral $PO_4$ unit with $n$ bridging oxygens. To the best of our knowledge, however, most studies on fluoride–phosphate glasses have focused on the metaphosphate (O/P = 3.0) composition, whereas very few studies have focused on the effects of the O/P ratio. In this study, we investigate the influence of the O/P ratio on the optical properties of fluoride–phosphate glasses and discuss the results based on the structural analysis of the glass.

## 2 Experimental Procedures

Fluoride–phosphate glasses were synthesized using an ordinal melt-quenching technique. The raw materials of $Ca(PO_3)_2$ (Rasa Industries, Ltd., Tokyo, Japan), $AlF_3$ (Morita Chemical Industries Co., Ltd., Osaka, Japan), $CaF_2$ (Hakushin Chemical Laboratory Co., Ltd., Tokyo, Japan), $BaF_2$ (Hakushin Chemical Laboratory Co., Ltd., Tokyo, Japan), and $BaCO_3$ (Nippon Chemical Industrial Co., Ltd., Tokyo, Japan) were weighed and mixed to obtain a glass weight of 100 g and then melted under the ambient atmosphere at 1223 K for 1 h in a platinum crucible. The glass compositions synthesized in this study are listed in Table 1. Hereinafter, the sample names of the $Ca(PO_3)_2$–$AlF_3$–$CaF_2$–$BaF_2$–BaO glasses are abbreviated as OP*X*, where *X* denotes the O/P ratio. A platinum lid was used during melting to prevent volatilization from the molten glass. After stirring and homogenization with a platinum propeller, the mixtures were poured into a steel mold, rapidly cooled, and immediately transferred to an annealing furnace maintained near the glass transition temperature, $T_g$. After holding at approximately $T_g$ for 3 h, the glass was slowly cooled to room temperature at a rate of 16 K/h. The compositions of the glass samples were quantitatively analyzed by X-ray fluorescence (XRF) analysis, ZSX Primus II (Rigaku Corp., Tokyo, Japan). The impurities of the glass samples were quantitatively analyzed by inductively coupled plasma–mass spectrometry (ICP–MS), Agilent 7700 × (Agilent Technologies Inc., California, United States of America). For the ICP–MS analysis, the glass samples were dissolved by acid decomposition method. The crushed glass was placed in a platinum cell, and thermogravimetry-differential thermal analysis measurements, Thermo plus EVO2 TG8121 (Rigaku Corp., Tokyo, Japan), were performed at a heating rate of 10 K/min in the ambient atmosphere. The glass density was determined using the Archimedes method with deionized water as the immersion medium. For optical measurements, the glass was optically polished, and transmittance spectra were obtained in the range of 200–700 nm using a UV–Vis–NIR spectrophotometer, UH4150 (Hitachi High-Tech Science Corp., Tokyo, Japan), and in the range of 120–300 nm using a vacuum UV (VUV) spectrophotometer, KV-2004J (Bunkoukeiki Co., Ltd., Tokyo, Japan). The refractive index dispersion of the glass was measured using a Kalnew precision refractometer, KPR-3000 (Shimadzu Corp., Kyoto, Japan), at 11 wavelengths (i, h, g, F, e, d, C, r, and t lines and 1310 and 1550 nm). IR reflection spectra were measured using microscopic Fourier transform IR spectroscopy, Nicolet iN10 (Thermo Fisher Scientific Inc., Massachusetts, United states of America), in the range of 400–4000 $cm^{-1}$ with reference to a gold mirror. The absorption spectra were obtained through the Kramers–Kronig transformation of the reflection spectra. Unpolarized Raman scattering spectra were measured at an excitation wavelength of 532.11 nm using a micro Raman spectrometer, NRS-5000 (JASCO Corp., Tokyo, Japan).

Table 1 Composition of OP*X* glasses

| | $Ca(PO_3)_2$ (mol%) | $CaF_2$ (mol%) | $BaF_2$ (mol%) | BaO (mol%) | $AlF_3$ (mol%) | O/P |
|---|---|---|---|---|---|---|
| OP3.0 | 10 | 30 | 20 | 0 | 40 | 3.0 |
| OP3.2 | 10 | 30 | 16 | 4 | 40 | 3.2 |
| OP3.4 | 10 | 30 | 12 | 8 | 40 | 3.4 |
| OP3.6 | 10 | 30 | 8 | 12 | 40 | 3.6 |
| OP3.8 | 10 | 30 | 4 | 16 | 40 | 3.8 |
| OP4.0 | 10 | 30 | 0 | 20 | 40 | 4.0 |

## 3 Results

Table 2 shows the results of an XRF analysis of OP*X* glass. The analyzed composition shows that almost linear correlation with the nominal composition, and no significant decrease in F occurred. The analyzed composition tends to be about 1 at% lower in cations and about 5 at% higher in oxygen than the nominal composition. However, similar trends were observed for $Al_2O_3$ (Nippon Light Metal Co., Ltd., Tokyo, Japan) and $AlF_3$ (Morita Chemical Industries Co., Ltd., Osaka, Japan) powders measured as standard samples, so these discrepancies between nominal and analyzed values are due to some systematic error in the measurements not due to the sample. Therefore, the results of XRF show that there were no serious compositional changes by the evaporation of fluorine.

Table 3 lists the thermal properties, densities, and optical properties of the OP*X* glasses. The increase in $T_g$ with

Table 2 Results of the quantitative analysis of glass composition by X-ray fluorescence (XRF)

| | Nominal composition | | | | | | Analyzed composition | | | | | |
|---|---|---|---|---|---|---|---|---|---|---|---|---|
| | P (at%) | Al (at%) | Ca (at%) | Ba (at%) | O (at%) | F (at%) | P (at%) | Al (at%) | Ca (at%) | Ba (at%) | O (at%) | F (at%) |
| OP3.0 | 5.0 | 10.0 | 10.0 | 5.0 | 15.0 | 55.0 | 3.5 | 8.6 | 8.8 | 4.1 | 19.4 | 55.6 |
| OP3.2 | 5.1 | 10.1 | 10.1 | 5.1 | 16.2 | 53.5 | 3.7 | 8.6 | 8.8 | 3.9 | 20.4 | 54.6 |
| OP3.4 | 5.1 | 10.2 | 10.2 | 5.1 | 17.4 | 52.0 | 3.9 | 8.4 | 8.6 | 4.0 | 22.3 | 52.9 |
| OP3.6 | 5.2 | 10.3 | 10.3 | 5.2 | 18.6 | 50.5 | 4.0 | 8.5 | 8.7 | 4.0 | 23.3 | 51.4 |
| OP3.8 | 5.2 | 10.4 | 10.4 | 5.2 | 19.8 | 49.0 | 4.0 | 8.4 | 8.6 | 4.0 | 24.8 | 50.1 |
| OP4.0 | 5.3 | 10.5 | 10.5 | 5.3 | 21.1 | 47.4 | 4.0 | 8.5 | 8.6 | 4.0 | 26.0 | 48.8 |
| $Al_2O_3$ | | 40.0 | | | 60.0 | | | 33.4 | | | 66.5 | 0.1 |
| $AlF_3$ | | 25.0 | | | | 75.0 | | 21.8 | | | 3.8 | 74.4 |

Table 3 Thermal and optical properties of OP*X* glasses

| | $T_g$ (K) | $T_x$ (K) | $\Delta T$ (K) | $\rho$ (g/cm$^3$) | $E_g$ (eV) | $n_d$ | $\nu_d$ |
|---|---|---|---|---|---|---|---|
| OP3.0 | 712 | 844 | 132 | 3.59 | 7.03 | 1.46381 | 89.2 |
| OP3.2 | 716 | 834 | 118 | 3.57 | 7.06 | 1.46638 | 88.6 |
| OP3.4 | 719 | 846 | 127 | 3.58 | 7.04 | 1.47072 | 87.5 |
| OP3.6 | 733 | 863 | 130 | 3.60 | 6.96 | 1.47711 | 86.9 |
| OP3.8 | 744 | 870 | 126 | 3.62 | 6.92 | 1.48436 | 85.7 |
| OP4.0 | 746 | 871 | 125 | 3.64 | 6.77 | 1.48946 | 85.0 |

increasing O/P ratio is due to the decrease in fluorine content in the glass. In the case of fluoride ions of fluorophosphate glasses, only one cation is enough for charge compensation of terminal F, such as P–F bonds. In the case of oxide ions, however, at least two cations are required to compensate the negative charge of an oxide ion, except for P = O double bonds. Thus, electrostatic interactions among structural units, such as $P(O, F)_4$, $Al(O, F)_n$, and cations of Ca and Ba, are supposed to be stronger in oxygen-rich OP*X* glasses, resulting in higher viscosity and $T_g$. Similar to $T_g$, the crystallization onset temperature, $T_x$, also increases with an increase in the O/P ratio. $\Delta T$ (= $T_x - T_g$) is often considered a measure of the thermal stability of glass against crystallization [15], [16], but no significant dependence on the O/P ratio is observed. The glass density increases slightly with increasing O/P ratio.

Figure 1 shows the 10-mm-thick internal optical transmittance spectra of OP3.0 and OP4.0. There is no significant difference in the position of the absorption edge between OP3.0 and OP4.0; however, OP4.0 shows a lower transmittance at 300–400 nm than OP3.0. As can be seen in the inset of Fig. 1, the 80% transmission wavelength, $\lambda_{80}$, does not change significantly with the O/P ratio at O/P = 3.0–3.4, but it exhibits drastic redshifts with the O/P ratio at O/P = 3.6–4.0.

Figure 2 shows the optical absorption spectra of OP3.0 and OP4.0 in the VUV region. The large absorption below 170 nm is the intrinsic interband absorption of the glass, and the absorption edge of OP4.0 is located in a longer wavelength region than that of OP3.0. The bandgap energy, $E_g$, is estimated from the Tauc plot according to the following equation, and the results are listed in Table 3:

$$\alpha h\nu = A(h\nu - E_g)^2 \quad (1)$$

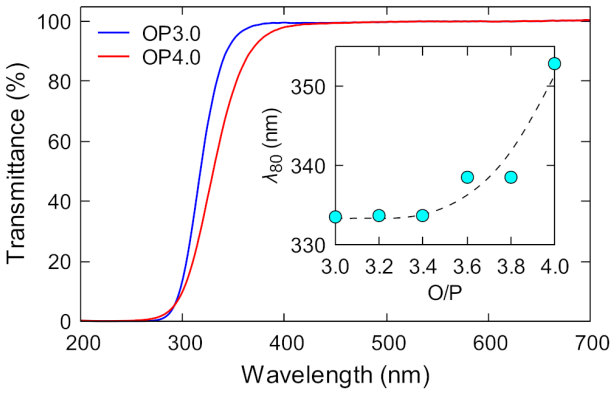


Fig. 1 Internal optical transmittance spectra (10 mm thick) of OP3.0 and OP4.0 glasses. The inset shows the O/P dependence of $\lambda_{80}$. The dashed line is shown to guide the eye.

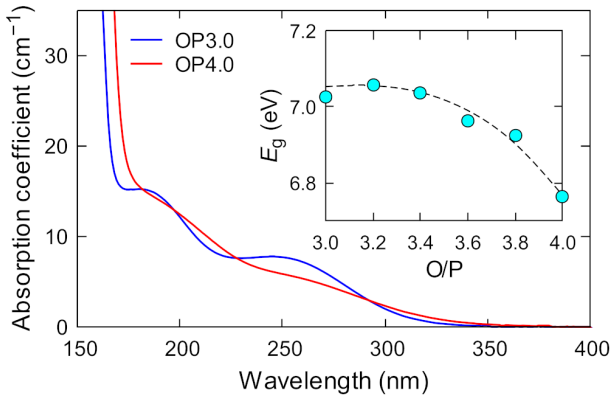


Fig. 2 Optical absorption spectra of OP3.0 and OP4.0 glasses in the vacuum ultraviolet (VUV) region. The inset shows the O/P dependence of $E_g$. The dashed line is shown to guide the eye.

where $\alpha$, $h$, $\nu$, and $A$ are the absorption coefficient, Planck's constant, light frequency, and an energy-independent constant, respectively. The values of $E_g$ for OP*X* glasses are close to those of other fluoride–phosphate glasses reported in the literature [4]. As shown in the inset of Fig. 2, $E_g$ is almost constant at O/P = 3.0–3.4; however, at O/P = 3.6–4.0, it decreases rapidly as the O/P ratio increases.

Figure 3(a) shows the results of the spectral deconvolution of the absorption spectra of OP3.0 and OP4.0. The absorption spectra can be successfully reproduced with three Gaussian functions. The absorption near 180 and 260 nm is due to the charge-transfer state (CTS) of O 2p → $Fe^{3+}$ 3d [2], [17], [18], where Fe ions are trace impurities present in the glass. Because the CTS is a parity-allowed transition, it has a large absorption coefficient, even at low concentrations of $Fe^{3+}$ ions. Table 4 summarizes the results of the ICP–MS analysis of the OP*X* glasses. It can be seen that Fe is present as a trace impurity in the glass at a concentration of approximately 20 mg/kg in each sample, and the contents of other transition metals and Pt are significantly lower than that of Fe. Therefore, the effect of impurity elements other than Fe on the UV absorption is considered negligible.

The O/P dependence of the absorption peak positions near 180 and 260 nm is shown in Fig. 3(b). Neither peak position shows a significant change in the range of O/P = 3.0–3.4, but both peaks shift drastically toward lower wave numbers with an increase in the O/P ratio from 3.6 to 4.0. As shown in Fig. 3(a), the absorption in the region below 5 eV is dominated by the CTS of O 2p → $Fe^{3+}$ 3d and is almost unaffected by the inherent absorption. Therefore, it is considered that the decrease in transmittance at 300–400 nm shown in Fig. 1 is due to the redshift of the CTS absorption as the O/P ratio increases. Figure 4(a) shows the refractive index dispersion of OP*X* glasses. As indicated in Table 3, as the O/P ratio increases, the refractive index increases, and the Abbe number decreases. Here, the Abbe number is defined as $\nu_d = (n_d-1)/(n_F-n_C)$, where $n_d$, $n_F$, and $n_C$ are the refractive indices at d (587.56 nm), F (486.1 nm), and C

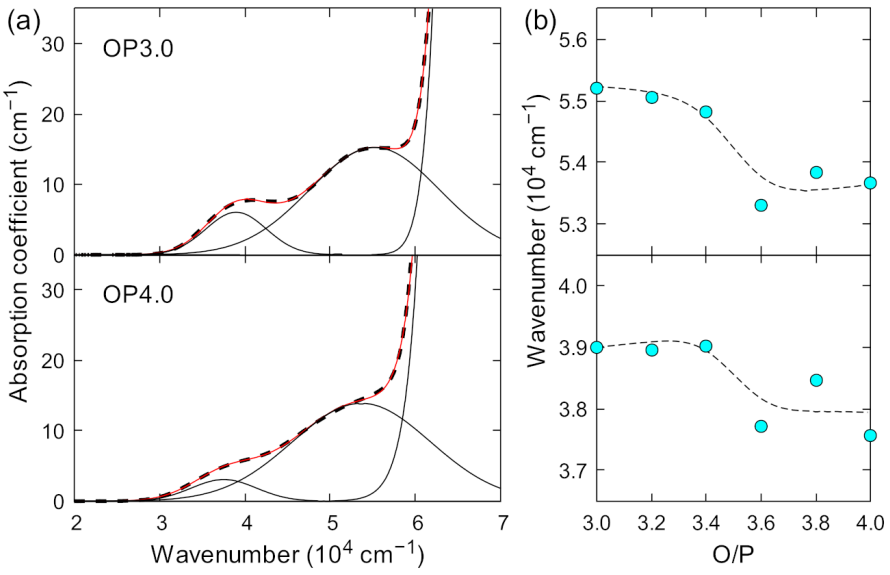


Fig. 3 (a) Spectral deconvolution of the optical absorption spectra for OP3.0 and OP4.0 glasses; (b) relationships between the peak positions and O/P ratio. The dashed and solid lines in (a) are the experimental and fitted data, respectively, and the dashed lines in (b) are guides for the eye.

Table 4 Results of the quantitative analysis of trace impurities by inductively coupled plasma–mass spectrometry (ICP–MS)

| | Cr (mg/kg) | Mn (mg/kg) | Fe (mg/kg) | Co (mg/kg) | Ni (mg/kg) | Cu (mg/kg) | Mo (mg/kg) | Pt (mg/kg) |
|---|---|---|---|---|---|---|---|---|
| OP3.0 | 1.3 | 0.2 | 21.9 | < 0.1 | 0.3 | 0.2 | < 0.1 | 0.5 |
| OP3.2 | 1.0 | 0.1 | 16.9 | < 0.1 | 0.2 | < 0.1 | < 0.1 | 0.2 |
| OP3.4 | 1.2 | 0.1 | 20.8 | < 0.1 | 0.2 | < 0.1 | < 0.1 | < 0.1 |
| OP3.6 | 1.3 | 0.2 | 21.3 | < 0.1 | 0.2 | < 0.1 | < 0.1 | < 0.1 |
| OP3.8 | 1.2 | 0.1 | 18.7 | < 0.1 | 0.1 | < 0.1 | < 0.1 | < 0.1 |
| OP4.0 | 1.1 | 0.1 | 17.5 | < 0.1 | 0.1 | < 0.1 | < 0.1 | < 0.1 |

(656.3 nm) lines, respectively. Figure 4(b) shows the correlation between $n_d$ and O/P ratio. It is noted that Fig. 4(b) shows that $n_d$ increases nonlinearly with the O/P ratio: The increase of $n_d$ with respect to the O/P ratio is greater at O/P = 3.6–4.0 than at O/P = 3.0–3.4. The refractive index dispersion is fitted using the Lorentz model, as represented by the following equation:

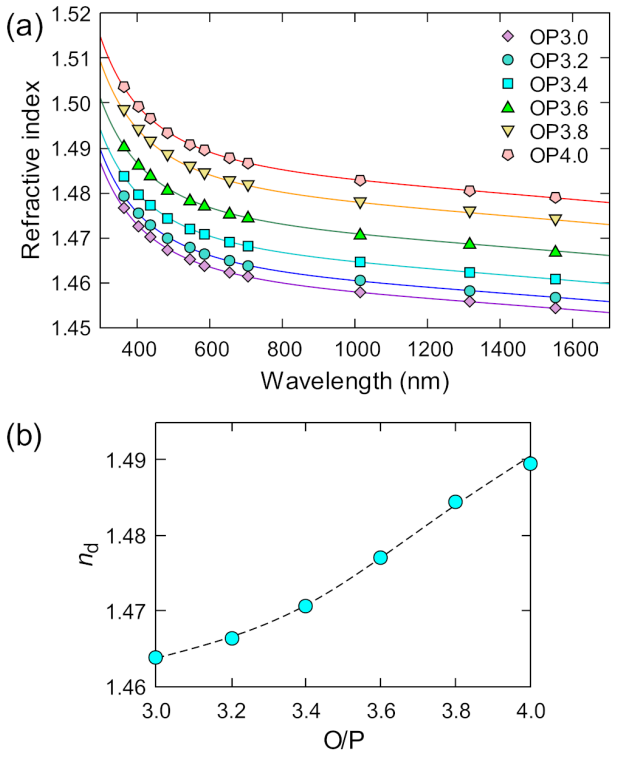


Fig. 4 (a) Refractive index dispersion of OP*X* glasses; (b) O/P dependence of $n_d$. The solid lines in (a) represent curves fitted using the Lorentz model, and the dashed line in (b) is guide for the eye.

$$(n+jk)^2 = 1+\frac{e^2}{\varepsilon_0 m}\sum_i \frac{N_i}{(\omega_i^2-\omega^2-j\omega\gamma_i)} \quad (2)$$

where $n$ is the refractive index, $j$ is the pure imaginary complex number, $k$ is the extinction coefficient, $e$ is the elementary charge, $\varepsilon_0$ is the electric permittivity of a vacuum, $m$ is the mass of the electron, $i$ is the type of oscillator, $N_i$ is the number density of the oscillator, $\omega$ is the angular frequency, $\omega_i$ is the resonance frequency, and $\gamma_i$ is the damping coefficient. Here, $k$ and $\gamma_i$ are assumed to be zero because the samples are optically transparent at the measured wavelength. Additionally, Eq. (2) can be simplified as the following equation, assuming that there are only two resonance terms in the UV and IR regions:

$$n^2 = 1+\frac{e^2}{\varepsilon_0 m}\left(\frac{N_{UV}}{\omega_{UV}^2-\omega^2}+\frac{N_{IR}}{\omega_{IR}^2-\omega^2}\right) \quad (3)$$

where $N_{UV}$ and $N_{IR}$ are the number densities of oscillators in the UV and IR regions, respectively, and $\omega_{UV}$ and $\omega_{IR}$ are the resonance frequencies in the UV and IR regions, respectively. As shown in Fig. 4(a), the refractive index dispersion of OP*X* glasses can be well represented by the two-term Lorentz model given in Eq. (3).

Figure 5 shows the O/P ratio dependence of the fitting

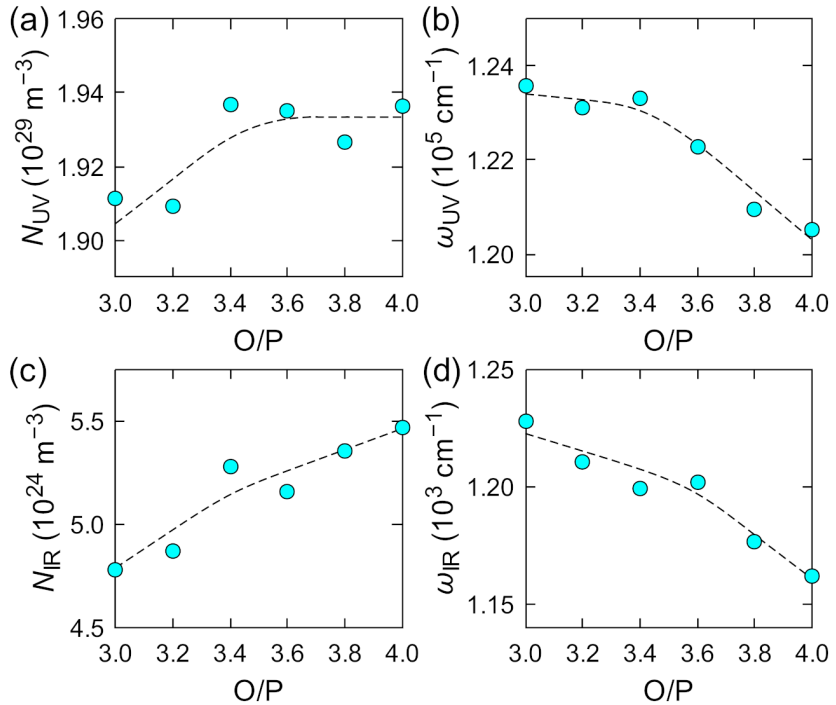


Fig. 5 Dispersion parameters of the OP*X* glasses: (a) $N_{UV}$, (b) $\omega_{UV}$, (c) $N_{IR}$, and (d) $\omega_{IR}$. The dashed lines are guides for the eye.

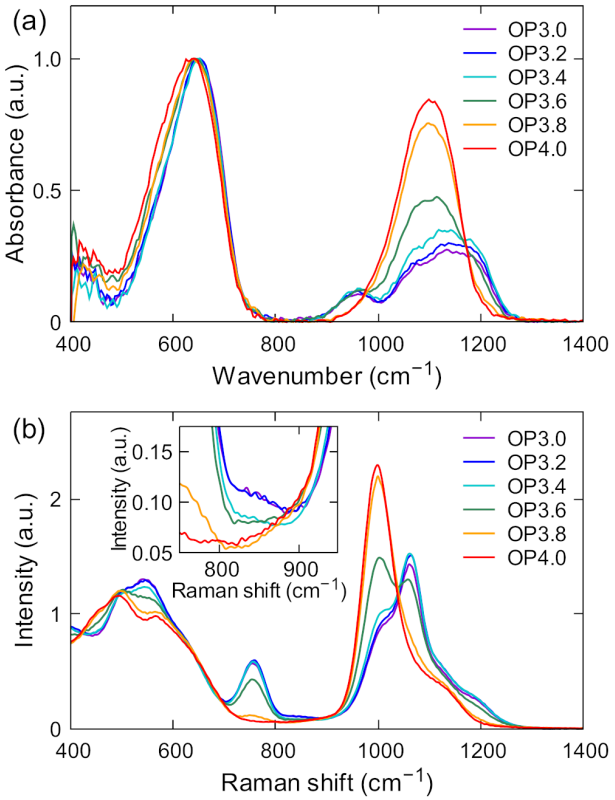


Fig. 6 (a) Infrared (IR) absorption and (b) Raman scattering spectra of the OP*X* glasses. The inset in (b) shows an enlarged view.

parameters determined using Eq. (3). As O/P increases, $N_{UV}$ seems to increase from O/P = 3.0 to 3.4 but remains almost constant at O/P = 3.6–4.0 (Fig. 5(a)). On the other hand, $\omega_{UV}$ shifts to lower wave numbers as the O/P ratio increases, and the slope becomes considerably larger at O/P = 3.6–4.0 than that at O/P = 3.0–3.4 (Fig. 5(b)). The dependence of $\omega_{UV}$ on the O/P ratio is consistent with the compositional change of $E_g$ presented in Table 3 and Fig. 2. The above results indicate that the increase in the refractive index with the increase in the O/P ratio at O/P = 3.0–3.4 and O/P = 3.6–4.0 is mainly due to the increase in $N_{UV}$ and the shift in $\omega_{UV}$, respectively. As for the oscillator parameters in IR region, with an increase in the O/P ratio, $N_{IR}$ increases almost monotonically, and $\omega_{IR}$ shifts to lower wave numbers, but the slope of $\omega_{IR}$ at O/P = 3.6–4.0 is slightly larger than that at O/P = 3.0–3.4. Therefore, the compositional dependence of the dispersion parameters in the UV and IR regions is considered to reflect changes in the electronic states and network structures of the OP*X* glasses, respectively.

Figure 6(a) shows the IR absorption spectra of the OP*X* glasses. There is no significant change in the spectrum at O/P = 3.0–3.4; however, at O/P = 3.6–4.0, the peak at 650 cm$^{-1}$ shifts to a slightly lower wave number with an increase in the O/P ratio. In addition, the intensities at 950 and 1200 cm$^{-1}$ decrease, whereas those at 1100 cm$^{-1}$ increase. Because the spectrum in the range of 800–1250 cm$^{-1}$ is attributed to the structure of the phosphate units, these changes in the spectrum at O/P = 3.6–4.0 reflect a drastic structural change in the phosphate groups that form the glass network. As shown in Fig. 7(a), the IR absorption spectrum at 800–1250 cm$^{-1}$ can be deconvoluted into four Gaussian functions. Band A (1150–1190 cm$^{-1}$) corresponds to asymmetric stretching ($\nu_{as}$) of P–O bonds in $P\text{Ø}_2\text{O}_2^-$ ($Q^2$) units [10], [13], [19], band B (1130 cm$^{-1}$) is $\nu_{as}$ of P–O bonds in $P\text{ØO}_3^{2-}$ ($Q^1$) units [10], [13], [19], [20], band C (1080 cm$^{-1}$) is the symmetric stretching ($\nu_s$) of P–O bonds in $P\text{ØO}_3^{2-}$ ($Q^1$) units and $\nu_{as}$ of P–O bonds in $PO_4^{3-}$ ($Q^0$) units [10], [13], [19] and band D (960 cm$^{-1}$) is $\nu_{as}$ of P–O–P bonds [10], [19], [20]. Here, Ø is bridging oxygen. The absence of a band at 1350 cm$^{-1}$ assigned to $\nu_s$ of P = O double bonds in $P\text{Ø}_3\text{O}$ ($Q^3$) units [14] indicates that the fraction of $Q^3$ units is very small in the OP*X* glasses. As shown in Fig. 7(a), the peak position of band A ($\nu_{as}$ P–O in $Q^2$) is located at 1189 cm$^{-1}$ in the OP3.0 glass and 1156 cm$^{-1}$ in OP4.0 glass, showing a shift to a lower wave number as the O/P ratio increases. This suggests a decrease in the length of the phosphate chains containing $Q^2$ units with increasing O/P ratio [21]. The fraction of each peak area in Fig. 7(a) is shown in part (b). The fractions of bands A ($\nu_{as}$ P–O in $Q^2$) and D ($\nu_{as}$ P–O–P) are largely constant at O/P = 3.0–3.4; however, at O/P = 3.6–4.0, they decrease monotonically as the O/P ratio increases. On the other hand, the fraction of band C ($\nu_s$ P–O in $Q^1$, $\nu_{as}$ P–O in $Q^0$) increases with the increase in the O/P ratio from 3.6 to 4.0. The fraction of band B ($\nu_{as}$ P–O in $Q^1$) does not show a clear dependence on the O/P ratio.

Figure 6(b) shows the Raman scattering spectra of the OP*X* glasses. Similar to the IR absorption spectra, no significant change is observed in the Raman spectra at O/P = 3.0–3.4; however, with an increase in the O/P ratio from 3.6 to 4.0, the intensities at 540, 750, 1060, and 1200 cm$^{-1}$ decrease, whereas those at 460 and 1000 cm$^{-1}$ increase. Figure 7(c) shows the result of spectral deconvolution of the Raman spectra at 800–1250 cm$^{-1}$ using four Gaussian functions. Band E (1160–1180 cm$^{-1}$) is $\nu_s$ of P–O bonds in $P\text{Ø}_2\text{O}_2^-$ ($Q^2$) units [6], [10], [13], [19], [22], band F (1110 cm$^{-1}$) is $\nu_{as}$ of P–O bonds in $P\text{ØO}_3^{2-}$ ($Q^1$) units [6], [10], [22], band G (1050 cm$^{-1}$) is $\nu_s$ of P–O bonds in $P\text{ØO}_3^{2-}$ ($Q^1$) units [10], [13], [19], [22] and pyrophosphate $P_2O_7^{4-}$ groups [19], and band H (1000–1020 cm$^{-1}$) is $\nu_s$ of P–O bonds in $PO_4^{3-}$ ($Q^0$) units [6], [10], [13], [19], [22]. The fraction of each peak area in Fig. 7(c) is shown in Fig. 7(d). The ratio of each peak area is almost constant at O/P = 3.0–3.4; however, at O/P = 3.6–4.0, the fractions of bands E ($\nu_s$ P–O in

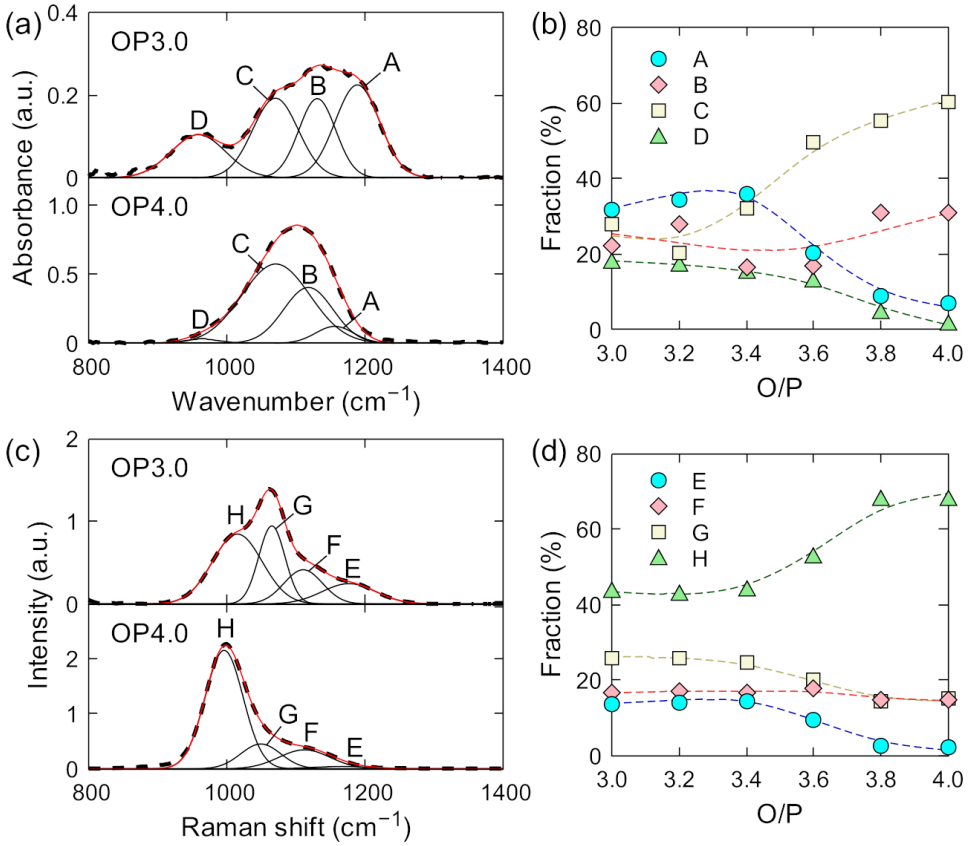


Fig. 7 Spectral deconvolution of (a) infrared (IR) absorption and (c) Raman scattering spectra for the OP3.0 and OP4.0 glasses, and the fraction of each peak area in the (b) infrared (IR) absorption and (d) Raman scattering spectra. The dashed and solid lines in (a, c) are the experimental and fitted data, respectively, and the dashed lines in (b, d) are guides for the eye.

Table 5 Assignments of infrared (IR) and Raman bands attributed to phosphate units in OP*X* glasses

| IR | | | | Raman | | | |
|---|---|---|---|---|---|---|---|
| Band | Wavenumber (cm$^{-1}$) | Assignment | Ref. | Band | Wavenumber (cm$^{-1}$) | Assignment | Ref. |
| A | 1090–1150 | $\nu_{as}$ P–O in $Q^2$ | [10], [13], [19] | E | 1160–1180 | $\nu_s$ P–O in $Q^2$ | [6], [10], [13], [19], [22] |
| B | ~1130 | $\nu_{as}$ P–O in $Q^1$ | [10], [13], [19], [20] | F | ~1100 | $\nu_{as}$ P–O in $Q^1$ | [6], [10], [22] |
| C | ~1080 | $\nu_s$ P–O in $Q^1$ | [10], [13], [19] | G | ~1050 | $\nu_s$ P–O in $Q^1$ | [10], [13], [19], [22] |
| | | $\nu_{as}$ P–O in $Q^0$ | [10], [13], [19] | | | $\nu_s$ $P_2O_7^{4-}$ | [19] |
| D | ~960 | $\nu_{as}$ P–O–P | [10], [19], [20] | H | 1000–1020 | $\nu_s$ P–O in $Q^0$ | [6], [10], [13], [19], [22] |

$Q^2$) and G ($\nu_s$ P–O in $Q^1$, $\nu_s$ $P_2O_7^{4-}$) decrease, and that of band H ($\nu_s$ P–O in $Q^0$) increase as the O/P ratio increases. On the other hand, band F shows an almost constant fraction regardless of the O/P ratio. The assignments of IR and Raman bands attributed to phosphate units in OP*X* glasses are summarized in Table 5.

The results in Fig. 7 strongly indicate a structural change of $Q^2$ units to $Q^0$ units with an increase in the O/P ratio at O/P = 3.6–4.0. The Raman spectra additionally support the breakage of the phosphate chains with increasing O/P ratio because the band at 750 cm$^{-1}$, which is assigned to the symmetric stretching mode of P–O–P bonds in the phosphate chains [6], [10], [19], [22], decreases in intensity with the O/P ratio at O/P = 3.6–4.0 (Fig. 6(b)). In addition, a slight band is confirmed at 850 cm$^{-1}$ in the Raman spectra (inset of Fig. 6(b)), and its intensity decreases as the O/P ratio increases, almost disappearing at O/P = 3.6–4.0. Because this band is attributed to the symmetric stretching of F–P–F bonds [6], [23], it indicates that P–F bonds are present at low O/P ratios. The symmetric stretching vibration of P–F bond is reported to appear around 760 cm$^{-1}$ [6], [13], [23], but it is difficult to evaluate it independently because it overlaps with the peak of the symmetric stretching vibration of P–O–P (750 cm$^{-1}$).

The evaluation of the low-frequency region (< 700 $cm^{-1}$) in the IR and Raman spectra of OP*X* glasses is more complicated. In aluminofluoride–phosphate systems, various modes due to the Al–(O, F) and P–(O, F) networks overlap in this region, and their frequencies also depend on the degree of polymerization [24]. The IR bands due to the vibrations of $AlO_6$, $AlO_4$, $AlF_6$, and $AlF_4$ appear at 535, 730, 540–570, and 620 $cm^{-1}$, respectively [25], and the asymmetric stretching modes of the Al–F–Al groups appear at 630 and 680 $cm^{-1}$ [13]. Furthermore, in the IR absorption spectra, the bending vibrations of O–P–O units and $\delta(PO_2^-)$ modes of $(PO_2^-)_n$ chains show a band at approximately 480 $cm^{-1}$, and the band at 540 $cm^{-1}$ is described as a fundamental frequency of $Q^0$ units or as harmonics of P = O bending vibrations [20]. In Raman spectroscopy, the vibrations of $AlF_6$ and $AlF_4$ units appear at 570 and 625 $cm^{-1}$, respectively [13], and the vibrations of $F_3Al–O–AlF_3$ groups appear at 530 $cm^{-1}$ [13]. In addition, the bending mode of O–P–O in $Q^0$ units, bending mode of phosphate chains, and symmetric stretching mode of P–O–P bonds in $Q^2$ units show Raman bands at approximately 440, 560, and 620 $cm^{-1}$, respectively [19]. From the above, the shift of the IR absorption peak at 650 $cm^{-1}$ with an increase in the O/P ratio (Fig. 6(a)) may reflect structural changes, such as a decrease in P–F bonds, an increase in $Q^0$ units, and a transformation from $AlF_6$ and $AlF_4$ to $Al(O, F)_6$. In addition, the decrease in intensity at 550 $cm^{-1}$ and increase at 480 $cm^{-1}$ in the Raman spectra (Fig. 6(b)) possibly reflect the structural changes of phosphate groups, such as the increase in $Q^0$ units and breakage of the phosphate chains with the increase in the O/P ratio.

## 4 Discussion

The IR and Raman spectroscopy results strongly indicate that the increase in the O/P ratio from 3.6 to 4.0 leads to the breakage of the phosphate chains, causing a decrease in $Q^2$ units and an increase in isolated $Q^0$ units. The increase in $N_{IR}$ and decrease in $\omega_{IR}$ with increasing O/P ratio (Figs. 5(c, d)) are also consistent with the spectral changes caused by the decrease in $Q^2$ units and increase in $Q^0$ units (Fig. 6(a)). This nonlinear structural change with the variation in the O/P ratio can be understood by considering the structure of phosphate glass, which is well described using the O/P ratio [14]. At O/P = 3.0–3.5, metaphosphate groups $[(PO_3)_n]$ are obtained, and the structure can be described as chains formed by $PO_4$ tetrahedra. In contrast, when the O/P ratio is between 3.5 and 4.0, isolated orthophosphate units ($PO_4^{3-}$) are generated. It should be noted that these orthophosphate units are separated from other $P(O, F)_4$ tetrahedra but are expected to be linked to Al–(O, F) polyhedra because previous structural analyses of fluoride–phosphate glass have shown that $Al(O, F)_6$ octahedra interconnect with phosphate monomers and dimers [26], [27]. In this study, however, oxygens in P–O–Al bonds are classified as non-bridging oxygens because the differences in electronegativities between Al (1.61) and O (3.44) are significantly larger than that between P (2.19) and O (3.44), resulting in more the ionicity of Al–O bonds than P–O bonds [28].

Although OP*X* glasses have a much lower oxygen content than fluorine content, structures in phosphate groups are strongly dependent on the O/P ratio, similar to phosphate glass. Therefore, it is suggested that P preferentially coordinates with oxygen, and this is also supported by the fact that the Raman intensity of F–P–F bonds is very weak compared with that of P–O-related bands (Fig. 6(b)). Such selectivity has also been reported in oxyfluoroborate glass, and its origin was discussed using the concept of electronegativity by Shinozaki et al [29]. The Pauling electronegativity values are Ba (0.89) < Ca (1.00) < Al (1.61) < P (2.19) < O (3.44) < F (3.98) [28]. Ba and Ca, which have low electronegativities, strongly attract fluorine and preferentially form ionic bonds. In contrast, P, which has a higher electronegativity than other cations, is more likely to form covalent bonds with oxygen, which has a more similar electronegativity than fluorine.

From the results of IR and Raman spectroscopy, almost no structural change was observed at O/P = 3.0–3.4, but significant structural changes were confirmed at O/P = 3.6–4.0. One possible explanation for this nonlinear trend is the effect of P–F bonds. Although the intensity of the Raman peak is small, Fig. 6(b) suggests the presence of F–P–F bonds at O/P = 3.0–3.4, and its intensity decreases with the increase of O/P ratio. Therefore, at O/P = 3.0–3.4, it is suggested that terminal fluorines in P–F bonds are replaced by oxygen as the O/P ratio increases. According to Ref. [26], fluorine preferentially replaces bridging oxygen on the phosphate tetrahedra [26]. If so, when the O/P ratio increases at O/P = 3.0–3.4, the introduced oxygen is expected to preferentially replace the fluorine in the P–F bonds to form the bridging P–O–P bonds. From Fig. 7, it can be seen that the fraction of IR band A ($\nu_{as}$ P–O in $Q^2$) and Raman band E ($\nu_s$ P–O in $Q^2$) slightly increase with O/P ratio at O/P = 3.0–3.4, supporting the formation of bridging P–O–P bonds by F → O substitution. Similarly, it is also expected that IR band D ($\nu_{as}$ P–O–P) and Raman band at 750 $cm^{-1}$ ($\nu_s$ P–O–P) increase with O/P ratio at O/P = 3.0–3.4, but the results

do not show a clear increase. This might be due to the overlap of these bands with vibrational components originating from the fluorophosphate units because it has been reported that the F–P–F and P–F bonds exhibit vibrational peaks at 980 $cm^{-1}$ in IR spectra [11], [25], and 760 $cm^{-1}$ in Raman spectra [6], [13], [23], respectively. At O/P = 3.0–3.4, the fraction and peak intensity in vibrational spectra of these fluorophosphate units should decrease with increasing O/P ratio.

According to the previous study [13], [23], the vibrational energy of non-bridging oxygen connected with P in $P(O, F)_4$ strongly depends on the number of non-bridging oxygens. This is because the bond order of terminal oxygen is averaged over the total number of non-bridging oxygens, so $PØO_2F^-$, $PO_2F_2^-$, and $PØ_2O_2^-$ ($Q^2$) units have almost the same bond order of 1.5 between P and the terminal oxygen atoms. Similarly, less polymerized $PO_3F^{2-}$ and $PØO_3^{2-}$ ($Q^1$) units would have almost the same bond order as 1.33. Therefore, even if the terminal fluorines in the P–F bonds are replaced with bridging oxygens at O/P = 3.0–3.4, it is estimated that the vibrational energy is hardly changed. At O/P=3.6–4.0, on the other hand, there should be almost no P–F bonds remaining due to the substitution to P–O–P bonds, so the oxygens introduced by increasing the O/P ratio preferentially form $P–O^-$ and P–O–Al bonds, leading the drastic structural change of phosphate units ($Q^2 \rightarrow Q^0$).

Finally, we discuss the relationship between the structural changes in the OP*X* glasses and their optical properties. Using the concept of optical basicity proposed by Duffy and Ingram, the optical basicities of the $Q^2$, $Q^1$, and $Q^0$ units are 0.50, 0.57, and 0.63, respectively [30]. This indicates that the electron-donating ability of oxygen increases as the number of non-bridging oxygen atoms in the $PO_4$ tetrahedron increases. This is because non-bridging oxygen generally has a smaller binding energy of outer electrons than bridging oxygen, resulting in a higher energy level of the O 2p orbital, which forms the upper valence states of the glass [31], [32]. In the OP*X* glasses, it is strongly expected that the energy level of the O 2p orbital shifts to a higher energy owing to the non-bridging oxygen generated with the increase in the O/P ratio at 3.6–4.0. The high-energy shift of the O 2p level reduces the transition energy to the conduction band, resulting in a decrease in the bandgap energy, as indicated in Table 3 and Fig. 2. This mechanism is also important for the refractive index dispersion because the redshift of the intrinsic resonance frequency, $\omega_{UV}$, can be explained in the same manner. As for the CTS transition band, the relationship between the electron-donating ability of ligand anions and the CTS transition energy has been discussed in other studies [18], [33]. Considering this, the nonlinear decrease in the CTS transition energy from O 2p to $Fe^{3+}$ 3d (Fig. 3) can also be explained by the drastic increase in the electron-donating ability of oxygen by the generation of non-bridging oxygen at O/P = 3.6–4.0. As for the refractive index, Fig. 4(b) clearly shows that the increase of $n_d$ with respect to the O/P ratio is greater at O/P = 3.6–4.0 than at O/P = 3.0–3.4. At O/P = 3.0–3.4, it is estimated that $n_d$ increases simply due to the increase in the number density of oxide ions with higher polarizability than fluoride ions because there is no significant change in the $Q^n$ distribution. On the other hand, at O/P = 3.6–4.0, in addition to the effect of an increase in the number density of oxide ions, the increase in optical basicity (number density of non-bridging oxygens) caused by a drastic change in the $Q^n$ distribution should contribute to increase $n_d$.

## 5 Conclusion

$Ca(PO_3)_2$–$AlF_3$–$CaF_2$–$BaF_2$–BaO glasses were prepared using the melt-quenching method, and the effects of the O/P ratio on the absorption spectrum and refractive index dispersion were evaluated. The bandgap energy determined from the intrinsic interband absorption edge was almost constant at approximately 7.0 eV at O/P = 3.0–3.4, but it rapidly decreased to 6.77 eV with the increase of O/P ratio at 3.6–4.0. Furthermore, the glass contained approximately 20 mg/kg Fe ions, and absorption peaks due to CTS from O 2p to $Fe^{3+}$ 3d were observed at approximately 180 and 260 nm; their peak positions also showed a redshift as the O/P ratio increased from 3.6 to 4.0. We also investigated the refractive index dispersion of the glass using the Lorentz model and clarified the nonlinear O/P dependence of refractive index $n_d$, the number density of oscillators, and resonance frequencies. IR and Raman spectroscopy suggested that, at O/P = 3.0–3.4, P–F bonds were substituted by bridging P–O–P bonds with an increase of O/P ratio, whereas at O/P = 3.6–4.0, the $Q^2$ units drastically decreased, and $Q^0$ units were generated as the O/P ratio increased, indicating the breakage of phosphate chains in the glass. From these results, it was concluded that the nonlinear changes in the optical properties with respect to the O/P ratio were due to an increase in non-bridging oxygen associated with the breakage of the phosphate chains: The increase in non-bridging oxygen with a high electron-donating ability enhanced the energy level of the upper valence band, resulting in a decrease in the transition energies from the O 2p level to the conduction band and

$Fe^{3+}$ 3d level.

**Acknowledgment.** The authors acknowledge M. Fujiwara (Nikon Corp.) and I. Sato (Nikon Corp.) for their help with the ICP–MS analysis and K. Kato (Nikon Corp.) for their assistance with the VUV measurements.

## References

[1] D. Ehrt and W. Seeber, "Glass for high performance optics and laser technology," *Journal of Non-Crystalline Solids,* vol. 129, no. 1–3, pp. 19–30, 1991.

[2] D. Ehrt, M. Carl, T. Kittel, M. Müller, and W. Seeber, "High-performance glass for the deep ultraviolet range," *Journal of Non-Crystalline Solids,* vol. 177, pp. 405–419, 1994.

[3] R. Lebullenger, L. A. O. Nunes, and A. C. Hernandes, "Properties of glasses from fluoride to phosphate composition," *Journal of Non-Crystalline Solids,* vol. 284, no. 1–3, pp. 55–60, 2001.

[4] D. Ehrt, "Phosphate and fluoride phosphate optical glasses—properties, structure and applications," *Physics and Chemistry of Glasses-European Journal of Glass Science and Technology Part B,* vol. 56, no. 6, pp. 217–234, 2015.

[5] W. Jahn, "Mehrstoffsysteme zum aufbau optischer gläser," *Glastechnische Berichte,* vol. 34, pp. 107–120, 1961.

[6] J. J. Videau, J. Portier, and B. Piriou, "Raman spectroscopic studies of fluorophosphate glasses," *Journal of Non-Crystalline Solids*, vol. 48, no. 2, pp. 385–392, 1982.

[7] U. Bärenwald, M. Dubiel, W. Matz, and D. Ehrt, "Structural models of the fluoroaluminate glass system $Ba(PO_3)_2$–$CaF_2$–$AlF_3$," *Journal of Non-Crystalline Solids,* vol. 130, no. 2, pp. 171–181, 1991.

[8] L. F. Santos, M. Almeida R, V. K. Tikhomirov, and A. Jha, "Raman spectra and structure of fluoroaluminophosphate glasses," *Journal of Non-Crystalline Solids*, vol. 284, no. 1–3, pp. 43–48, 2001.

[9] M. Nalin, S. J. L. Ribeiro, Y. Messaddeq, J. Schneider, and P. Donoso, "Scandium fluorophosphate glasses: a structural approach," *Comptes Rendus Chimie,* vol. 5, no. 12, pp. 915–920, 2002.

[10] D. Möncke, D. Ehrt, L. L. Velli, C. P. E. Varsamis, and E. I. Kamitsos, "Structural investigations of fluoride phosphate glasses," *Proceedings of XX International Congress on Glass,* Vols. P-10–030, pp. 1–6, 2004.

[11] H. Sun, L. Zhang, S. Xu, S. Dai, J. Zhang, L. Hu, and Z. Jiang, "Structure and thermal stability of novel fluorophosphate glasses," *Journal of Alloys and Compounds,* vol. 391, no. 1–2, pp. 151–155, 2005.

[12] D. Möncke, D. Ehrt, L. L. Velli, C. P. E. Varsamis, E. I. Kamitsos, S. Elbers, and H. Eckert, "Comparative spectroscopic investigation of different types of fluoride phosphate glasses," *Physics and Chemistry of Glasses - European Journal of Glass Science and Technology Part B*, vol. 48, no. 6, pp. 399–402, 2007.

[13] D. Möncke and H. Eckert, "Review on the structural analysis of fluoride-phosphate and fluorophosphate glasses," *Journal of Non-Crystalline Solids: X*, vol. 3, 100026, 2019.

[14] R. K. Brow, "Review: the structure of simple phosphate glasses," *Journal of Non-Crystalline Solids,* Vols. 263–264, no. 1, pp. 1–28, 2000.

[15] F. A. Santos, J. R. J. Delben, A. A. S. T. Delben, L. H. C. Andrade, and S. M. Lima, "Thermal stability and crystallization behavior of $TiO_2$ doped ZBLAN glasses," *Journal of Non-Crystalline Solids,* vol. 357, no. 15, pp. 2907–2910, 2011.

[16] M. Çelikbilek, A. E. Ersundu, and S. Aydin, "Preparation and characterization of $TeO_2$–$WO_3$–$Li_2O$ glasses," *Journal of Non-Crystalline Solids,* vol. 378, pp. 247–253, 2013.

[17] L. Liu, C. Liu, X. Wang, Z. G. Hu, R. K. Li, and C. T. Chen, "Impact of $Fe^{3+}$ on UV absorption of $K_2Al_2B_2O_7$ crystals," *Solid state sciences,* vol. 11, no. 4, pp. 841–844, 2009.

[18] D. Möncke and D. Ehrt, "Charge transfer transitions in glasses - Attempt of a systematic review," *Optical Materials: X,* vol. 12, 100092, 2021.

[19] A. Moguš-Milanković, A. Šantić, S. T. Reis, K. Furić, and D. E. Day, "Mixed ion–polaron transport in $Na_2O$–$PbO$–$Fe_2O_3$–$P_2O_5$ glasses," *Journal of Non-Crystalline Solids,* vol. 342, no. 1–3, pp. 97–109, 2004.

[20] C. Ivascu, A. T. Gabor, O. Cozar, L. Daraban, and I. Ardelean, "FT-IR, Raman and thermoluminescence investigation of $P_2O_5$–$BaO$–$Li_2O$ glass system," *Journal of Molecular Structure,* vol. 993, no. 1–3, pp. 249–253, 2011.

[21] L. Koudelka, J. Klikorka, M. Frumar, M. Pisárčik, V. Kellö, V. D. Khalilev, V. I. Vakhrameev, and G. D. Chkhenkeli, "Raman spectra and structure of fluorophosphate glasses of $(1-x)Ba(PO_3)_2$–$x$LiRAlF$_6$," *Journal of Non-Crystalline Solids,* vol. 85, no. 1–2, pp. 204–210, 1986.

[22] R. K. Brow, D. R. Tallant, S. T. Myers, and C. C. Phifer, "The short-range structure of zinc polyphosphate glass," *Journal of Non-Crystalline Solids,* vol. 191, no. 1–2, pp. 45–55, 1995.

[23] V. K. Bühler and W. Bues, "Schwingungsspektren von fluot-ophosphatschmelzen und -kristallea," *Zeitschrift für anorganische und allgemeine Chemie,* vol. 308, pp. 62–71, 1961.

[24] P. Tarte, "Infra-red spectra of inorganic aluminates and characteristic vibrational frequencies of $AlO_4$ tetrahedra and $AlO_6$ octahedra," *Spectrochimica Acta Part A: Molecular Spectroscopy,* vol. 23, no. 7, pp. 2127–2143, 1967.

[25] B. Karmakar, P. Kundu, and R. N. Dwivedi, "IR spectra and

their application for evaluating physical properties of fluorophosphate glasses," *Journal of Non-Crystalline Solids,* vol. 289, no. 1–3, pp. 155–162, 2001.

[26] R. K. Brow, Z. A. Osborne, and R. J. Kirkpatrick, "A multinuclear MAS NMR study of the short-range structure of fluorophosphate glass," *Journal of Materials Research*, vol. 7, no. 7, pp. 1892–1899, 1992.

[27] D. Ehrt, "Structure and properties of fluoride phosphate glasses," *Proceedings SPIE*, vol. 1761, pp. 213–222, 1992.

[28] L. Pauling, "The nature of the chemical bond. IV. The energy of single bonds and the relative electronegativity of atoms," *Journal of the American Chemical Society,* vol. 54, no. 9, pp. 3570–3582, 1932.

[29] K. Shinozaki, S. Sukenaga, and K. Ohara, "Photoluminescence and structural similarity of crystals with oxide–fluoride stacking structure and oxyfluoride glass," *Journal of the Ceramic Society of Japan,* vol. 128, no. 12, pp. 1030–1037, 2020.

[30] J. A. Duffy and M. D. Ingram, "An interpretation of glass chemistry in terms of the optical basicity concept," *Journal of Non-Crystalline Solids,* vol. 21, no. 3, pp. 373–410, 1976.

[31] S. K. J. Al-Ani, C. A. Hogarth, and R. A. El-Malawany, "A study of optical absorption in tellurite and tungsten-tellurite glasses," *Journal of materials science,* vol. 20, pp. 661–667, 1985.

[32] B. S. Bae and M. C. Weinberg, "Ultraviolet optical absorptions of semiconducting copper phosphate glasses," *Journal of Applied physics,* vol. 73, no. 11, pp. 7760–7766, 1993.

[33] J. A. Duffy, "Charge transfer spectra of metal ions in glass," *Physics and Chemistry of Glasses,* vol. 38, no. 6, pp. 289–292, 1997.

[34] K. Yoshimoto, M. Ueda, Y. Yamamoto, and M. Mizuguchi, "Impact of the O/P ratio on the optical properties and structures of fluoride–phosphate glass," *Journal of the American Ceramic Society*, vol. 106, no. 5, pp. 2852–2861, 2023.

吉本幸平　Kohei YOSHIMOTO
生産本部 技術統括部 光学素材部
Optical Material Department
Technology Sector
Production Technology Division

上田　基　Motoi UEDA
先進技術開発本部
Advanced Technology Research & Development Division

山本優也　Yuya YAMAMOTO
先進技術開発本部 材料・要素技術研究所
Materials & Advanced Research Laboratory
Advanced Technology Research & Development Division

水口雅史　Masafumi MIZUGUCHI
先進技術開発本部 材料・要素技術研究所
Materials & Advanced Research Laboratory
Advanced Technology Research & Development Division


吉本幸平
Kohei YOSHIMOTO


上田　基
Motoi UEDA


山本優也
Yuya YAMAMOTO


水口雅史
Masafumi MIZUGUCHI

Nikon Research Report Vol. 6
Published September 2024



NIKON CORPORATION